CASCADED MICROFIBER BIOSENSOR FOR SIMULTANEOUS DETECTION OF DENGUE AND SARS-COV-2 VIRUSES

By

NURUL NADIAH BINTI ZULKEFLEE

Thesis Submitted to the School of Graduate Studies, Universiti Putra Malaysia, in Fulfilment of the Requirements for the Degree of Master of Science

May 2024

FK 2024 7

Abstract of thesis presented to the Senate of Universiti Putra Malaysia in fulfilment of the requirement for the degree of Master of Science

CASCADED MICROFIBER BIOSENSOR FOR SIMULTANEOUS DETECTION OF DENGUE AND SARS-COV-2 VIRUSES

By

NURUL NADIAH BINTI ZULKEFLEE

May 2024

Chairman : Muhammad Hafiz bin Abu Bakar, PhD
Faculty : Engineering

The sudden emergence of dengue virus (DENV) and severe acute respiratory syndrome coronavirus 2 (SARS-CoV-2) has caused widespread disease, death, and significant societal disruption globally. They are also among the few infectious diseases that show sustained increases year by year in the last 5 years, especially in Malaysia. Accurate detection of biological markers is crucial for managing these outbreaks. Single-mode tapered fiber (SMTF) sensors offer exceptional sensitivity and versatility. This is due to the measurable wavelength shifts induced by changes in the surrounding environment through the interaction of evanescent waves. This study introduces a novel cascaded in-line configuration of two tapered fibers to detect DENV II envelope (E) and SARS-CoV-2 spike (S) proteins simultaneously. The selected taper profiles were SMTF1 (12 µm waist diameter, 5 mm taper length) and SMTF2 (10 µm waist diameter, 20 mm taper length). The performance of both SMTFs were tested using varying concentrations of sodium chloride (NaCl) to evaluate their effectiveness in detecting distinct refractive indices (RI). The analysis of the wavelength shifts in

both spectral fringes have led to the potential of simultaneous multiple analytes detection. To evaluate the dual-sensor's response to biological analytes, SMTF1 and SMTF2 were exposed to DENV II E protein and SARS-CoV-2 S protein, respectively. The immobilization of anti-DENV II E and anti-SARS-CoV-2 S1 antibodies on both SMTFs resulted in the sensitivity of 6.9 ± 0.72 nm/μM and 10 ± 0.56 nm/μM for SMTF1 and SMTF2, respectively. The corresponded dissociation constants were 1.42 $\times 10^{-10}$ M for SMTF1 and 1.15 $\times 10^{-10}$ M for SMTF2. The sensor's limit of detection (LOD) of 0.01 pM underscores its high sensitivity. Overall, the ability to detect multiple determinants using a cascaded SMTF transducer presents a promising label-free and dual-sensing biosensor for early diagnosis and effective clinical management for these two viral infections.

Keywords: Single-mode tapered fiber, dengue virus, severe acute respiratory syndrome coronavirus 2, label-free biosensor, dual-sensing

SDG: GOAL 3: Good Health and Well-Being, GOAL 9: Industry, Innovation, and Infrastructure

Abstrak tesis yang dikemukakan kepada Senat Universiti Putra Malaysia sebagai memenuhi keperluan untuk ijazah Master Sains

GENTIAN MIKRO BIOPENDERIA MELATA UNTUK PENGESANAN SERENTAK VIRUS DENGGI DAN SARS-COV-2

Oleh

NURUL NADIAH BINTI ZULKEFLEE

Mei 2024

Pengerusi : Muhammad Hafiz bin Abu Bakar, PhD
Fakulti : Kejuruteraan

Kemunculan mendadak virus denggi (DENV) dan sindrom pernafasan akut teruk koronavirus 2 (SARS-CoV-2) telah menyebabkan berleluasanya penyakit, kematian, dan gangguan yang ketara dalam kalangan masyarakat di seluruh dunia. Penyakit-penyakit tersebut juga merupakan antara beberapa penyakit berjangkit yang menunjukkan peningkatan yang berterusan dari tahun ke tahun dalam tempoh 5 tahun kebelakangan ini, terutamanya di Malaysia. Pengesanan penanda biologi yang tepat adalah penting untuk menangani wabak-wabak ini. Penderia-penderia gentian tirus mod tunggal (SMTF) menawarkan kepekaan dan kebolehan yang luar biasa. Hal ini disebabkan oleh anjakan panjang gelombang boleh diukur yang disebabkan oleh perubahan dalam persekitaran sekeliling melalui interaksi gelombang evanesen. Kajian ini memperkenalkan dua gentian tirus yang berkonfigurasi sebaris melata yang novel bagi mengesan protein DENV II sampul (E) dan SARS-CoV-2 pancang (S) secara serentak. Profil tirus yang telah dipilih adalah SMTF1 (12 μm diameter pinggang, 5 mm panjang tirus) dan SMTF2 (10 μm diameter pinggang, 20 mm panjang

tirus). Prestasi kedua-dua SMTF telah diuji menggunakan kepekatan natrium klorida (NaCl) yang berbeza untuk menilai keberkesanannya dalam mengesan indeks biasan (RI). Analisis anjakan panjang gelombang dalam kedua-dua jalur spektrum telah menunjukkan potensi kepada pengesanan pelbagai analit secara serentak. Bagi menilai tindak balas dwi-penderia terhadap analit biologi, SMTF1 dan SMTF2 masing-masing telah didedahkan kepada protein DENV II E dan protein SARS-CoV-2 S. Imobilisasi antibodi anti-DENV II E dan anti-SARS-CoV-2 S1 pada kedua-dua SMTF telah menghasilkan kepekaan masing-masing 6.9 ± 0.72 nm/μM and 10 ± 0.56 nm/μM untuk SMTF1 dan SMTF2. Pemalar penceraian yang sepadan adalah 1.42 $\times 10^{-10}$ M untuk SMTF1 dan 1.15 $\times 10^{-10}$ M untuk SMTF2. Had pengesanan penderia (LOD) sebanyak 0.01 pM menekankan kepekaannnya yang tinggi. Secara keseluruhannya, keupayaan untuk mengesan pelbagai penentu menggunakan transduser SMTF yang melata menunjukkan biopenderia tanpa penanda dan dwi-penderiaan yang menjanjikan diagnosis awal dan keberkesanan pengurusan klinikal bagi kedua-dua jangkitan virus tersebut.

Kata Kunci: Gentian tirus mod tunggal, virus denggi, sindrom pernafasan akut teruk koronavirus 2, biopenderia tanpa penanda, dwi-penderiaan

SDG: MATLAMAT 3: Kesihatan Baik dan Kesejahteraan, MATLAMAT 9: Industri, Inovasi dan Infrastruktur

ACKNOWLEDGEMENTS

Alhamdulillah, I am able to complete this thesis, all praise to the Almighty God. I am grateful to Him for granting me the physical and mental fortitude to endure all of the difficulties related to completing this research. Throughout this incredible journey, I have had the honour and pleasure to work with and meet a large number of amazing people, whom I wish to thank.

First and foremost, I would like to express my gratitude to the most important individuals in my life. To both of my dear parents, Zulkeflee Abu Kasim and Norhayati Muhamad, who have been a constant source of inspiration to me throughout my life, supporting, encouraging, and fully understanding me to finish my studies. And thank you to all of my family members for your undying love, continuous support, and faith in me. They selflessly inspired and motivated me to discover and pursue my destiny.

I would like to express my deepest appreciation to my supervisor, Associate Prof. Dr. Muhammad Hafiz Abu Bakar for giving me the opportunity to work with this research and giving me proper direction throughout the whole research process. My gratitude extends to my co-supervisor, Dr Yasmin Mustapha Kamil who was very helpful, offered invaluable assistance despite her tight schedule, and for the guidance and patience throughout the time. She has been an incredibly supportive co-supervisor, and I could not have wished for a better one. Throughout the research, I have learned a hard way to be more independent, not only to gain good research ideas but also to succeed in life. Next, I would like to thank Associate Prof. Dr. Syamsiah Mashohor, also my co-supervisor, for her support, encouragement, and guidance. Working under

their supervision was a wonderful joy and honour. I am grateful for everything they have taught me.

Aside from that, I would also like to convey my sincere thanks to everyone in the Photonic Systems Engineering Laboratory for their outstanding collaboration, motivation, and support during this research. I truly value the time we have spent working together. A moment lasts all of a second, but the memory lives on forever. I would also like to deliver special thanks to Dr. Nadiah Husseini Zainol Abidin for providing me the unwavering support and continuous encouragement throughout my years of study and through the process of researching and thesis-writing phases. Not to forget, Mr Zamili who has always been helpful whenever I need help with equipment and the fabrication of tapered fiber needed to complete this work. This Master of Science (MSc.) journey with all of you will be a lasting memory for me as I embark on a new chapter in my life. Lastly, I would like to express my appreciation to everyone who has either contributed directly or indirectly to the success of this endeavour. May God grant prosperity and honor to the aforementioned individuals throughout their lives.

This thesis was submitted to the Senate of Universiti Putra Malaysia and has been accepted as fulfilment of the requirement for the degree of Master of Science. The members of the Supervisory Committee were as follows:

Muhammad Hafiz bin Abu Bakar, PhD
Associate Professor
Faculty of Engineering
Universiti Putra Malaysia
(Chairman)

Syamsiah binti Mashohor, PhD
Associate Professor
Faculty of Engineering
Universiti Putra Malaysia
(Member)

Yasmin binti Mustapha Kamil, PhD
Senior Lecturer
Faculty of Biotechnology and Biomolecular Sciences
Universiti Putra Malaysia
(Member)

_____
ZALILAH MOHD SHARIFF. PhD
Professor and Dean
School of Graduate Studies
Universiti Putra Malaysia

Date: 10 October 2024

TABLE OF CONTENTS

LIST OF TABLES

LIST OF FIGURES

LIST OF ABBREVIATIONS

AFM	Atomic force microscopy
APTES	3-(Aminopropyl) triethoxysilane
AuNP	Gold spherical nanoparticle
AuNR	Gold nanorod
AuTNP	Gold triangular nanoprism
C=O	Carbonyl structures
C-C	Carbon-carbon bond
C-H	Methyl group
ChOx	Cholesterol oxidase
C-N	Carbon–nitrogen bond
COO^-	Carboxyl
DENV	Dengue virus
DI	Deionized water
DNA	Deoxyribonucleic acid
EDFA	Erbium-doped fiber amplifier
EDX	Energy-dispersive X-ray
EW	Evanescent wave
FESEM	Field emission scanning electron microscope
FSR	Free spectral range
GUI	Graphical user interface
IgG	Immunoglobulin G
LOD	Limit of detection
LSPR	Long surface plasmon resonance
MERS-CoV	Middle east respiratory syndrome

MZI	Mach-Zehnder interferometer
NaCl	Sodium chloride
NaOH	Sodium hydroxide
N-H	Hydrogen bond
NH_3^+	Amino
NSP	Non-structural protein
OFB	Optical fiber biosensor
OH	Hydroxyl functional group
OSA	Optical spectrum analyzer
PBS	Phosphate buffer saline
PCR	Polymerase chain reaction
PMF	Polarization-maintaining fiber
RBD	Receptor binding domain
RI	Refractive index
RMS	Root mean square
SARS-CoV-2	Severe acute respiratory syndrome coronavirus 2
SD	Standard deviation
SERS	Surface-enhanced Raman scattering
Si-NH_2	Hexamethylcyclotrisilazane
Si-O-	Silicon monoxide
SiO_4	Silicate (Orthosilicic Acid)
Si-OH	Silanol
Si-O-Si	Siloxanes
SMF	Single-mode fiber
SMS	Single mode-tapered multimode-single mode

SMTF	Single-mode tapered fiber
SPR	Surface plasmon resonance
TIR	Total internal reflection
WD	Waist diameter
WL	Waist length

CHAPTER 1

INTRODUCTION

1.1 Overview

This chapter offers a comprehensive understanding of the research's background, with the primary attention being placed on the single-mode tapered fiber (SMTF) and how it can be utilized as an optical fiber biosensor (OFB). Also included is a discussion on the connection between SMTF and how it can be used as a cascaded optical biosensor. After that, an explanation of the problem statement for this research is provided, and then the research purpose and objectives that are intended to help alleviate the situation are outlined. The scope of the research is broken down in detail, and the report's structure is outlined.

1.2 Research Background

Fiber optic technology originated for data transport and telecommunications applications. In several industries, due to the intrinsic benefits of fiber, its application in sensors has grown during the past three decades: low cost, miniaturization, lightweight, and immunity to electromagnetic interference [1]. Physical characteristics like strain, pressure, and temperature, as well as biological parameters like analyte concentration and chemical composition, can all be sensed by optical fiber sensors since they are activated by changes in light propagation caused by these stimuli. The constant demand for simple, rapid, and continuous direct monitoring techniques that use a probe or a sensing element in medical care, medicine, and commercial applications drives the development of biosensors.

The main advantages of using OFB are their excellent light delivery, increase interaction length, affordability, and capability to stimulate and detect emitted light from the desired molecules. It provides an excellent alternative to traditional techniques for label-free biomolecular measurements due to its high sensitivity, selectivity, and multi-parameter sensing. Various OFBs can be classified based on the interaction mechanisms like optical fiber grating [2], Mach-Zehnder interferometer (MZI) [3], surface plasmon resonance (SPR) [4], surface-enhanced Raman scattering (SERS) [5], tapered fiber sensing [6], and Fabry-Perot interferometer [7]. It generates signals proportional to the analyte concentration, and the received signals are analyzed using various techniques such as wavelength shifts [8], phase shift [9], intensity fluctuation [10], and frequency shift [11].

To enhance the biosensors' sensitivities, specific optical fiber structures have been developed where in this research, a method of reducing optical fiber size called tapered optical fiber was used. Tapered OFB are biofunctionalized devices based on RI detection, allowing for the specific and reproducible detection of a biological analyte [12]. Since the RI around a bare fiber biosensor cannot be tailored to a particular analyte, this type of measurement is commonly known as volume measurement. In this study, the use of SMTF as a biosensor was proposed. This allows for utilizing the propagating mode's evanescent wave (EW), enabling easier recognition of biomolecules. Tapering the fiber considerably increases the strength of the evanescent field in this research. One major benefit of these sensors is the accuracy and rapidity with which sensors can detect analytes in real-time. Because the medium's refractive index (RI) affects the modes propagating at the fiber boundary along the tapered area, it has a significant impact on SMTF's sensing capabilities [13]. Observing the

wavelength shifts in the output transmission spectrum allows for the final realization of interferometric pattern modifications and measurements.

To meet with the current diagnostic demands, there is significant room for SMTF-based sensors to improve in terms of functionality, sensitivity, selectivity, and stability. Exploring the SMTF cascaded configuration for simultaneous detection of multiple determinants is one of many solutions. Cascading tapers can improve the interaction with the sensing medium, the sensitivity, and the range of fiber-optic sensors [14]. Deoxyribonucleic acid (DNA), glucose, protein, living cells, antibiotics, and viruses are just some of the things that optical fiber biosensors have shown promise in detecting. To conduct a particular detection, bioreceptors are affixed to the surface of the sensor fiber. The basis of a label-free biosensor is labeled surface RI sensing, which involves measuring the concentration-dependent change in RI and associated wavelength shift when receptors bind to target molecules on the fiber surface. Multi-parameter sensing in biosensors, where a single optical fiber sensing device could detect multiple parameters such as viruses and diseases, has attracted significant research interest. severe acute respiratory syndrome coronavirus 2 (SARS-CoV-2), dengue virus (DENV), biotin-avidin, Middle East respiratory syndrome (MERS-CoV), and Malaria are examples of multiple disease detection having the same symptoms and characteristics. All these viruses are possible to be used in this research. Therefore, multi-parameter sensing could be realized through cascading SMTFs that are functionalized for different target analytes.

1.3 Problem Statement

Recent studies have shown the great promise of SMTF biosensors but putting them into practice in the real world has proven to be a challenging task thus far. Despite its many advantages, the detection mechanism of the SMTF sensor, which relies on spectral fringe observation, limits its multiplexing capability. The combined interferometric effect from cascading another SMTF sensor would complicate measurements of the optical response. Multiplexing capability is crucial for biosensors, particularly when diagnosing infections with similar symptoms. It provides a great option for early diagnosis of two viral diseases, DENV, and SARS-CoV-2, and can quickly identify even trace amounts of these viruses. The current method necessitates conducting separate tests for different suspected infections, significantly impacting the practicality of the sensor. This requires double the work and also affects the detection time. As both diseases show almost similar symptoms like high fever, headache, and diarrhoea, on top of cough and flu, and require different clinical management regimes, a quick detection method that can distinguish between the two viral diseases is necessary to improve the management of both. This necessitates a method to cascade multiple SMTF biosensors and allow simultaneous detection of different diseases.

1.4 Research Aim and Objectives

This research aims to investigate and develop a cascaded pair of SMTF sensors, designed to detect a distinct antigen. Due to the cascading sensor setup and the dual disease detection using dengue virus (DENV) II envelope (E) protein and SARS-CoV-2 spike (S) protein, a composite spectral profile will be created from the sensors' spectral outputs, which have different physical properties.

These objectives of the study will help achieve the aforementioned goal:

1. To fabricate and characterize an in-line cascaded fiber taper.
2. To evaluate the performance of cascaded fiber taper for simultaneous detection of two different RIs.
3. To investigate the spectral response of the fabricated fiber taper towards the presence of different biological analytes using DENV II E protein and SARS-CoV-2 S protein.

1.5 Research Scope

This thesis reports on work that was done to design and develop a cascaded tapered sensor using SMTF and study the feasibility of using a cascaded fiber taper to detect multiple RI and dual diseases at the same time. The fabrication of a sensor is the primary focus of this research, as illustrated in Figure 1.1. Because of the ease of fabrication and the increased sensitivity provided by the EW stimulated along the tapered region, SMTF was chosen as the optical transducer. Also, the reliable and power-independent sensing output is made possible by spectral-shift-based detection. The research study will primarily focus on developing a SMTF sensor that can measure RI.

This research is intended to accomplish both design and develop the necessary parameters for the diameters of the cascaded fiber and to assess the capabilities of the cascaded SMTFs sensor in detecting multiple different RI solutions at the same time. By focusing on the DENV II E and SARS-CoV-2 S proteins, the suggested sensor utilizes a virus-centric technique for detection. The selection of the E protein for Dengue was based on its presence in the virus's outer shell structure; therefore, its detection indicates the presence of the virus rather than any immunological proteins. The selection of Serotype II was based on its high prevalence in Malaysia [15]. Meanwhile, SARS-CoV-2's S protein facilitates viral entry into the host through a fusion process. Because of its correct conformation, more epitopes than other subunits or domains, and higher immunogenicity, the SARS-CoV2 S protein is the best option [16]. Because the SARS-CoV-2 S protein differs from other structural proteins in the virus, it is crucial as an antigen for the development of vaccinations and diagnostic tools. The experiment used protein concentrations in the nanoMolar (nM) range so that the results could be compared to those of other, similar studies. The selectivity of the optical sensor is influenced by the way bio-recognition molecules are attached onto the SMTF, while the sensitivity of the sensor is determined by using different concentrations of both diseases.

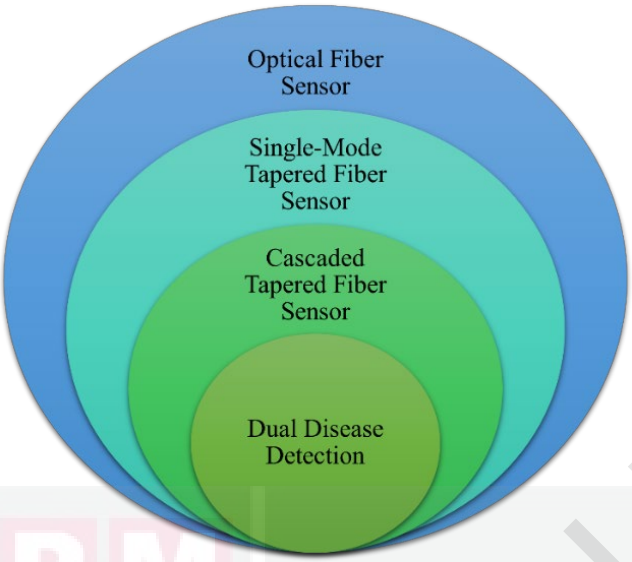

Figure 1.1: Research scope.

1.6 Thesis Organization

The following is an overview of each chapter that makes up the content of the thesis:

Chapter 1 comprises a concise introduction and outline of the research work, which also includes a summary of the study research. The issues and problem statement associated with SMTF biosensors are addressed, as well as the research's aim, objectives developed to answer those concerns, and research scope.

The review of the literature will be covered in Chapter 2. This applies to the entire issue of the usage of SMTF as a sensor. This chapter also discusses the growing technology of SMTF within optical sensors. It discusses current research on optical fiber biosensors in various detection sectors, the advantages of using it for a single disease detection, and the use of cascaded SMTFs sensors for single and dual disease detection.

Chapter 3 and Chapter 4 outline the approach used for this research. This began with the fabrication and characterization of the fiber taper until cascading the SMTF, followed by NaCl characterization, solution synthesis, and surface bio-functionalization. The antibody is then immobilized till the ultimate detection of dual illnesses. This chapter will demonstrate all the techniques, experimental setups, and parameters involved. The overall flow of the research and the steps done throughout the experiment are outlined. The results and discussion from the experiment are included also where the performance of cascaded SMTF for dual-sensing biosensor applications is addressed and studied. The findings of SMTF and cascaded SMTF characterization were recorded. The shift of wavelengths in the output spectrum caused by varying sodium chloride (NaCl) concentrations, as well as single and dual disease detection, are investigated and addressed.

Chapter 5 concludes the research work of this thesis overall, which also includes some recommendations for future work. All significant findings related to the objectives are emphasized.

CHAPTER 2

LITERATURE REVIEW

2.1 Introduction

This chapter discusses the current applications of tapered fiber sensors. The SMTF guiding principles are also reviewed in this chapter. Various research for each sensor base is elaborated along with further discussion of several studies on sensors based on the SMTF. Additionally, research on the application of optical biosensors for single and dual disease detection was discussed. Research on cascaded SMTFs was examined in the final subchapter, particularly for the detection of biomolecules utilizing the concept of evanescent wave (EW).

2.2 Optical Fiber Sensor

Over the past three decades, optical fiber sensor monitoring applications have attracted significant attention across numerous industries. This technology has an impressive performance for the next-generation intelligent sensing platform, which offers long-distance, high-precision, exceptional performance, multiparametric monitoring, and resistance to harsh environmental conditions [17]. The low transmission losses make it possible to do remote sensing with minimal signal loss. Also, it is flexible, light, small, highly sensitive, and has a compact fiber geometry. This gives it a remarkably high degree of freedom in applications with limited portability and space needs, a large bandwidth, and makes it easy to implement multiplexed or distributed sensors [18], [19].

Intrinsic sensors use the fiber itself as a transducer, whereas extrinsic sensors path and collect light from the measurement site. Optical fiber offers a practical means for implementing optical sensing [20], [21]. Typically, it works by detecting alterations in light transmission due to various external factors, such as strain, temperature, pressure, analyte concentration, or composition of chemicals [22].

Though essential for optical communication, the sensing applications of optical fiber are restricted as light does not interact with its surroundings; this is due to the cladding's near-zero propagation loss and the total internal reflection (TIR) concept [23]. Hence, the implementation of distinctive fiber-optic structures is crucial to obstruct the propagation of light, thereby enabling the light to interact with its surroundings. In the field of light alterations and sensing, various techniques have been suggested to customize light propagation and enhance its interaction with sensing materials. These methods encompass polishing, chemical etching, tapering, bending, and femtosecond grating inscription [24]. Enhanced evanescent fields can be efficiently excited in the optical fiber sensor to expose and interact light with the surrounding medium where one of the examples shown in Figure 2.1.

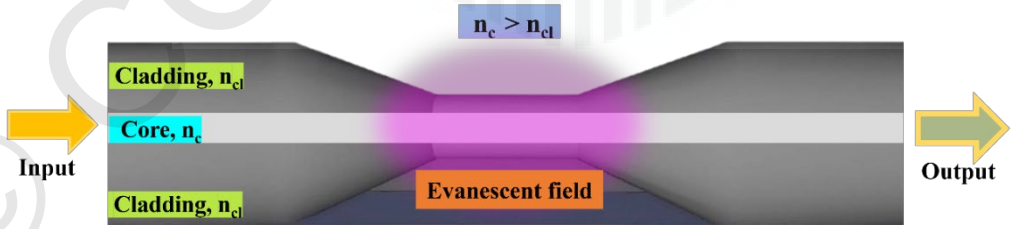

Figure 2.1: An evanescent wave-based optical fiber sensor with the cladding removed.

2.3 Overview of Tapered Fiber

Tapered fibers are currently capturing the curiosity of many interesting building blocks in a broad spectrum of photonic applications. In 2023, a journal reported on a sensitive, low-cost, quick, and straightforward tapered optical fiber system designed to detect infectious biomolecules. These are made possible by the fact that tapered fiber possesses desirable characteristics for optical guidance, such as low loss, high evanescent field strength, high optical confinement, and tunable waveguide dispersion. Tapered fibers are ideal for nonlinear optical applications due to the high field confinement they can achieve because of their high RI contrast [25].

Various techniques are employed in the fabrication of tapered fiber, as has been demonstrated. These procedures include top-down techniques such as fiber-pulling [26], bottom-up methods like vapor–liquid–solid operations [27], laser ablation [28], and electron beam lithography [29]. Flame heating is one of the most flexible ways to produce tapered fibers with high physical properties [30]. How well the tapered fiber sensor works depends on how the fiber is formed., with a lower diameter at the waist of the taper resulting in enhanced sensitivity [31].

By spectrally evaluating the medium surrounding the optical fiber, using chemically sensitive materials for attachment to other waveguides, or measuring the RI of the medium, chemical sensing is made easier with tapered fibers because access is granted to the EW of the propagating mode. Additionally, a tapered segment of the optical fiber might provide advantages for measuring physical factors like strain and temperature due to its smaller diameter. The "heat and stretch" technique used to create tapered optical fibers is shown in Figure 2.2. The polymer buffer coating, commonly

acrylate, is removed from a segment in the centre of an optical fiber with a mechanical stripper or proper solvent. The optical fiber tails on both sides of the tapering part are connected to the translation stages. The area where the buffer coating is removed is exposed to the heat source, while the fiber tails are pulled in opposite directions. The method enables the fabrication of optical fiber tapers with well-defined taper waists, regardless of the diameter [32].

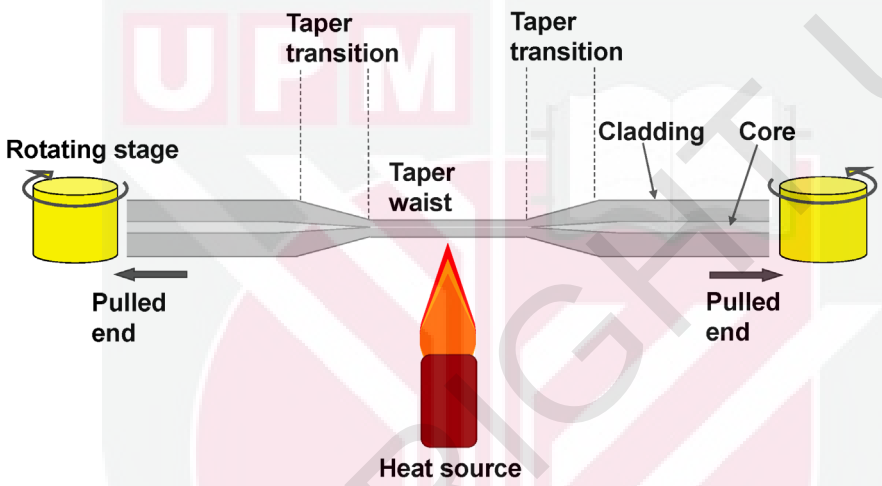

Figure 2.2: Process of fabricating tapered fiber sensors using a flame heating method [32].

2.4 Principle of Single-Mode Tapered Fiber

Recent applications of tapered single-mode fibers have gained attention due to their compact size, low cost, versatile design, and excellent sensitivity. A small diameter tapered fiber can be created by applying heat and stretching a short section of single-mode fiber (SMF) [33]. The tapered waist region emits an evanescent field, which severely confines light at the fiber surface. When light passes through a standard SMF, there is a total reflection at the point where the core and the cladding meet. This is where the evanescent field is created. However, the evanescent field cannot reach extremely far into the cladding because it is not very strong. Therefore, it is incapable

of sensing by interacting with the external materials surrounding the fiber's surface. An approach to induce the evanescent field to traverse the cladding is to apply a pulling force to the heated fiber. This may result in a certain degree of fiber diameter reduction [34].

Tapering refers to the steady lowering of an optical fiber's wall thickness into a few minor scales of diameter. Since the fibers are tapered, the light will be contained inside a smaller core radius, resulting in the evanescent field effectively propagating outside of the fiber. Consequently, the increased light is directed away from the centre [35]. The diameter of the optical fiber is reduced to a few microns in the homogenous tapered region after the tapering procedure. Tapered fiber consists of three sections: the down-taper, the uniform taper waist, and the up-taper.

When the transition areas match the adiabaticity criterion, the taper transition length exceeds the length between the fundamental and second order modes. This results in a reduced angle taper, which avoids energy coupling with higher-order modes [36]. Adiabatic tapers of this nature are distinguished by their single-mode operation and minimal losses. For non-adiabatic tapers, which fail to meet this criterion, the coupling of light to higher-order modes results in increased taper losses and the introduction of features for sensing applications into the transmission spectrum due to interference between the propagating modes.

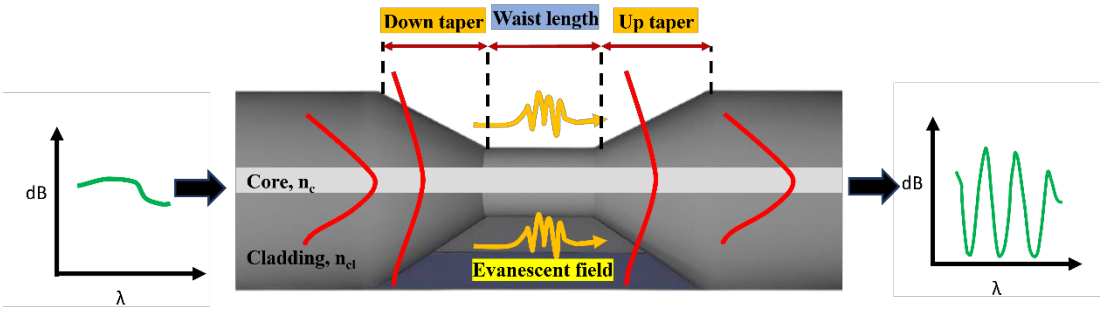

Figure 2.3: Light propagation in a non-adiabatic tapered fiber.

Significant coupling develops between the fundamental mode and the high-order cladding modes if the fiber is non-adiabatic because the taper transition zone is shorter than the coupling length. This happens as the light moves along the down-taper [37]. Afterward, the higher-order cladding modes will couple with the fundamental mode in the up-taper region, which will result in a comb spectrum being produced at the output shown in Figure 2.3. The light can pass through the cladding or air contact and travel parallel to the fiber's surface as EW. Any disruptions in the surroundings will influence the EW, and this will be reflected in the resulting spectrum as the modes are coupled together at the end of the tapered region, making this evanescent field useful for sensing [38]. The sensing qualities of the non-adiabatic tapered fiber are influenced by factors in the external environment, including the external RI and temperature [39], [40]. The total light intensity at the receptor, located at the opposite end of the untapered fiber, is defined by the following equation [39];

$$I = I_1 + I_2 + 2\sqrt{I_1 + I_2\, cos\Delta\emptyset}, \quad (2.1)$$

where I is the output intensity; $I_1 + I_2$ are the intensities of the fundamental core mode and high-order modes, respectively. $\Delta\emptyset$ is the phase shift between two modes calculated using [41];

$$\Delta\emptyset = \left[\frac{2\pi(\Delta n_{eff})L_w}{\lambda}\right], \quad (2.2)$$

where Δn_{eff} is the difference between the effective RI of the core and the effective RI of the external surrounding ($n_{eff}^{c} - n_{eff}^{ext}$) and L_w the waist length of the tapered fiber and λ is the wavelength. When the two modes combine in the up-taper area, an interference spectrum is produced with the wavelength, the effective RI difference, and the waist length of the taper all influencing the free spectral range (FSR) or fringe spacing between the interference patterns are given [41];

$$\Delta \text{ / FSR} = \left[\frac{\lambda^2}{(\Delta n_{eff})L_w}\right]. \quad (2.3)$$

As a result of the interferometric effects in the fiber taper, the result looks like the illustration in Figure 2.4. Because of the interference phenomena that happen inside a tapered fiber, the spectrum here has the appearance of a comb.

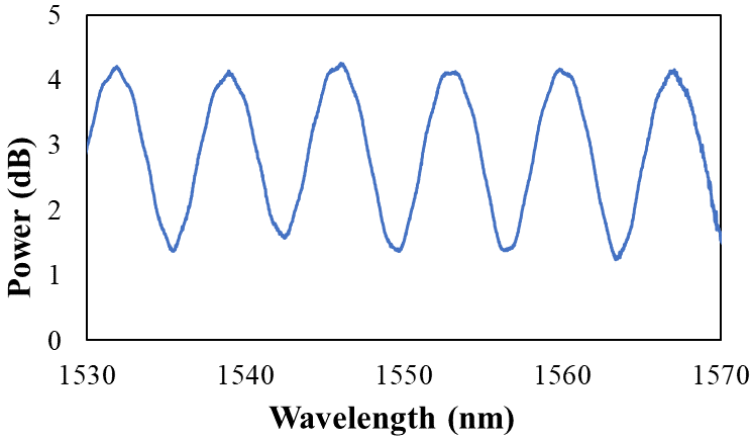

Figure 2.4. Spectral output of single-mode tapered fiber.

The evanescent field penetrates beyond the core-cladding contact by a distance denoted by d_p. Specifically, it is the mathematical distance where the evanescent field drops to 1/e of its value at the core-cladding contact [42]. This distance, denoted as the penetration depth, may be mathematically described as [41];

$$d_p = \frac{\lambda}{2\pi(n_{co}^2 sin^2\theta_{int} - n_{cl}^2)^{\frac{1}{2}}}, \quad (2.4)$$

where λ is the wavelength of the incident light, n_{co} and n_{cl} are the RI of the new core and the surrounding medium, and the incidence angle at the new core-external medium contact, measured from the normal, is denoted as θ_{int}. The up-taper region is where the fundamental and higher-order modes are recombined with the original fiber core. The RI of the solution is often less than that of the original fiber cladding. Consequently, it is anticipated that the penetration depth will decrease upon sample addition compared to the initial core/cladding fiber arrangement.

Alterations to the effective RI will influence the phase shift, which will, in turn, influence the intensity of light at a certain wavelength [43]. This will provide the impression of a movement toward the margins. Optical power variations are commonly employed to assess the reaction of an adiabatic taper to its surrounding medium. However, the non-adiabatic taper is more favorable as it aligns with the concept of interference between core and cladding modes. Because a coherent shift in the transmission spectrum will occur whenever there is a change in the medium that surrounds the sensor, which can be easily observed and quantified, the spectrum is an excellent choice for usage in a sensor.

2.5 Tapered Fiber as Biosensor

In analytical terms, a biosensor is a transducer that converts a molecular recognition of a target analyte into a quantifiable reaction [44]. Changes to the biosensors' sensing modules for detecting biomolecular, nanosized products like protein biomarkers, and viruses have allowed them to transform the conventional analytical processes into diagnostic methods, thereby making a significant impact. Because of their sensitivity to a wide range of well-known optical phenomena, optical transducers are used extensively [45]. Conventional analytical methods have many limitations, but optical biosensors, which use photodetectors to monitor changes in reflectance as a recognized signal like absorbance, fluorescence, luminescence, polarization, and RI may fill this need.

Biosensing has emerged as one of the most exciting applications for single-mode tapered fiber and has produced many works and studies on it. When the fiber taper causes some of the propagating light to be directed outside the fiber, an evanescent

field is created. The evanescent field has the potential to act as a sensor due to its ability to reach into the surrounding medium and detect variations in RI near the tapering optical fiber. Biosensors utilizing single-mode tapered fiber have garnered significant interest from researchers.

The wavelength shift-based microfiber biosensor has garnered considerable interest from experts due to its unique output and ability to operate independently of power. This transducer's interferometric spectral fringes undergo a discernible shift due to the interaction between the evanescent wave field and variations in the surrounding medium. By immobilizing a biomolecule probe, one can achieve a highly specific and accurate detection of various determinants, such as proteins [46]. Various techniques can be employed to effectively immobilize a complementary probe onto the surface of a tapered fiber biosensor. Studying bio-affinity interactions, in which the probe is attached to the fiber's surface utilizing a particular binding affinity between the probe and target molecule, is one aspect of the research [47]. This may give an immense potential for the application in disease detection, and diagnosis as well. Table 2.1 shows the recent studies and applications that can be related to the tapered fiber as a biosensor. The method, performance parameters, findings, and limitations were described.

The first study effectively created a non-adiabatic SMTF for high-sensitive RI and temperature monitoring, both theoretically and experimentally. Experiments showed that the sensor with a diameter of 8 μm could detect temperature changes down to -300 pm/C and that it could detect RI changes as small as 1800 nm/RIU. Then, a glass microtube filled with a high thermo-optical coefficient liquid was proposed as an

enhanced temperature sensor construction to take advantage of the sensor's high RI sensitivity shown in Figure 2.5 [48]. The simplified, inexpensive, and straightforward sensor construction is readily producible. It also boasts high sensitivity, robust mechanical, and excellent anti-disturbance capability.

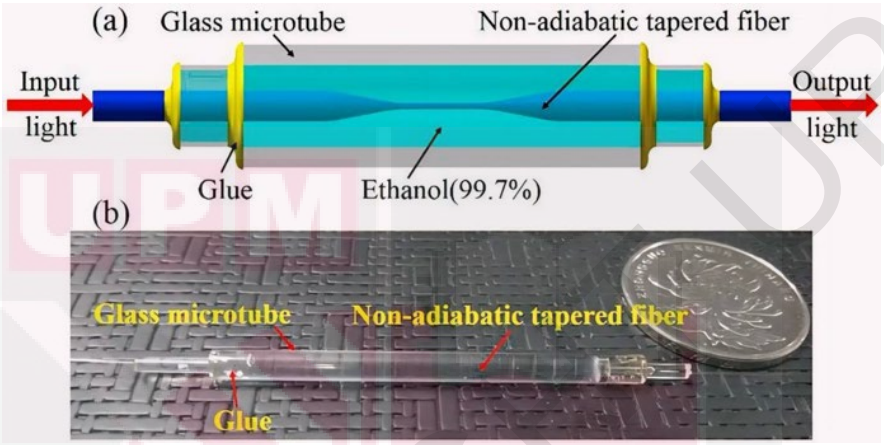

Figure 2.5: (a) Schematic representation of the enhanced sensor structure, and (b) actual image of the improved sensor structure [48].

In 2021, researchers introduced a label-free plasmonic biosensor that used laminated gold nanoparticles optical fiber technology for sensing [49]. Five microRNAs were detected with excellent selectivity using an advanced label-free ultrasensitive tapered fiber plasmonic biosensor. Three distinct metallic nanoparticles make up the biosensing platform: gold triangular nanoprisms (AuTNPs), gold nanorods (AuNRs), and gold spherical nanoparticles (AuNPs) layered tapered fiber for enhancing the evanescent mode. Since AuTNPs laminated, tapered fiber was found to have the highest RI sensitivity, it was used to evaluate the microRNA panel shown in Figure 2.6. Optimum sensitivity was obtained because hydrogen bonds were established between the target microRNAs and the single-stranded DNA probes during self-assembly [50]. Experimentally, they found that by detecting the spectrum shifts, a limit of detection (LOD) between 103 aM and 261 aM be attained for the panel of

microRNAs. In addition, the ssDNA layer adsorbed on the tapered fiber plasmonic biosensor increased the dynamic range from 1 fM to 100 nM. With a LOD between 1.097 fM – 1.2 fM, clinically relevant concentrations of the panel of microRNAs were successfully detected in human serum solution. This is the first paper to demonstrate that tapered fiber plasmonic biosensor technique can detect a panel of microRNAs. By producing a scalable sensor for the detection and quantification of large arrays of microRNAs, this simple yet incredibly sensitive technique might increase the applications of tapered optical fiber biosensors.

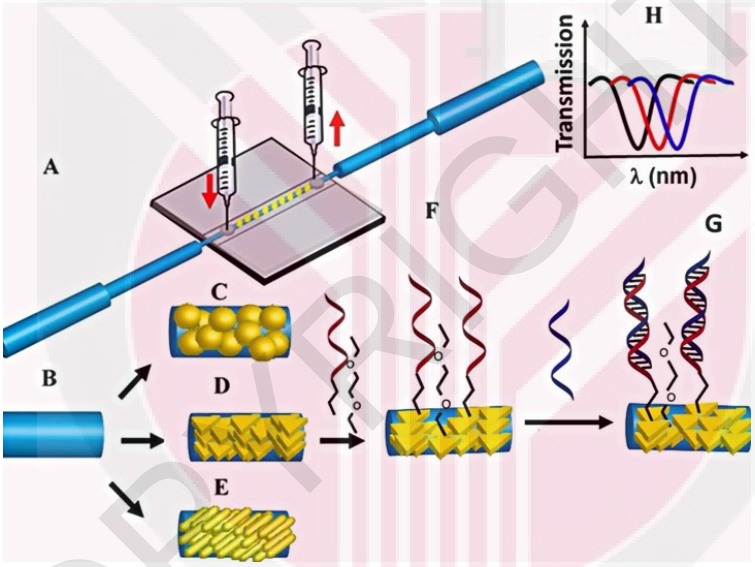

Figure 2.6: (A) Schematic of the designed TOF plasmonic biosensor, (B) functionalization of TOF with 3-aminopropyl-triethoxysilane (APTES), (C) AuNPs, (D) AuTNPs, and (E) AuNRs laminated TOF, (F) ssDNA and PEG-SH functionalized TOF, (G) hybridization with target microRNA, and (H) transmission spectrum of the functionalization [49]**.**

A tapered optical fiber-based sensor probe is created employing cholesterol oxidase (ChOx) and AuNPs to improve the sensor's sensitivity and selectivity. The results show that when cholesterol concentration rises, so does the intensity of the reflection. This is because ChOx is detected at the sensor probe. Cholesterol is oxidized into cholestenone and hydrogen peroxide in proportion to the concentration of cholesterol.

Changing the concentration of H_2O_2 causes a different reflection peak in the region around the sensor probe shown in Figure 2.7 where the immobilization occurs [51]. Biosensors with a sensitivity of 0.125 %/mM, linearity of R^2 = 0.9952, and resolution of 0.12 have been created and used to evaluate various cholesterol concentrations from 10 nM to 10 mM. The created sensor provides the 0 to 10 mM range of clinically significant cholesterol, and the LOD is discovered to be 53.1 nM [52]. The proposed sensor probe is more straightforward to manufacture and more effective than current sensors. A steadier sensor probe has been designed. Sensor probes provide excellent repeatability and reusability.

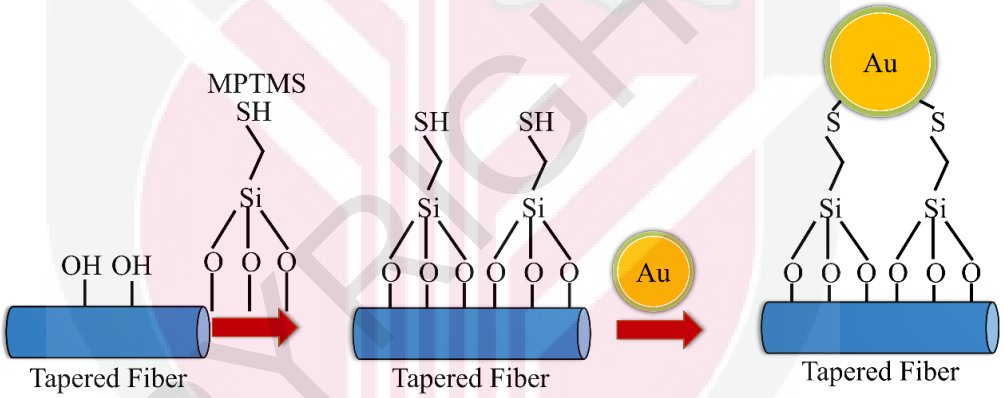

Figure 2.7: AuNPs immobilization on the sensing region of tapered fiber.

A paper was published about a label-free fiber optic biosensor for detecting bacteria based on a single mode-tapered multimode-single mode (SMS) structure shown in Figure 2.8. This study's main goal was to find out how well Salmonella Typhimurium could be found in phosphate buffer saline (PBS) and milk that had been tampered with. The multimode fiber's cladding was removed, and anti-S. Typhimurium monoclonal antibodies were subsequently added to the etched region to create the multimode interference-based SMS sensor for biosensing. The antibodies that were added to the

SMS biosensor made it possible to detect S. Typhimurium in a wide linear range (500 CFU/mL to 5000 CFU/mL) with an LOD of 247 CFU/mL. The whole analysis of per sample, including cleanup, took less than 20 minutes. A thorough theoretical study of the proposed biosensor was performed, evaluating how the beam moves and how power is dispersed. The biosensor was very selective when it came to Escherichia coli and Staphylococcus aureus. The proposed biosensing method could be used to find a wide range of pathogens with high sensitivity (275.86 nm/RIU) [53]. The SMS biosensor is better than other fiber sensor because it is easy to make and easy to use. Despite the intrigue generated by the preliminary findings of this investigation, certain factors must be considered. The fiber optic biosensor must be packaged appropriately due to its fragility. The created sensing platform, based on biorecognition components, may be utilized for multiple target analyte measurements. In particular, the created bio-interfaced sensing platform with specialized receptors is effective for in vitro pathogen detection for early infectious illness diagnosis, consumer product monitoring, and remote environmental process monitoring.

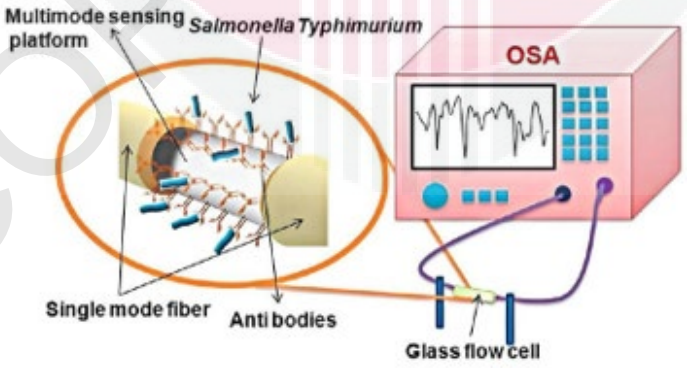

Figure 2.8: A schematic illustration of the SMS biosensor, featuring an immobilized sensing platform utilizing anti-S. Typhimurium antibodies to detect S. Typhimurium [53].

The development of the first label-free optically based sensor for DENV II E protein detection was also discussed. To do this, complementary recombinant antibodies-functionalized SMTF was required. Strong EW generated by the fiber's dimensional shift interacts with immune complexes that form on its surface when the virus is present. This interaction serves as the foundation for the sensor's core notion. The sensor configuration yielded results with a sensitivity of 5.02 nm/nM and LOD of 1 pM, respectively, and a standard deviation (SD) value of $\pm$ 0.4 shown in Figure 2.9 (a) and (b) [54]. The rapid and compact sensor is an excellent replacement for label-free, quantitative measurement of the infection. It may also help improve clinical care and understanding of the disease. In comparison with current research attempts concerning Dengue diagnosis, the sensor has proven to attain outstanding degrees of specificity and sensitivity in a rapid 15-minute detection period.

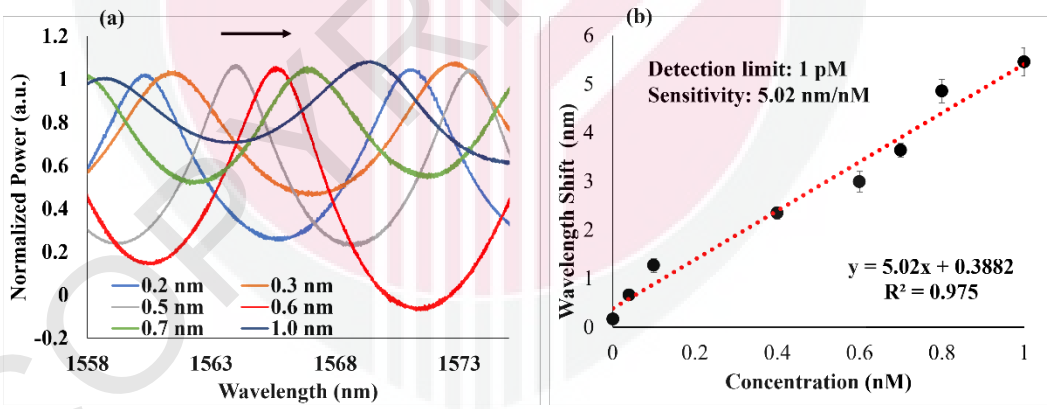

Figure 2.9: (a) Output spectra when SMTF sensor was introduced to different concentrations of DENV II E and (b) Trend line for the relationship between wavelength shift and concentration of DENV II E proteins [54].

Table 2.1: Recent studies and applications related to tapered fiber as a biosensor.

Application	Sensor Type	Sensing Method	Sensitivity	LOD	Performance	Year	Ref.
RI, Temperature	Non-adiabatic SMTF sensor	High thermo-optical coefficient	≤-300 pm/°C, RI changes ≤1800 nm/RIU	-	Simple, low-cost	2015	[55]
MicroRNA	Tapered fiber plasmonic	EW of transmission spectrum	263 nm/RIU.	1.097-1.220 fM	Simple, sensitive	2021	[49]
Disease	LSPR-based cholesterol	AuNPs with ChOx sensor probe	0.125%/mM	53.1nM	Highly reproducible	2019	[52]
	SMS Salmonella Typhimurium	Based on EW interaction	275.86 nm/RIU	247 CFU/mL	Detection time of 20 min	2018	[53]

Table 2.1: Continued

Functionalized SMTF for Dengue E protein	EW interacts with bound biomolecules	5.02 nm/nM	1 pM	Rapid detection time of 15 min	2018	[54]

2.6 Optical Biosensors for Single and Dual Disease Detection

In 2020, research on optical biosensors was done to evaluate a one-dimensional photonic crystal for the diagnosis of malaria [56]. The patient's blood is used to create the defect layer. Changes in concentration cause the index of refraction to fluctuate noticeably compared to normal blood. When the transmission peak shifts, it is an indication of trouble and can be utilized to detect malaria due to the medium's altered RI. The transmission spectra are calculated using the tried-and-true method of transfer matrices. The proposed sensor has a sensitivity of 495.73 nm/RIU, a quality factor of 2.03, a LOD of 8.07×10^{-6} RIU, and an estimated response time of 73.8 fs. This is the driving force behind the proposed biosensor device's small size, lightning-fast response time, and foolproof design.

Dual-functional plasmonic photothermal biosensors for very accurate SARS-CoV-2 were recently disclosed in research. These biosensors combine the plasmonic photothermal (PPT) effect with surface plasmon resonance (LSPR) sensing transduction to give a workable alternative to clinical COVID-19 diagnosis [57]. Nucleic acid hybridization of two-dimensional gold nanoislands (AuNIs) functionalized with complementary DNA receptors may be able to detect SARS-CoV-2 sequences. Localized PPT heat raises in situ hybridization temperature and helps distinguish comparable sequences of DNA. This dual-functional LSPR biosensor detects the targeted SARS-CoV-2 sequences at 0.22 pM and permits accurate identification of the target in a multigene mixture [58]. Figure 2.10 illustrates how the plasmonic resonances of PPT and LSPR can be excited at two different wavelengths using two different angles of incidence, hence improving sensing stability, sensitivity, and dependability. It also displays the PPT-enhanced LSPR biosensing system's

theoretical and actual configurations, as shown in Figures 2.10, respectively. After passing through the aperture-iris (I1/I2), linear polarizers (P1/P2), and birefringent crystal (BC) along the LSPR sensing route, the collimated broad-spectrum beam was reflected at the interface of AuNI-dielectric for LSPR detection. Normalized absorbances (c) and (d) of AuNI sensor chips display a narrowly tuned peak absorption at 523.4–539.7 nm (± 0.2 nm). A significant improvement in hybridization kinetics and nucleic acid detection selectivity was achieved using the in situ PPT on AuNI chips [59]. In light of the ongoing COVID-19 pandemic, the suggested dual-functional LSPR biosensor can serve as an effective and simple diagnostics platform to boost the precision of clinical testing and alleviate strain on polymers chain reaction (PCR) based methods.

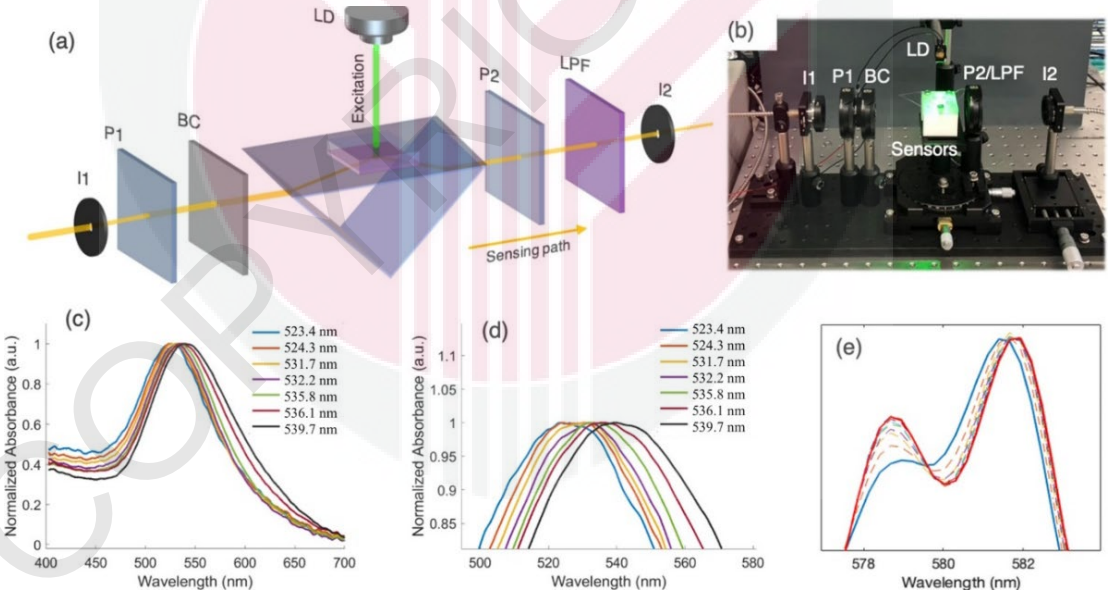

Figure 2.10: Experimental setup and system optimization [57].

2.7 Cascaded Fiber Taper

A paper published in 2022 proposes a cascaded triple waist-enlarged taper few-mode fiber (FMF) temperature sensor with a beaded structure [60]. FMF-cascaded waist-expanded taper is the sensor's main structure. The waist-enlarged taper structure diameter influences the effective RI difference and sensor sensitivity. The experiment used three waist-enlarged taper structures with diameters of 206.56 μm, 208.58 μm, and 208.58 μm, respectively. This implies that the sensor's effective RI difference is 0.00199841. As a result, the sensor's sensitivity is improved and interference from other modes is minimized. From 30 °C to 90 °C, the spectrum shows a red-shifting effect, according to the results of the experiments. A strong linear correlation exists between temperature change and wavelength shift, with a temperature sensitivity of 89.41 pm/°C [61]. This sensor's remarkable stability, high sensitivity, and simple structure make it suitable for use in chemical sensing, and biomedical temperature detection applications.

Another work proposes a RI sensor by cascading a fiber non-adiabatic SMTF and a fiber Sagnac interferometers [62]. A non-adiabatic SMTF's modal interference produces a periodic interference spectrum that varies with the external medium's RI shown in Figure 2.11 for the sensor design. Analytes in liquid form interact with the SMTF. Through modifications to the fiber Sagnac interferometer, the RI sensitivity of the SMTF was improved. Modifying the polarisation state and length of the polarization-maintaining fiber (PMF) can alter the Sagnac loop's interference spectrum. The overlaid envelope is produced by cascading two interferometers with differing FSR. This structure will alter the single interferometer's sensing capabilities [63]. The findings of the experiment indicate that the RI sensitivity of the suggested

sensor can range from 921.43 nm/RIU for a single tapered fiber to 787.24 nm/RIU for a dual tapered fiber arrangement, shown in Figure 2.11. The suggested method's low cost and ease of manufacture make it an appealing option for modifying the RI sensitivity.

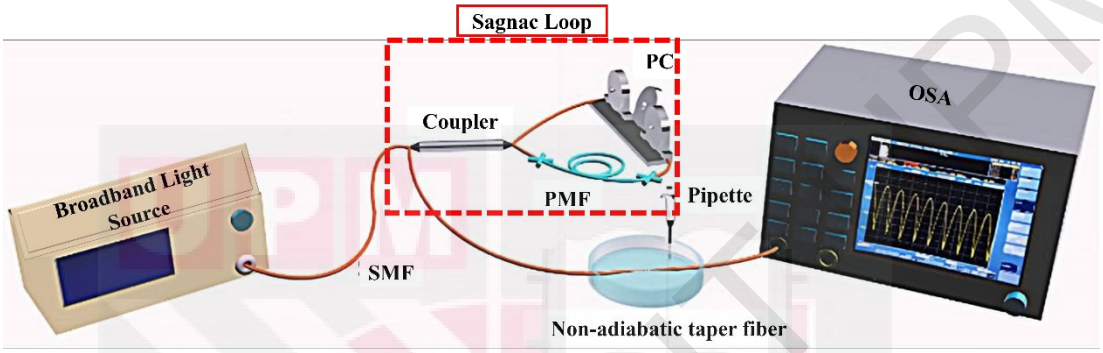

Figure 2.11: The sensor design consists of a Sagnac loop cascading together with the non-adiabatic bi-conical SMTF [62].

2.8 Critical Review on DENV II Envelope (E) and SARS-CoV-2 Spike (S) Proteins

Traditional approaches to viral detection involve qualitative assays based on PCR and enzyme-based antibodies, viral separation, and immunofluorescence utilizing microscopy. However, these methods are not appropriate for repetitive clinical testing since it requires an extended period, ranging from 2 to 14 days, lead to higher costs and insufficient to address the issue of rapid community spread [64]. Various biomarkers such as DNA, RNA, peptides, antibodies, glycoproteins, and antigens can identify viral infections. These biomarkers are categorized into two types: antigens and antibodies [44]. Recent studies have highlighted the potential of using sensors to identify dengue virus and SARS-CoV-2 [47], [54]. This fascination arises from the difficulties presented by the similar symptoms that often occur in the initial phases of

infection [65]. Although there were fluctuations in dengue cases from 2020 to 2021, there has been a notable rise in the number of COVID-19 cases in most countries in 2021, as depicted in Figure 2.12. Infections and diseases can cause a wide variety of symptoms, from no sign of sickness to death. Individuals diagnosed with COVID-19 might receive inaccurate dengue serology results because of potential cross-reactivity between both viruses and vice versa [66].

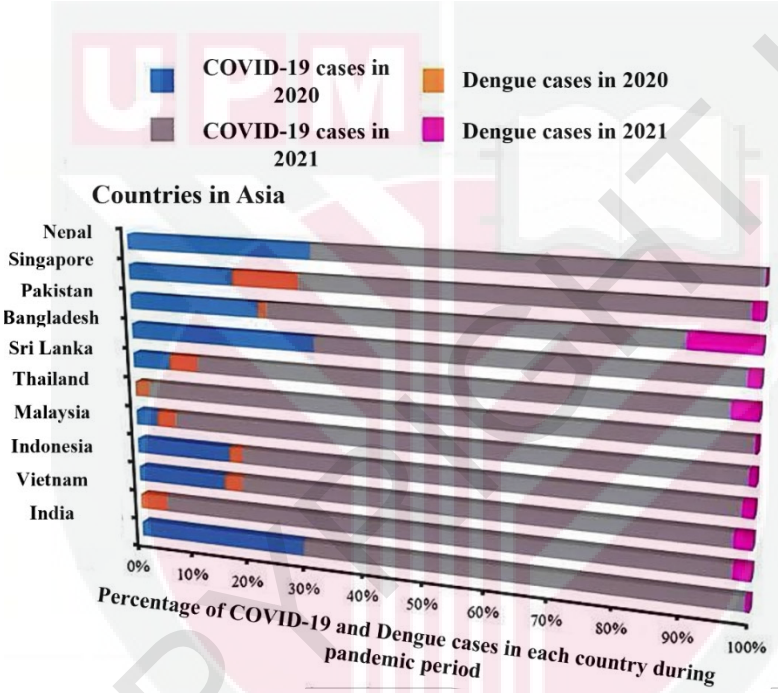

Figure 2.12: Percentage of dengue and COVID-19 incidences in various Asian countries during the pandemic period from 2020-2021 [66].

2.8.1 Dengue Virus Pathology and Virion Structure

The dengue virus is usually spread by mosquitoes in tropical and subtropical areas. Each year, between 100 and 400 million people get infected with it. As per a recent report by the World Health Organization (WHO), the rise in infected cases in 2020 has elevated DENV to a significant disease following COVID-19. As of now, there are still no specific therapeutic drugs or vaccines available for DENV infection [67]. One

explanation is the cross-reactivity between DENV and other flaviviruses because of the similar conserved structure found on the envelope (E) protein shared among the flaviviruses [15]. Four types of DENV have been confirmed by tests: DENV-1, DENV-2, DENV-3, and DENV-4. Their nucleotide sequences are very similar, with a similarity of 65%–70% [68]. The two envelope-associated proteins, M and E proteins, are present in a lipid bilayer that makes up the DENV envelope. Table 2.2 displays the three structural domains (DI, DII, and DIII) that are known to form the E protein.

Table 2.2: Three structural domains of Dengue E protein [69], [70].

Structural Domains	Function
DI	The hinge region, linked to two other functional domains, changes E protein structure due to external pH.
DII	Hydrophobic-rich peptide sequence contributes to E protein dimerization
DIII	Ig-like domain

The E protein dominates the viral surface and is the main focus of the immune response. It plays a crucial role in various biological functions such as binding to receptors, fusion, and entering host cells. The E protein, particularly its domain III (DIII), triggers host immune responses by generating protective and neutralizing antibodies, as illustrated in Figure 2.13. Hence, the dengue E protein plays a crucial role as an antigen for the development of vaccines and testing methods.

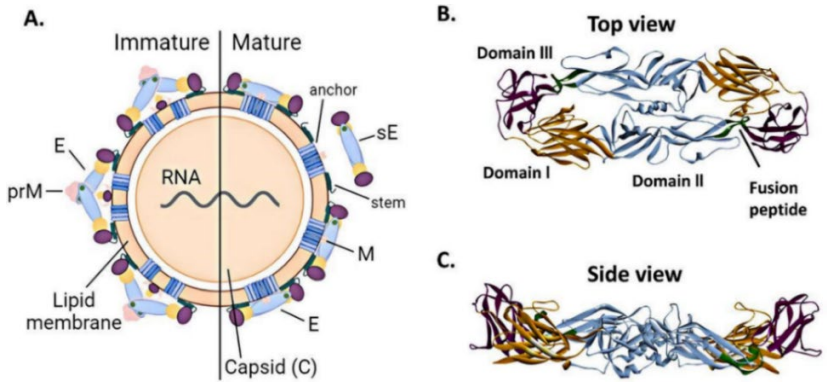

Figure 2.13: A dengue virus particle is shown graphically. Both immature and mature virions are displayed in (a). The crystal structure and domains of the dengue envelope protein's dimeric form from (b) the top and (c) side view [70].

2.8.2 Structural and Functional Properties of SARS-CoV-2

Novel coronavirus disease 2019 (COVID-19), an epidemic triggered by an entirely new coronavirus, emerged in December 2019 and has subsequently proliferated internationally, transforming into a pandemic. It was observed promptly that COVID-19 was attributed to a coronavirus subsequently identified as SARS-CoV-2. SARS-CoV-2 is an encapsulated, spherical particle measuring 65–125 nm in diameter [71]. The four structural proteins of SARS-CoV-2 are the envelope (E), spike (S), nucleocapsid (N), and membrane (M) shown in Figure 2.14. Using a fusion process, the S protein, which has been observed at the atomic level through electron microscopy, facilitates the entry of viruses into the host [16].

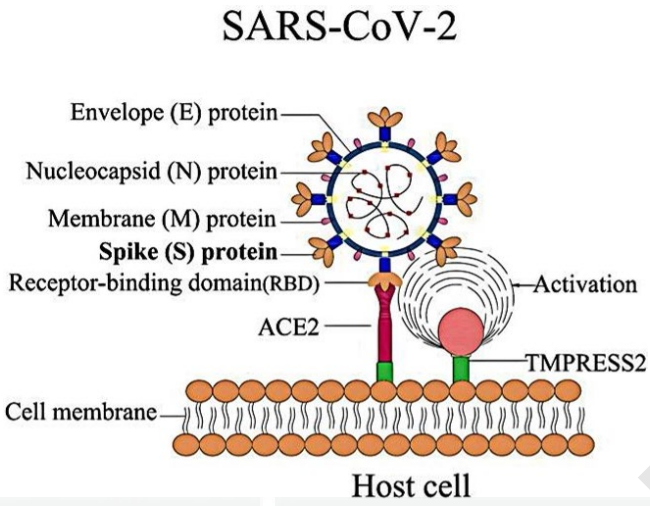

Figure 2.14: Functions and structural characteristics of the SARS-CoV2 S-protein. S-protein interaction with host cells: The ACE-2 receptor on the host cell binds to the virus via the RBD of the S-protein [71].

The outermost transmembrane protein of the virus, known as the S protein, has a molecular weight of about 150 kDa. It interacts with the lower respiratory tract cells that produce the angiotensin-converting enzyme 2 (ACE2) to form homotrimers that protrude on the viral surface and aid in the attachment of envelope viruses to host cells [72]. Understanding receptor recognition and cell membrane fusion is essential, involving two subunits, S1 and S2. The S1 subunit contains a receptor-binding domain that recognizes and binds to the host receptor angiotensin-converting enzyme 2, while the S2 subunit aids in viral cell membrane fusion by forming a six-helical bundle via the two-heptad repeat domain [73]. The S protein has distinctive characteristics that set it apart from other structural proteins in SARS-CoV-2. Choosing the SARS-CoV2 S-protein over other subunits or domains is ideal due to its proper conformation, increased number of epitopes, and higher immunogenicity [74]. Therefore, the SARS-CoV-2 S protein is essential as an antigen for the creation of vaccines and testing techniques.

2.9 Summary

The concept of SMTF sensors was broken down in detail, including its overarching theory as well as the method by which it functions. Following an explanation of the SMTF and sensor-based SMTF principle, a discussion of the advantages and disadvantages of this technology followed. Several studies that were associated with SMTF as a biosensor were highlighted here, with a particular focus on the techniques and the concrete characteristics. This study also discussed various research findings on the use of SMTF as a biosensor. In conclusion, the literature on the application of optical biosensors for single, dual disease detection and cascaded fiber taper was also presented and addressed in this chapter. These biosensors were utilized to detect single and dual diseases simultaneously. The following chapter will provide a comprehensive account of the methods that were implemented throughout the experiment.

CHAPTER 3

FABRICATION AND PERFORMANCE ANALYSIS OF A CASCADED SINGLE-MODE TAPERED FIBER TOWARD REFRACTIVE INDEX VARIATION

3.1 Introduction

The experimental processes involved in the design and development of the cascaded SMTF sensor for dual-detection towards different variations of refractive index are described in depth in this chapter. To accomplish the goals and objectives of this research, meticulous planning was implemented. The preparation, experimental setup, and observed parameters are discussed in detail in this chapter.

3.2 Research Planning

Figure 3.1 shows the research planning in a flowchart, which shows the steps and order of the research. The first step in designing and making a cascaded SMTF for a dual-sensing biosensor was to make conventional discrete SMTF with different parameters. Then, the SMTFs were tested with air to find the two best parameters needed to make a large and small FSR, which are the most suitable FSRs. Once the right parameter tapers were found, the chosen SMTFs were characterized by using NaCl solutions with different concentrations to compare them. Next, the research moved on to making cascaded SMTF and figuring out how cascaded SMTF worked with different amounts of NaCl. These few steps were the basis of the whole research to test whether the sensor could pick up two different RIs at the same time. The detailed process and outcome of the steps are explained in the following subsections.

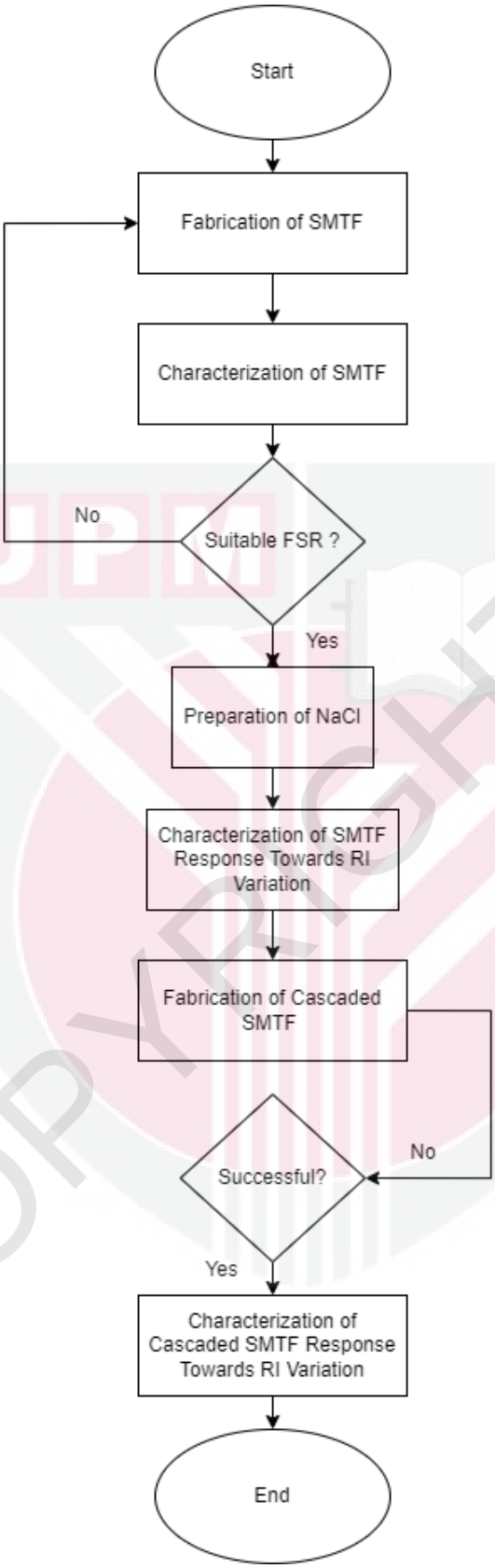

Figure 3.1: Flowchart of the experiments conducted for the performance of cascaded SMTF towards refractive index variation.

3.3 Fabrication and Characterization of SMTF

The fabrication of the sensing transducer, SMTF for this study was manufactured by GPX-3400 Optical Glass Processing Workstation where it is a multifunctional, computer-controlled device designed for glass processing. The filament is used as the source of heat in the machine. With the filament being size- and material-specific, it becomes much easier to manipulate and control the design of the glass process output. The workstation's built-in digital CCD camera and mirror tower allow for clear side end-view pictures, exact measurement, and alignment, making it ideal for dimension measuring. Figure 3.2 illustrates the structure of the SMTF, which consists of three main sections known as the down taper, the waist, and the upper. Within these regions, it is necessary to exercise appropriate control over factors such as the down taper and up taper length, waist length (WL), and waist diameter (WD). The uniformity of the created tapers was assured by setting the fiber rely on velocity and heat power during heating to 1 mm/s and 60 W, respectively.

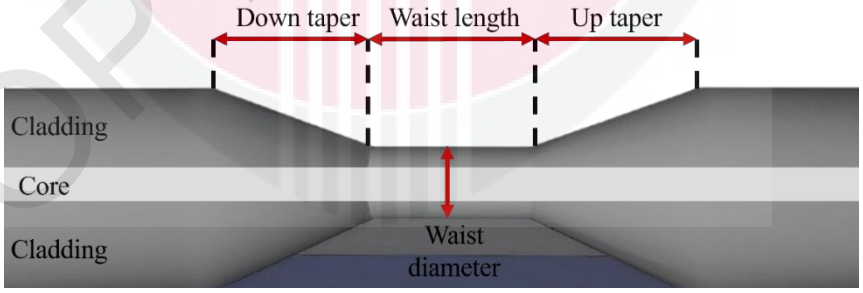

Figure 3.2: Single-mode tapered fiber schematic diagram.

This fabrication goal is to enable light to be excited and propagated near the fiber's boundary. Alcohol, wipes, fiber remover, and single-mode fiber (Corning SMF-28 Ultra 200) were used to prepare the SMTF. The first step was to use a fiber remover to remove the coating around the fiber. An alcohol-infused cloth was then used to

cleanse the fiber of residues and grime. Figure 3.3 shows all the equipment required for these steps. Finally, the fiber was inserted into the Vtyran machine, which can be seen in Figure 3.4. Here is what each part of the Vytran machine did. Starting with the fiber lifters, which held, positioned, and moved the fiber during the different processes that the Vytran machine did.

Figure 3.3: Equipment for SMTF fabrication.

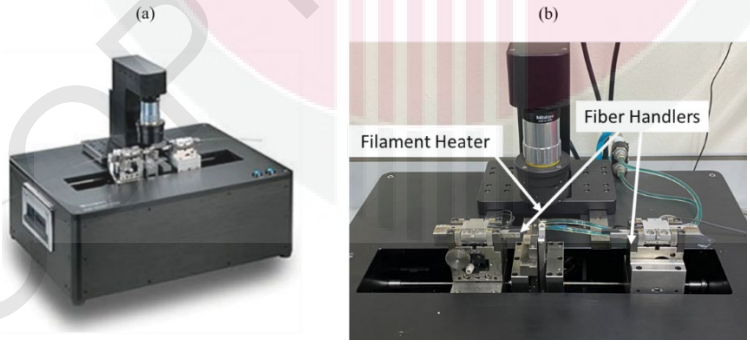

Figure 3.4: Vytran (a) overview machine and (b) each part in Vytran Machine.

The machine tapered the fiber by the values entered into the graphical user interface (GUI) regarding the WL, down taper length, and up taper length, as well as the WL and WD illustrated in Figure 3.5. Both diameter and length of fiber can be conveniently modified and regulated via the GUI of the Vytran. Following the fabrication process, a CCD imaging system was employed to validate and oversee the fiber's structure and quality. Vytran will then taper the fiber to the desired value that had been set before it begins the process. Using the CCD imaging system, it is possible to identify and monitor the present state and structure of the fiber once the fabrication process is complete shown in Figure 3.6. As the diameter of the tapered section has decreased, the SMTF has become fragile and must be handled with great care. The WL and WD were changed in this study, but the down taper length and up taper length remained the same at 5 mm. It is known that this value can result in the nonadiabaticity necessary for the interferometric effect [41].

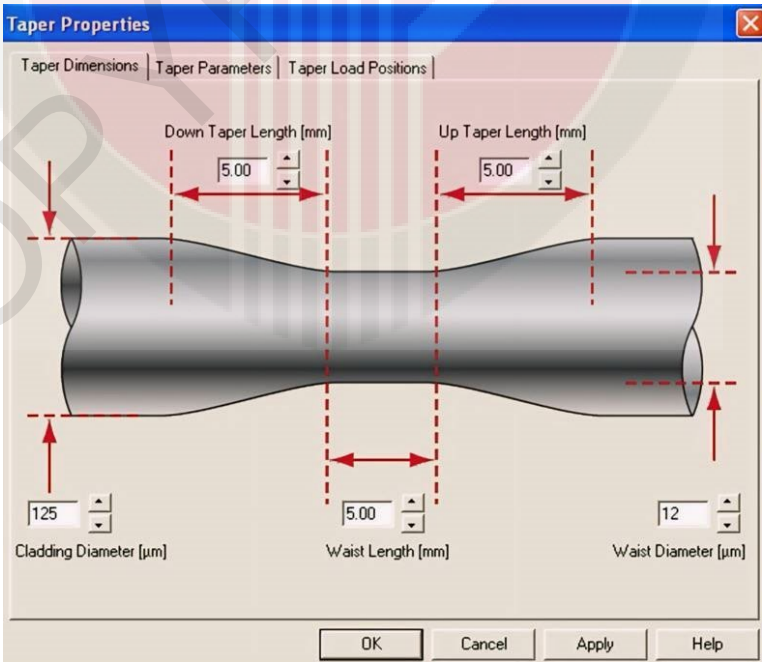

Figure 3.5: Vtyran GUI.

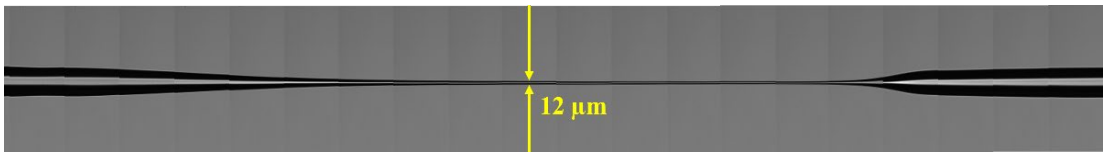

Figure 3.6: SMTF from CCD imaging system.

A reference spectrum was obtained before connecting the fiber taper by physically connecting the Optical Spectrum Analyzer (OSA, AQ6331) and C-band Erbium-doped Fiber Amplifier (EDFA-C100) light sources using two spliced single mode FC/PC pigtails. Next, the splicing point of the two pigtails was disconnected. The SMTF was then spliced with one end to the pigtail that was attached to OSA and the other end to the pigtail linked to the light source. The resulting spectral output was then compared to the reference spectrum. Each fiber taper was fabricated and characterized before proceeding to SMTF response toward RI variation characterization. Figure 3.7 shows the experimental configuration of a characterization using SMTF. Spectral measurements were performed using wavelength resolution of 0.05 nm and a wavelength ranging from 1500 nm to 1600 nm. After that, the taper parameters that satisfied the FSR requirement outlined previously were selected for the further steps.

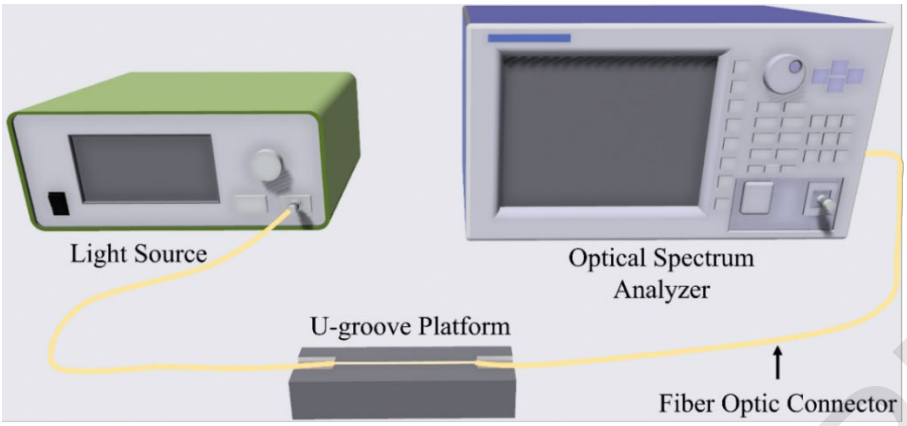

Figure 3.7: SMTF characterization setup in 3-Dimension.

The findings of the FSR characterization tests performed on nine different taper profiles using air are presented in Figure 3.8 and Table 3.1. While the values of the down taper length and up taper length were held constant at 5 mm, the values of the WL and WD were altered. To calculate an average FSR, each taper profile was characterized three times. According to the findings shown in Table 3.1, the typical FSR for each taper profile reduces either when the WL is increased or when the WD is reduced [75]. The two appropriate parameters for cascaded SMTF are those that create large fringes ideally with FSR more than 16 nm, and those that provide small fringes preferably with FSR below 5 nm. The value was chosen due to the OSA limitation of resolution to avoid overlapping fringes and ensure accurate data interpretation. Due to their distinctive average FSR (23.2330 nm vs 3.1075 nm), taper 8 (WL = 5 mm, WD = 12 µm) denoted as SMTF1 and taper 1 (WL = 20 mm, WD = 10 µm) denoted as SMTF2 were selected for further experimentation.

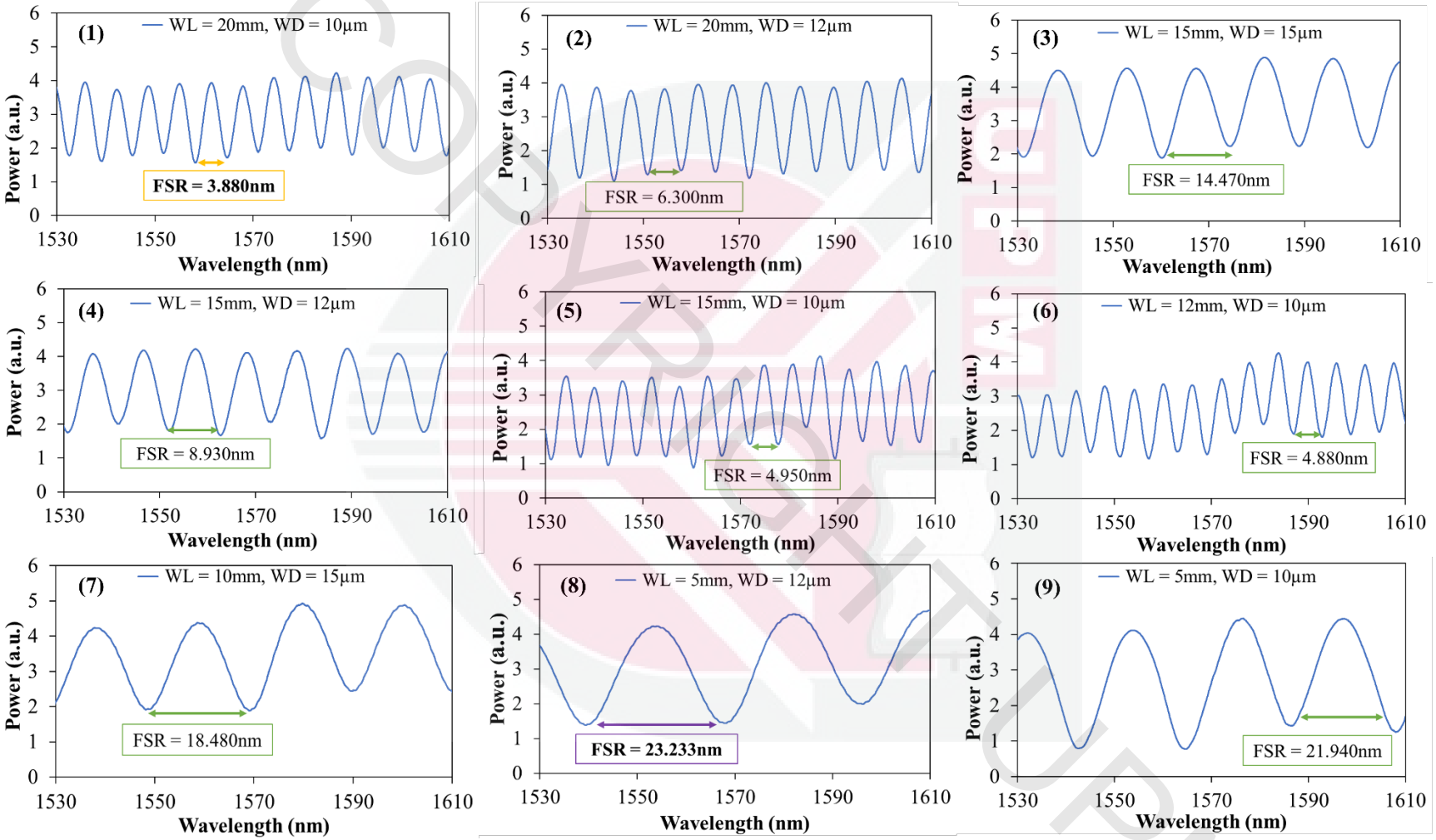

Figure 3.8: Average FSR value for nine different waist length and waist diameter.

Table 3.1: Analysing the effects of waist length and diameter on FSR performance.

No.	Taper Profile Parameter			
	Up/Down taper (mm)	Waist Length (mm)	Waist Diameter (μm)	Average FSR (nm)
1	5	20	10	3.880
2	5	20	12	6.300
3	5	15	15	14.470
4	5	15	12	8.930
5	5	15	10	4.950
6	5	12	10	4.880
7	5	10	15	18.480
8	5	5	12	23.233
9	5	5	10	21.940

Figure 3.9 depicts the output spectrum of taper profile 8 which was designated as SMTF1 with large fringes and taper profile 1 with small fringes as SMTF2 which was observed using OSA. For tapered fiber sensor, the greater the degree of bending and refraction of light, the greater its sensitivity.

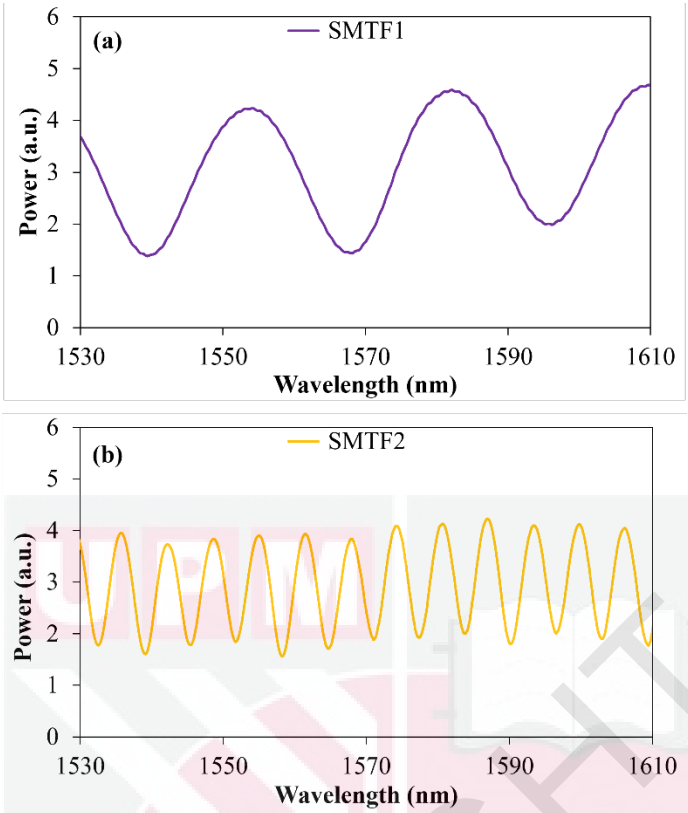

Figure 3.9: Output spectra taken from taper profiles of pre-cascaded SMTF (a) taper 8 and (b) taper 1.

3.4 Characterization of SMTF Response Towards Refractive Index Variation

Figure 3.10 depicts the methodology of NaCl solution, whereby different mass NaCl were diluted into a beaker containing 20 mL deionized water detailed in Table 3.2. For RI characterization, newly fabricated SMTFs were tested with solutions containing various concentrations of NaCl. This step's objective was to characterize the response of the RI sensor so that a comparison could be made between the results obtained before and after cascading. The RI of each NaCl solution was recorded using an Atago PAL-RI refractometer. As the NaCl concentration increases from 0.0 M to 1.0 M, the RI increases as well.

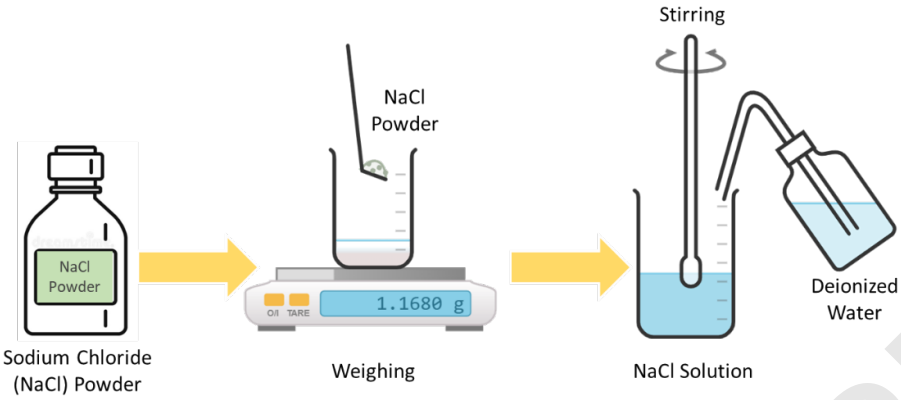

Figure 3.10: NaCl solution sample preparation.

Table 3.2: NaCl concentration and its corresponding refractive index value.

Solid NaCl (g)	Deionized Water (mL)	NaCl Solution (M)	Refractive Index (RI)
0.000	20	0.0	1.3322
0.2338	20	0.2	1.3337
0.4675	20	0.4	1.3348
0.7013	20	0.6	1.3360
0.9350	20	0.8	1.3378
1.1688	20	1.0	1.3389

Figure 3.11 shows the experimental setup that is comprised of EDFA as a light source, SMTF, U-groove platform, and OSA. Initially, the SMTF was secured on the U-groove platform and inserted in between the two aforementioned equipment. A micropipette was used to transfer the prepared NaCl solution onto the tapered region. The SMTF was rinsed three times with deionized water to wash away the residual substance. Figure 3.12 (a) and (b) depict the output spectra of SMTF1 and SMTF2 when introduced to NaCl solutions containing various RIs. Using the wavelength shift produced by calculating the difference between the original wavelength of a fringe

observed in a 0 M NaCl solution and the new wavelength of the same fringe in NaCl solutions of varied RI, the effect of varying RI on SMTFs was analyzed. As predicted by theory, as the concentration grows from 0 M to 1.0 M, the wavelength shifts to the right due to the increase in the effective RI of the cladding, n_{eff}^{c}. As n_{eff}^{c} increases, the differences (Δn_{eff}) between the effective RI of the core and its external surroundings will decrease, according to equation 2.2. This shows that when the wavelength shift exceeds the FSR, there will be an overlapping in the output spectra. Consequently, by subjecting the tapered region to varying concentrations of NaCl, the n_{eff}^{c} is modified, which in turn affects the initial relative phase of the spectrum. This modification induces a discernible shift or spacing of fringes in the spectral response.

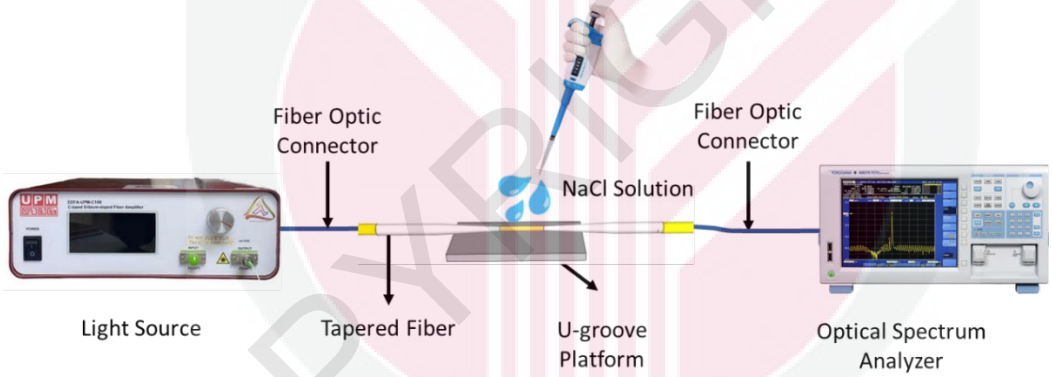

Figure 3.11: Employ the optical deposition technique to analyze the properties of NaCl.

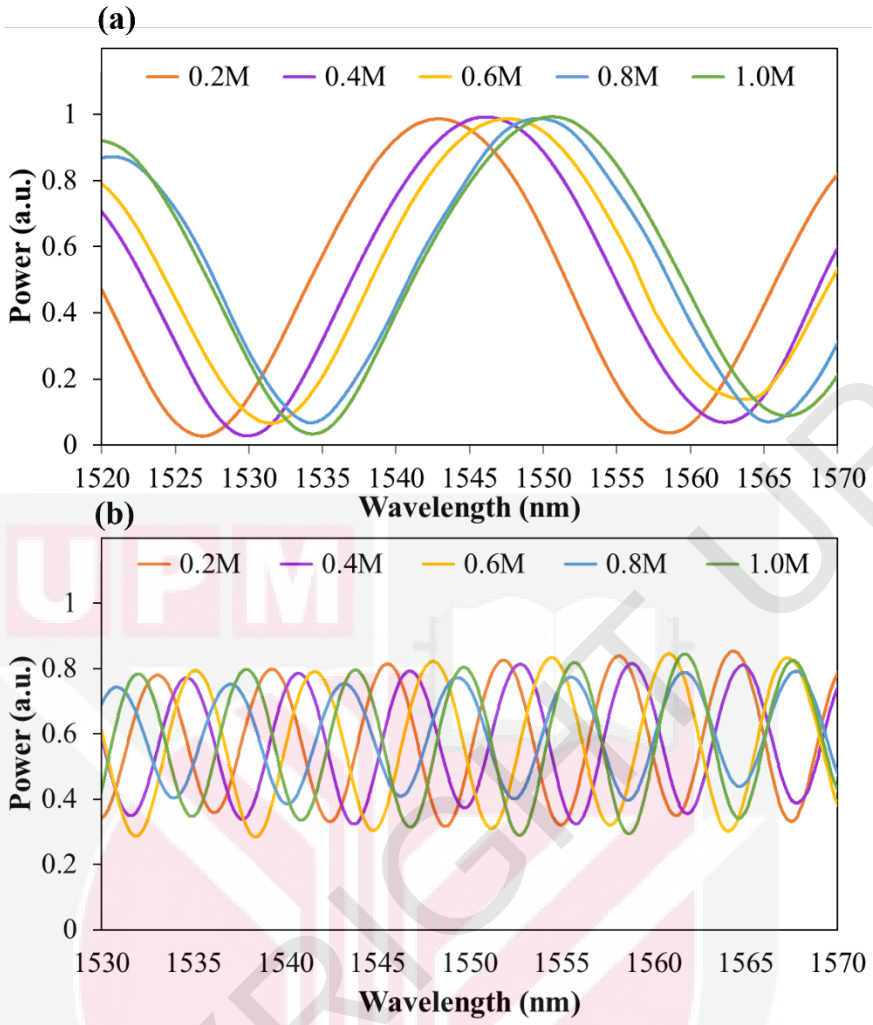

Figure 3.12: Output spectra of pre-cascaded for (a) SMTF1 and (b) SMTF2 towards RI.

Figure 3.13 depicts the wavelength shift in relation to RI for SMTF1 and SMTF2. It is evident from the graph that the wavelength shifts for both SMTFs increase linearly with the increase of RI from 1.3322 RIU to 1.3389 RIU. When the RI changes from 1.333 RIU to 1.3780 RIU, the greatest wavelength shifts for SMTF1 and SMTF2 are 14.93 nm and 10.92 nm, respectively. Based on the graph, SMTF1 has a linear trend line with a correlation coefficient of 0.9981 and a sensitivity of 1418.7 nm/RIU for its linear curve gradient. The linear trend line of SMTF2 has a correlation coefficient of R^2 = 0.9974, and the attained sensitivity is 1876.5 nm/RIU. Both SMTFs have excellent linearity because the points overlap the trend line in a manner that permits

linear fitting of almost 1. With a larger WD, the evanescent field has a shallower penetration depth, and a shorter WL makes the effective interaction area less, leading to lower sensitivity for SMTF1 [76]. All the experiments were repeated thrice to generate error bars of wavelength shift presented in Figure 3.13.

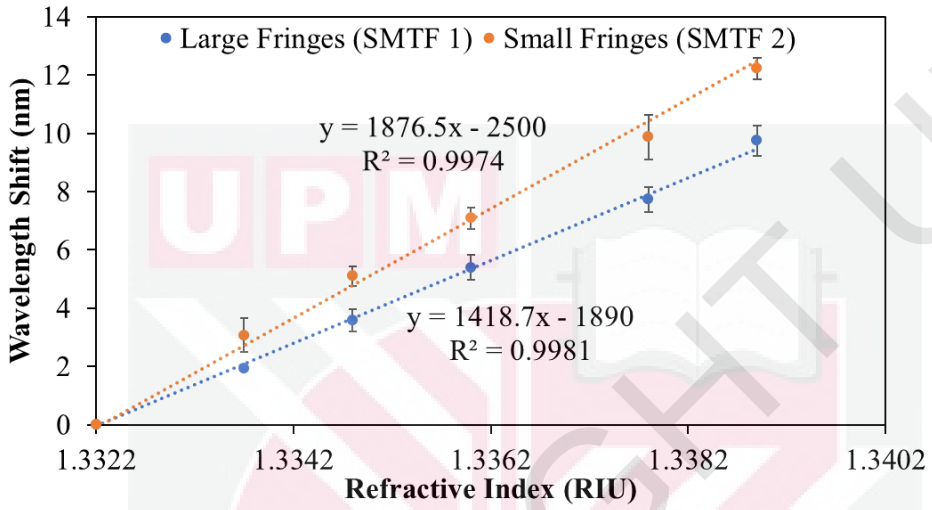

Figure 3.13: Trend lines depicting the correlation between wavelength shift and different refractive index (RI) concentrations for SMTF1 and SMTF2.

3.5 Fabrication and Characterization of Cascaded SMTF

Figure 3.14 illustrates the experimental setup for cascaded SMTF characterization. SMTF1 and SMTF2 were put on U-groove platforms 1 and 2, respectively. Both SMTFs were spliced together, as illustrated by point "X" in Figure 3.15. The spacing between the tapers was not considered during the design process due to the size restriction imposed by the U-groove sample platform.

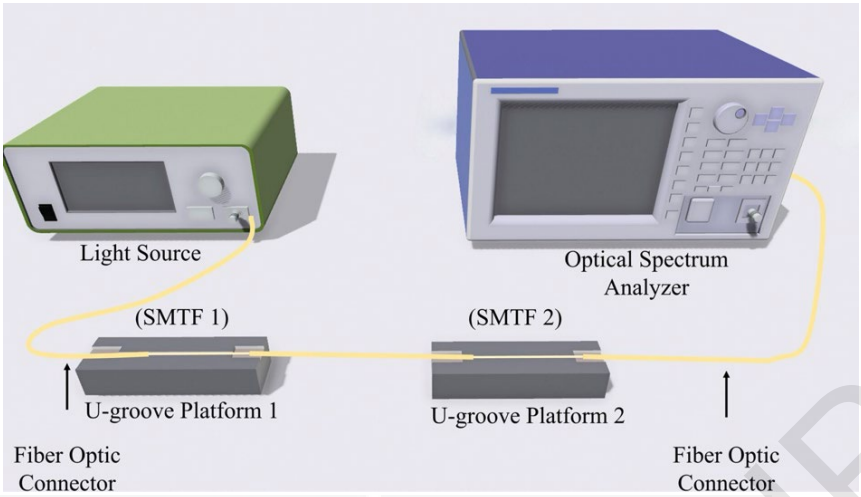

Figure 3.14: Experimental setup of cascaded SMTF.

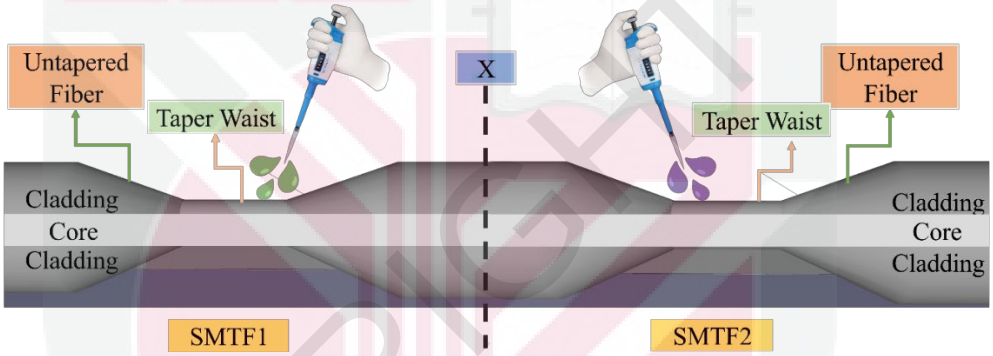

Figure 3.15: Cascaded SMTF point.

As light travels through the SMTF, it coupled to higher-order modes. When these modes interact, they generate a series of interference fringes, as presented in Figure 3.16. The two combined fringes, one of which has shorter fringes spacing that lies inside the larger fringes of the cascaded structure creates a periodic interferometry pattern due to the light interference. Higher-order modes will be excited and propagate down the tapered region when light moves from the fiber to the down-taper section of SMTF1. The phases interfere and the modes reunite at the end of the tapered region. The output light from SMTF1 then has a comb-like spectrum because of the interference of the modes. This light, is now the new fundamental mode, keeps moving into SMTF2. In SMTF2, the same interference and excitation phenomena seen in

SMTF1 will occur too. As a result, a composite spectrum made up of small fringes superimposed within the large fringes was produced.

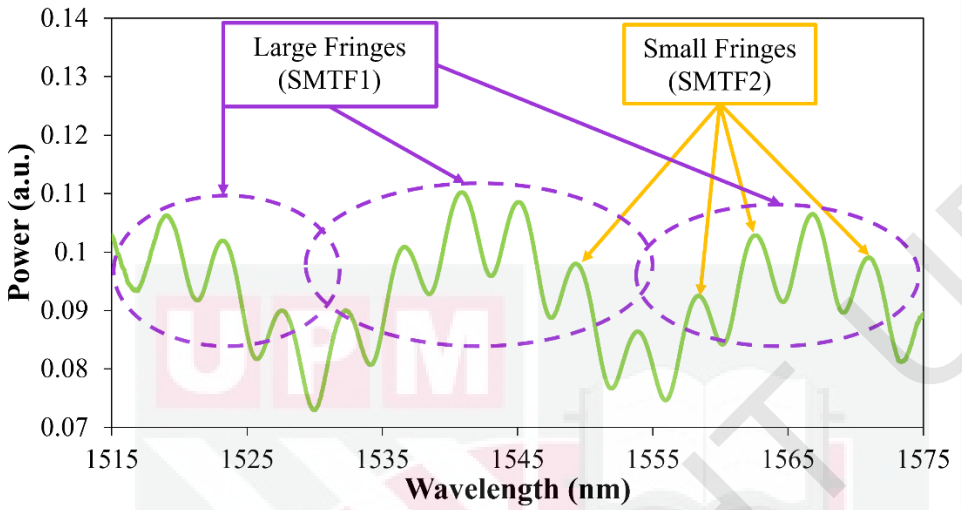

Figure 3.16: Output spectra of the cascaded SMTFs.

3.6 Cascaded SMTF Response Towards RI Variation

To observe and test the capability of simultaneously detecting two different RIs, the characterization of cascaded SMTFs is the backbone of the entire research. The procedures that were conducted were like the ones conducted to characterize individual SMTFs. There were 4 separate sets of experiments tabulated in Table 3.3, each representing a unique sequence of inserting the RIs solution into the sample holders.

Table 3.3: 4 sets of different experiments for NaCl.

	NaCl (M)							
	SET 1		SET 2		SET 3		SET 4	
NO	SMTF 1	SMTF 2	SMTF 1	SMTF 2	SMTF 1	SMTF 2	SMTF 1	SMTF 2
1	0.0	0.0	0.0	0.0	1.0	0.0	0.0	0.0
2	0.0	0.2	0.2	0.0	0.8	0.2	0.2	0.2
3	0.0	0.4	0.4	0.0	0.6	0.4	0.4	0.4
4	0.0	0.6	0.6	0.0	0.4	0.6	0.6	0.6
5	0.0	0.8	0.8	0.0	0.2	0.8	0.8	0.8
6	0.0	1.0	1.0	0.0	0.0	1.0	1.0	1.0

For set 1, SMTF1 was immersed and fixed in deionized water, equivalent to a 0.0 M NaCl solution, while SMTF2 was exposed to a range of NaCl concentrations from 0.0 M to 1.0 M. In set 2, deionized water was fixed at SMTF2, and various concentrations of NaCl solution were added to SMTF1. In experiment set 3, the NaCl concentration in both SMTFs varied in a manner that contrasted with set 4, where the solution concentration for both tapers gradually increased. Each set of experiments was repeated three times to determine average readings and assess repeatability.

Experiment set 1 output spectra for cascaded SMTFs are shown in Figure 3.17 (a), and the corresponding wavelength shift of small fringes with a different RI solution is shown in Figure 3.17 (b). Since only SMTF2 was immersed in the various RIs solutions, only the average wavelength shift of the small fringe was analyzed. As RI increases, a clear rightward shift in the small fringes is seen, while the large fringes

show only slight changes. The graph's linearity, R^2, is 0.9954, and its sensitivity gradient is 1493.8 nm/RIU. Error bars reflect the SD from the triplicates exhibiting errors smaller than 0.9 nm. This is probably because of how easily SMTF is influenced by its surroundings. Consequently, slight variations in temperature and strain introduce tiny changes during experiments.

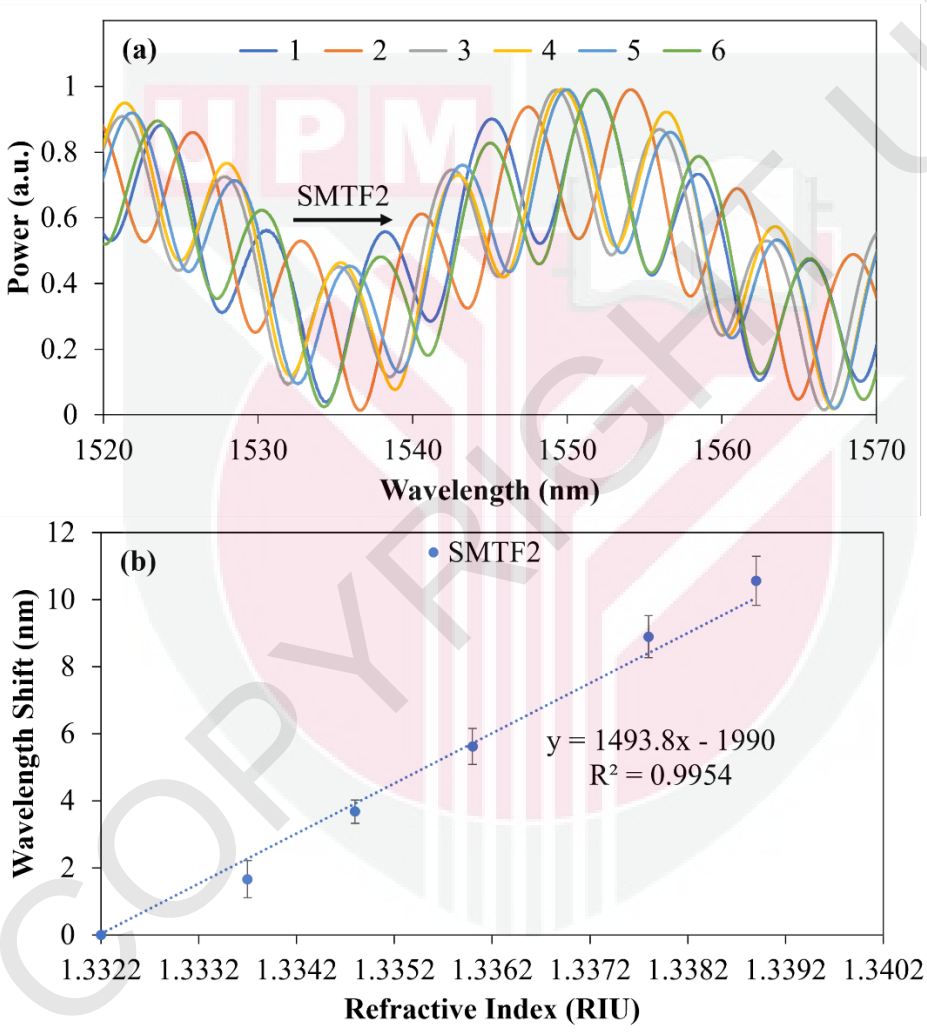

Figure 3.17: Output spectra cascaded SMTFs average (a) wavelength shift of (b) small fringes against RI for Experiment set 1.

Experiment set 2 output spectra for cascaded SMTFs are shown in Figure 3.18 (a), and the corresponding average wavelength shift of large fringes with a change in RI solution is shown in (b). In Experiment 2, SMTF2 was held at 1.3322 RIU while SMTF1 was immersed in a different RI solution. Upon comparing the dips in the spectral responses with the increasing concentration of NaCl, an observation of a red shift was made. This is because when concentration increases, so does RI. From 1.3322 RIU to 1.3389 RIU, it shows that the wavelength shift for large fringes gradually increases from 0 nm to 6.971 nm. There is a linearity of 0.9967 and a sensitivity of 1013.4 nm/RIU with the SMTF1. The low average SD value of 0.89 signifies minimal variability of errors, which further enhances the sensor's reproducibility. Because the sensitivity of all three sensors is close to the average value, the sensor has a high probability of producing a constant sensitivity for any repeated experiment.

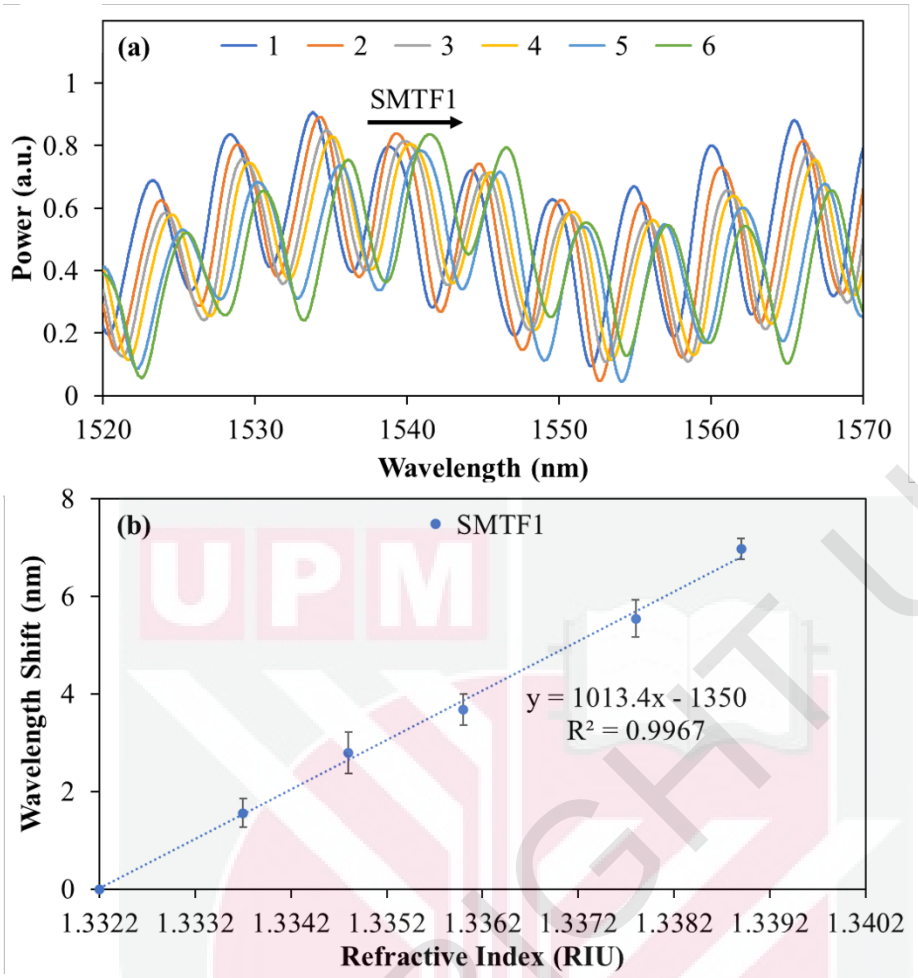

Figure 3.18: Output spectra cascaded SMTFs average (a) wavelength shift of (b) large fringes against RI for Experiment set 2.

Figure 3.19 (a) and (b) display the output spectra for cascaded SMTFs and the corresponding wavelength shifts of large and small fringes, respectively, when a different RI solution is utilized in Experiment set 3. Large fringes in the output spectra shift to the left when SMTF1 is immersed in decreasing RI solutions and small fringes shift to the right when SMTF2 is immersed in increasing RI solutions. The RI sensitivity achieved by SMTF1 is 915.75 nm/RIU, while SMTF2's sensitivity is 1343.6 nm/RIU. Both SMTF1 and SMTF2 have linearities of 0.9853 and 0.9952, respectively. Since the overlapping shifts of small and large fringes influenced the analysis and generated inconsistency between the data, the linearity of SMTF1 in Experiment set 3

is lower compared to prior experiment sets. SMTF1 had an SD of 0.89 meanwhile SMTF2 had an SD of 1.07. Furthermore, the spectral curve is shifted to longer wavelengths when the RIU of the sensing medium is increased. Resonance wavelength is found to increase with increasing RI of the sensing medium.

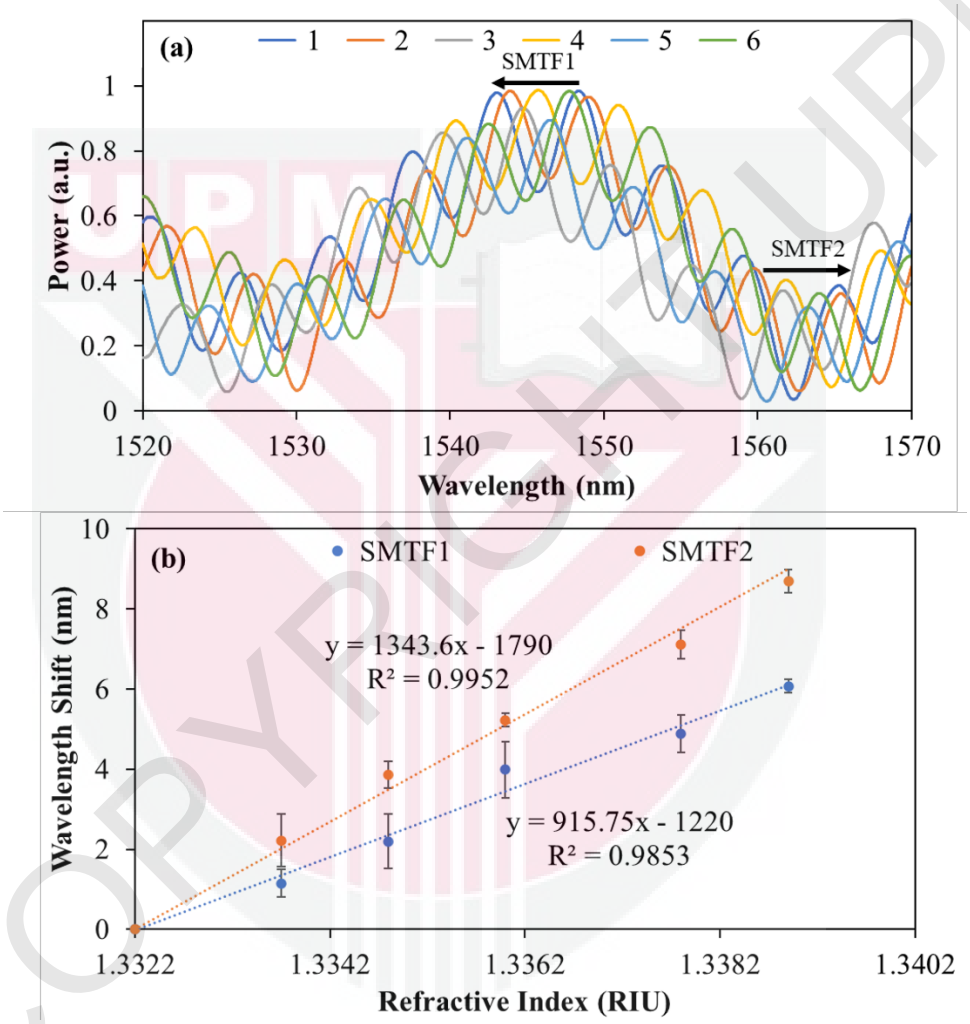

Figure 3.19: Output spectra cascaded SMTFs average (a) wavelength shift of (b) large fringes and small fringes against RI for Experiment set 3.

The output spectra of the cascaded SMTFs and the wavelength shifts of large and small fringes when using a different RI solution for Experiment set 4 are illustrated in Figure 3.20 (a) and (b), respectively. After being immersed in the same increasing RIs solution, SMTF1 and SMTF2 in Experiment 4 produced spectra with a right shifting of wavelength for both large and small fringes. SMTF1 has a sensitivity of 975.81 nm/RIU, while SMTF2's is 1441.3nm/RIU. Both SMTF1 and SMTF2 exhibit linearity greater than 0.99. SMTF1 and SMTF2 have SD values of 1.03 and 1.32, respectively. The sensitivity for SMTF1 is lower than SMTF2 due to the larger WD, which reduces the penetration depth of the evanescent field [77].

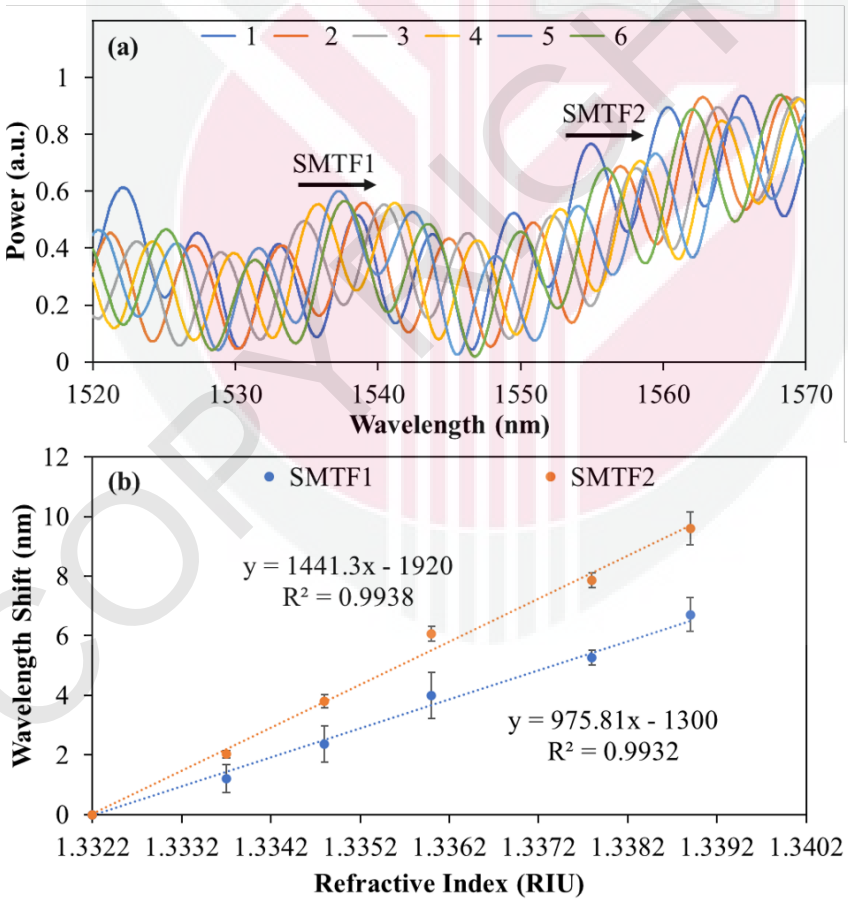

Figure 3.20: Output spectra cascaded SMTFs average (a) wavelength shift of (b) large fringes and small fringes against RI for Experiment set 4.

Table 3.4 displays the experimentally obtained levels of sensitivity for SMTF1 and SMTF2. Results show the sensitivity of the single SMTF is greater than that of the cascaded SMTFs. Sensitivity greater than 1340 nm/RIU was reached by SMTF2 in all experiments; however, sensitivity less than 1340 nm/RIU was obtained by cascaded SMTFs for SMTF1. Since SMTF are particularly sensitive to strain and temperature, the values of RI in different studies may vary. The outcomes may therefore change with even little shifts in these two factors. The significant discrepancy between SMTF1 and SMTF2 results was caused by the fact that SMTF1 has a larger FSR in cascaded configuration than SMTF2. This larger FSR reduces the visibility of fringes, resulting in a lower sensitivity in comparison to SMTF2 with a smaller FSR [78]. Since overlapping spectra made it hard to identify the shifts, the method of analysis could also influence the results. The sensitivity of SMTF1 is comparatively lower than that of SMTF2 because of its greater WD, which leads to a decrease in the depth of penetration of the evanescent field, improved fringe visibility, and potential for stronger signal enhancement [77].

Table 3.4: Analyzing the effects of waist length and waist diameter on FSR performance.

	Experiment (nm/RIU)				
SMTF	**Single SMTF**	**Set 1**	**Set 2**	**Set 3**	**Set 4**
1	1418.70	-	1013.40	915.75	975.81
2	1876.50	1493.80	-	1343.60	1441.30

The cascaded SMTFs generated a periodic interferometry pattern with two combined fringes consisting of both large and small fringes. Under several sets of trials, the performance of cascaded SMTFs was evaluated; it is feasible to determine the RI changes that occurred to a specific SMTF based on changing fringes. The sensitivity of cascaded SMTFs is lower than that of pre-cascaded SMTFs. The study of the results revealed that cascaded SMTFs can simultaneously detect two distinct RIs.

3.7 Summary

This chapter demonstrated SMTF fabrication and characterization. Waist region of SMTF affect output spectrum properties. According to the theory, the two acceptable parameters for cascaded SMTF are those that produce large fringes with FSR greater than 16 nm and those that generate small fringes with FSR less than 5 nm. The results led to the selection of two taper profiles: SMTF1, with a WD of 12 μm and a WL of 5 mm, and SMTF2, with a WD of 10 μm and a WL of 20 mm. This chapter also included NaCl-based RI characterization to investigate and evaluate the performance of the cascaded SMTF sensor for dual-detection simultaneously.

CHAPTER 4

CASCADED SINGLE-MODE TAPERED FIBER BIOSENSOR FOR SIMULTANEOUS DETECTION OF DENGUE AND SARS-COV-2 VIRUSES

4.1 Introduction

The experimental processes involved in the preliminary investigation, optimization and development of the cascaded SMTF biosensor for simultaneous detection of dengue and SARS-CoV-2 viruses described in depth in this chapter. The subsequent subchapters provide a detailed explanation of the discussions, ensuring the research's success. The preparation, experimental setup, and observed parameters are covered in this chapter.

4.2 Research Planning

Research planning in a flowchart shown in Figure 4.1. Preliminary investigation and optimization of the surface modification method were firstly conducted with the Biotin-Avidin system. Completion and success of the aforementioned preliminary study would be followed by functionalization process using chemical solutions like hydroxylation with sodium hydroxide (NaOH), silanization with (3-Aminopropyl) triethoxysilane (APTES), and activation using glutaraldehyde (Glu). The functionalized and immobilized antibody that matches it was attached to the cascaded SMTFs. After the antibody was successfully attached to the cascaded SMTFs, the sensor was used and tested with different concentrations of a single disease. The performance evaluation of the sensor would then commence with the use of multiple diseases, in this case, DENV II E and SARS-CoV-2 S protein. By observing the sensor's reaction to changing concentrations of both diseases, the sensitivity,

resolution, LOD, and affinity towards the targeted determinant would be assessed. The detailed process and outcome of the steps are explained in the following subsections.

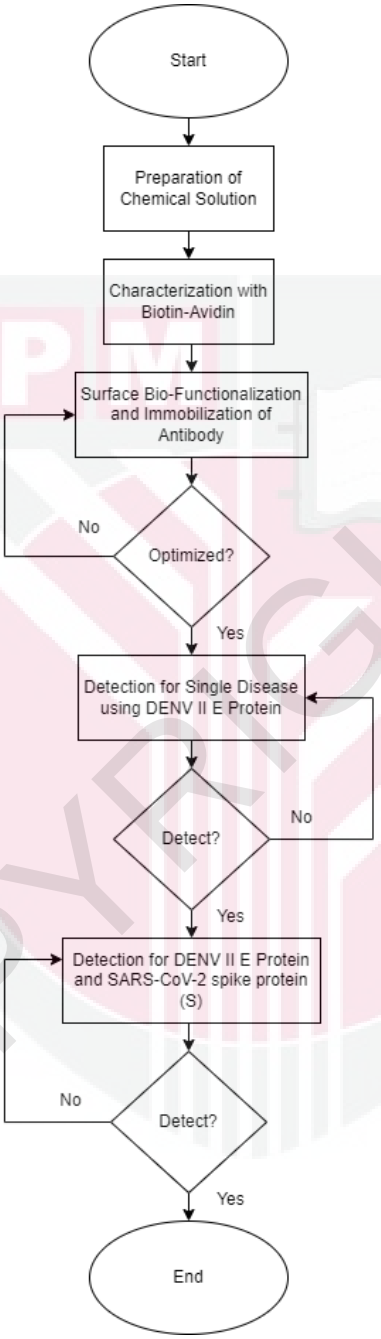

Figure 4.1: Flowchart of the experiments conducted for the dual-disease detection of DENV II E and SARS-CoV-2 S proteins.

4.3 Characterization of Cascaded SMTF Surface Functionalization with Silane-PEG-Biotin and Detection of Avidin

Biotin and avidin are two molecules that have an extremely strong attraction to one other. The biotin-avidin system is a molecular diagnostics benchmark that is used in purification and detection procedures with a dissociation constant of about $10^{-15}\ M$ [79]. Due to a protein and protein-specific antibody limited availability, biotin-avidin was used to imitate bio-recognition molecule functionalization onto the tapered surface and complementary determinant detection. This is a preliminary investigation into the potential of bio-recognition molecule functionalization on the SMTF for sensing certain determinants.

The surface of the fiber was activated with 1.0 M NaOH (Sigma Aldrich) to immobilize the bio-recognition molecule, biotin, on the SMTF. 10 mL of deionized water was used to dilute 0.04 g of powdered NaOH [40]. Following 50 minutes, the SMTF underwent three rinses using deionized water before being left to dry.

95% ethanol and 5% deionized water were used to dilute a 0.1 M stock solution of silane-PEG-biotin. The silane-PEG-biotin solution was inserted into the groove of the sample holder until the tapered region was immersed. According to the manufacturer's instructions, 30 minutes should be sufficient for incubation [54]. The silane agent would condense during incubation, linking to the fiber surface's hydroxyl groups via hydrogen bonds.

The powdered avidin was dissolved in pH 7.4 PBS to make the avidin solution. avidin incubation was 15 minutes per the manufacturer's recommendation [54]. Total of 3 sets of cascaded SMTFs sensors were tested at each concentration to evaluate their repeatability and accuracy. Figure 4.2 depicts the schematic mechanism of the biotin-avidin reaction on the SMTF.

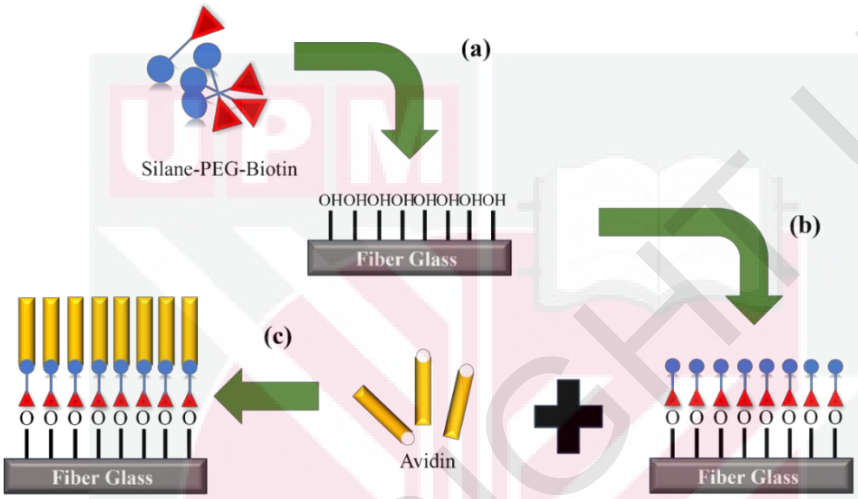

Figure 4.2: Schematic diagram for (a) functionalization and (b) immobilization of silane-PEG-biotin, and (c) detection of avidin.

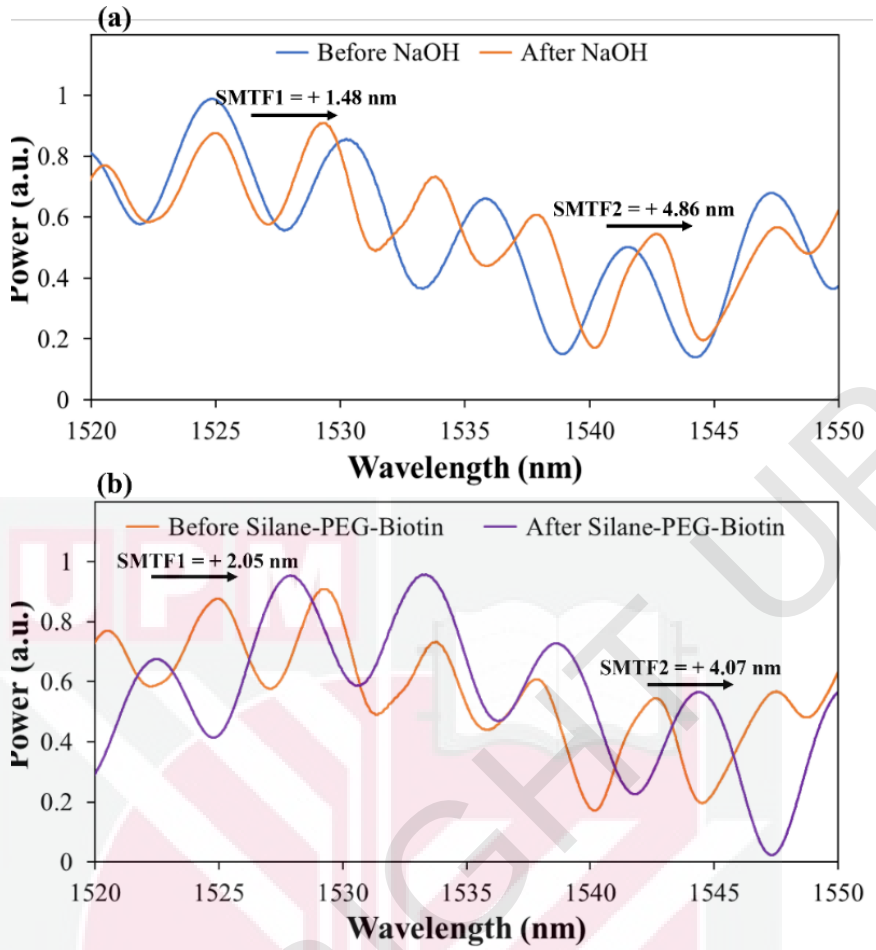

Figure 4.3: Spectra response when (a) NaOH of (b) silane-PEG-biotin were introduced to the cascaded SMTFs.

The hydrolysis of SMTF in silane solution caused silane-PEG-biotin to adhere to it. An additional layer on the SMTF surface increases RI, causing a spectrum shift on the OSA. In Figure 4.3 (a), spectra responses before and after the introduction of NaOH were compared. A red shift of 1.48 nm for SMTF1 and 4.86 nm for SMTF2 was observed after NaOH was inserted. In Figure 4.3 (b), it was noted that the spectrum shifted to the right by 2.05 nm for SMTF1 and 4.07 nm for SMTF2 after the functionalization of silane-PEG-biotin. Simply stated, these red shifts represent the increase in RI surrounding the SMTF as a result of layers being added to the fiber. This is by equation 2.1 and 2.2. The observation confirms silane-PEG-biotin surface activation and functionalization on the SMTF. To evaluate the performance of the

proposed sensor, 3 sets of experiments were performed using cascaded SMTFs, referring to Table 4.1, and each one was exposed to a different concentration of avidin ranging from 0.2 μM to 1.0 μM. After 15 minutes, the SMTF were rinsed three times with deionized water to remove any remaining residues before drying. To ascertain the sensor's accuracy and precision, this series of tests was carried out three times.

Table 4.1: 3 sets of different experiments for silane-PEG-biotin and detection of avidin.

NO	Avidin (μM)					
	SET 1		SET 2		SET 3	
	SMTF1	SMTF2	SMTF1	SMTF2	SMTF1	SMTF2
1	0.0	0.0	0.0	0.0	0.0	0.0
2	0.0	0.2	0.2	0.0	0.2	0.2
3	0.0	0.4	0.4	0.0	0.4	0.4
4	0.0	0.6	0.6	0.0	0.6	0.6
5	0.0	0.8	0.8	0.0	0.8	0.8
6	0.0	1.0	1.0	0.0	1.0	1.0

The corresponding wavelength shift was observed based on the spectra response in Figure 4.4. For both experiments in set 1 and set 2, it yields a coefficient correlation value of 0.9997 and 0.9987 for SMTF2 and SMTF1. When both SMTFs increase gradually in experiment set 3, R^2 for both is above 0.9985. The R^2 for all spectral shift responses are also remarkably high, indicating that the linear fit is a good representation of the data. This demonstrates a clear relationship between concentration and red shifts as higher concentrations lead to a shifting of peaks towards longer wavelengths. The observed phenomenon is consistent with equation. 2.1 and

2.2, as the increase in concentration is directly proportional to the increase in RI, leading to the observed outcome. The sensitivity of the sensor for all sets of experiments obtained at a value of ≈ 6.4 nm/μM with SD of ± 1.45 for SMTF1 meanwhile sensitivity for SMTF2 obtained a value of ≈ 9.3 nm/μM with SD of ± 1.78. SMTF2 has more sensitivity than SMTF1 (c). This is because the evanescent field at the sensor surface is higher for SMTF2, compatible with the fact that it has a smaller WD [77].

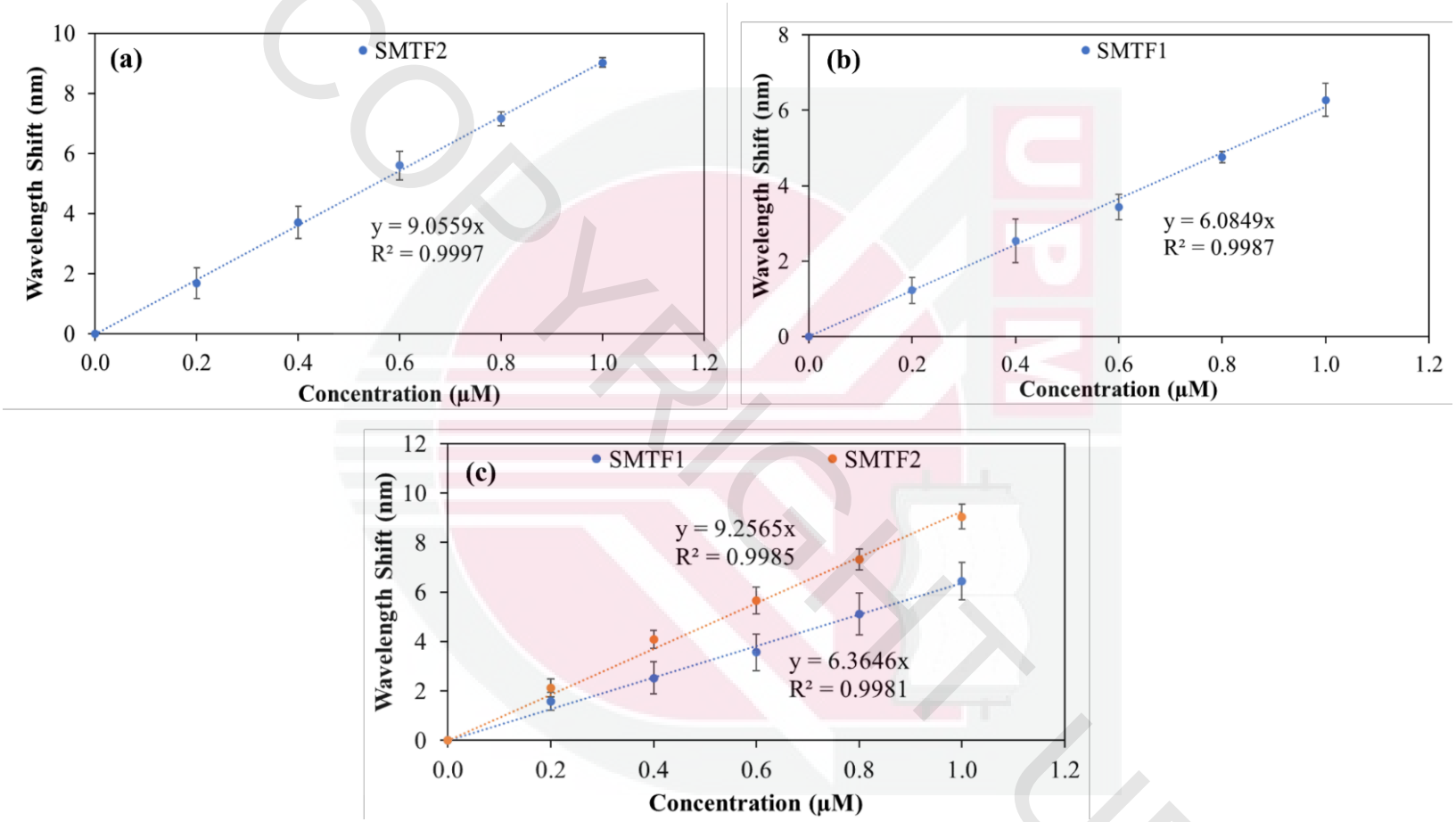

Figure 4.4: Trend line exhibiting the correlation between wavelength shift and avidin concentration for the experiment in (a) set 1, (b) set 2, and (c) set 3.

4.4 Surface Bio-functionalization and Antibody Immobilization

Following preliminary testing with biotin and avidin, SMTF demonstrated good feasibility in sensing specific protein molecules after being functionalized with bio-recognition molecules. To detect DENV II E and SARS-CoV-2 proteins, specialized monoclonal antibodies (MAbs) will be utilized and attached to the surface of SMTF as biorecognition molecules. Similar functionalization and immobilization steps are implemented as in the preliminary investigation.

4.4.1 Preparation of Chemical Solution for Functionalization

The hydroxylation technique was used to start the functionalization process. 20 mL of deionized water was mixed with 0.08 g of NaOH to prepare 0.1 M NaOH. It was then left to immerse at room temperature for 50 minutes [54]. The initial procedure involves coating the SMTF surface with hydroxyl (-OH) functional groups, which will facilitate the subsequent silanization process. To get rid of unattached molecules, the tapered area was washed three times with deionized water following a 50-minute incubation period. After that, it was left to dry for 5 minutes at room temperature (24℃).

The hydroxylation process was validated using Raman spectroscopy (Alpha 300 R, WITec) on the tapered surface at an excitation wavelength of 532 nm. Figure 4.5 shows significant peak values at 970 cm^{-1}, 1040 cm^{-1}, 1100 cm^{-1}, and 1200 cm^{-1}, showing the presence of Si-OH, Si-O-, and SiO_4, respectively [80]. These oxygenated linkages are known as siloxane and silanol, and both will aid in the following silanization process.

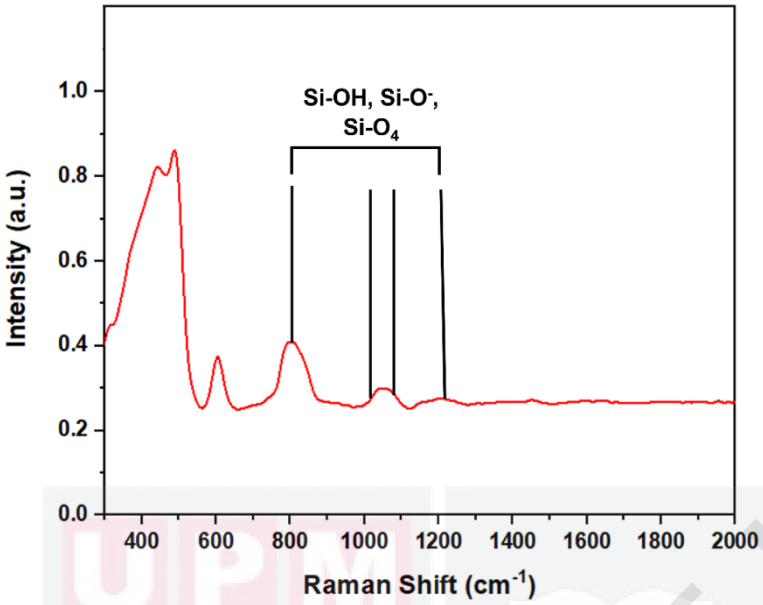

Figure 4.5: Analysis of the Raman spectrum of a SMTF following a hydroxylation process.

The process of silanization was then initiated by adding the hydroxylated tapering region to APTES. The goal of adding APTES to the hydroxylated surface was to link inorganic and organic compounds [81]. It was chosen for its amine functional group content, and it is the main component that facilitates the immobilization of DENV II E and SARS-CoV-2 S protein-specific antibodies onto the surface of the SMTF [54]. APTES structural formula is depicted in Figure 4.6.

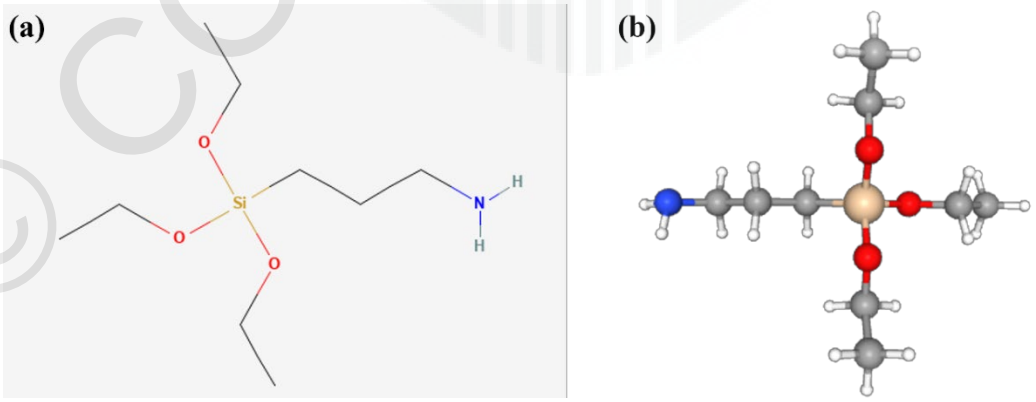

Figure 4.6: Structural formula of APTES in (a) 2-Dimensional and (b) 3-Dimensional.

The hydroxyl groups are responsible for removing the ethoxy group of the APTES to facilitate the hydrolysis of ethoxy groups, leaving the APTES with hydroxyl groups that are ready to attach to the surface. The process would place the APTES molecule where the amino group is visible, giving the SMTF's surface an aminopropyl terminal [82]. Figure 4.7 illustrates the silanization reaction schematically. Silanization began by incubating the tapered area for 45 minutes with APTES/deionized water (2% v/v from Amresco), similar to prior studies [54]. After 45 minutes, the SMTF was cleaned three times with deionized water to remove unattached molecules and dried at room temperature.

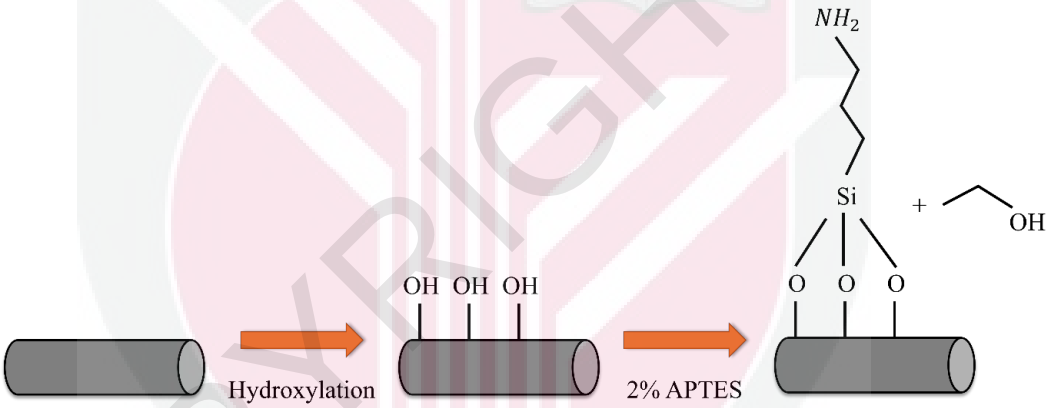

Figure 4.7: APTES is subsequently deposited onto the surface of the SMTF after its hydroxylation with NaOH.

Raman spectra following silanization are shown in Figure 4.8. The Si-O-Si and Si-O- vibrational modes are shown by the peaks at 486 cm^{-1} and 1040 cm^{-1} [81]. This indicates a covalent bond between the silane agent and the hydroxylated SMTF surface. At 2930 cm^{-1}, there was another peak that showed the C-C skeletal structure of the connected APTES. The peaks at 1247 cm^{-1}, 1343 cm^{-1}, and 1605 cm^{-1} indicate the N-N, N-H, Si-NH_2, and NH_3^+ deformation vibrational modes, respectively [83].

These peaks demonstrate that the bent optical fiber's surface has amine groups and that APTES may attach to it.

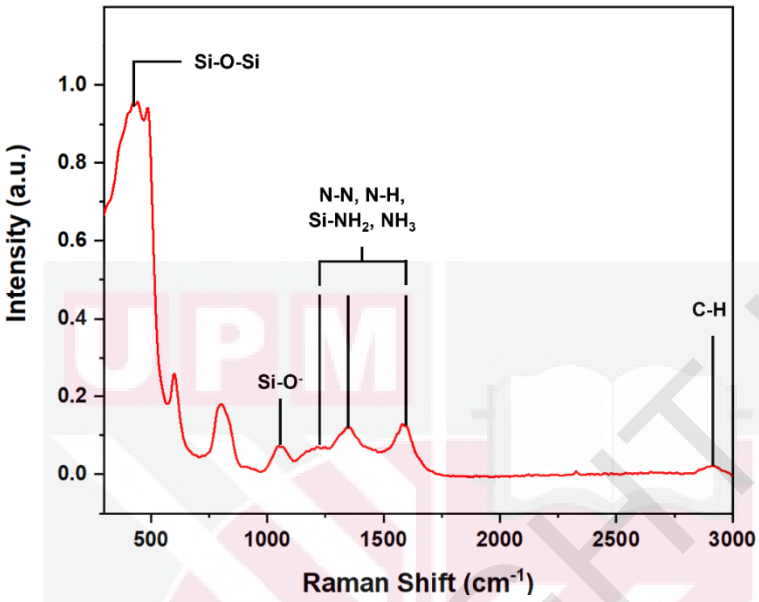

Figure 4.8: Raman spectrum of SMTF after being silanized using silane agent.

The tapered surface was activated with glutaraldehyde following the silanization procedure. Glutaraldehyde is a homo-bifunctional crosslinker with a 5-carbon skeletal backbone and two aldehyde terminals. The structural formula of the glutaraldehyde molecule is shown in Figure 4.9. Because aldehyde terminals are present, glutaraldehyde may react with primary amino groups, thiols, and phenols on enzymes and other proteins. Glutaraldehyde improves protein-protein and protein-support interactions by increasing molecular distance to minimize steric effects and conformational changes that could affect protein function [84].

(a) (b)

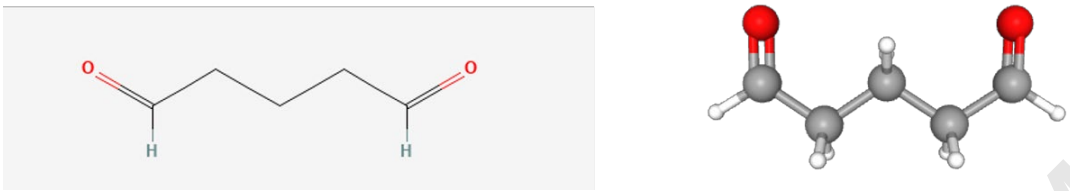

Figure 4.9: Structural formula of Glutaraldehyde in (a) 2-Dimensional and (b) 3-Dimensional.

The activation process is shown in Figure 4.10. Glutaraldehyde and the silanized surface of the SMTF will react to expose aldehyde groups that are prepared to form covalent bonds with the primary amines of the chosen protein antibodies, resulting in the formation of imine linkages. The initiation of the activation process was by injection of glutaraldehyde/PBS (2.5% v/v from Sigma Aldrich) into the sample holder until the tapered region was submerged in the solution for 45 minutes [54]. After 45 minutes, glutaraldehyde-layered optical fiber was permitted to dry at room temperature after being cleansed three times with deionized water to eliminate excess or unattached molecules.

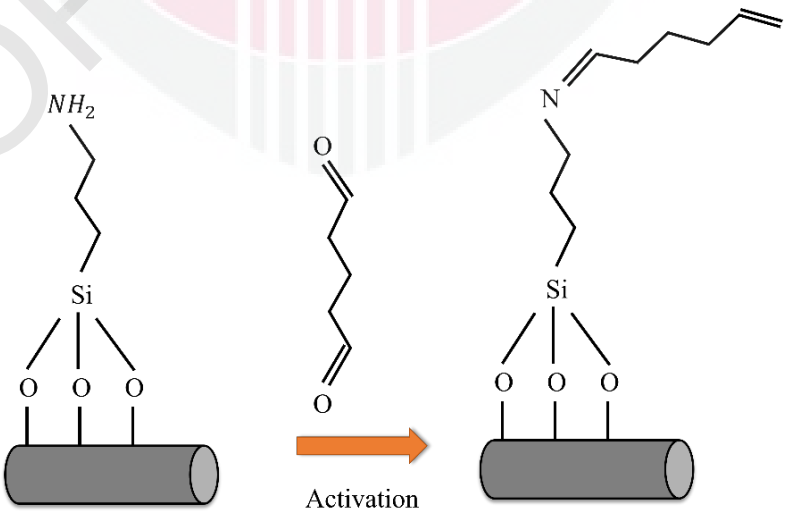

Figure 4.10: Activation process with glutaraldehyde on silanized surfaced of SMTF.

Figure 4.11 displays the Raman spectrum after the SMTF surface was activated with glutaraldehyde. The vibrational modes observed between 800 cm^{-1} to 980 cm^{-1} provide valuable insights into the skeletal structure of glutaraldehyde, the presence of the aldehyde functional group, and the formation of the amide bond with APTES [85]. The peak at 1611 cm^{-1}, 1660 cm^{-1}, and 1796 cm^{-1} refers to aldehyde functional group carbonyl structures, C=O, whereas 1330 cm^{-1} is linked to Amide I and Amide II bond vibrational modes [86]. Moreover, the peaks seen at 1461 cm^{-1} and 2930 cm^{-1} were induced by the methyl groups (C-H) [85]. This observation adds more evidence to support the activation of the SMTF surface by glutaraldehyde.

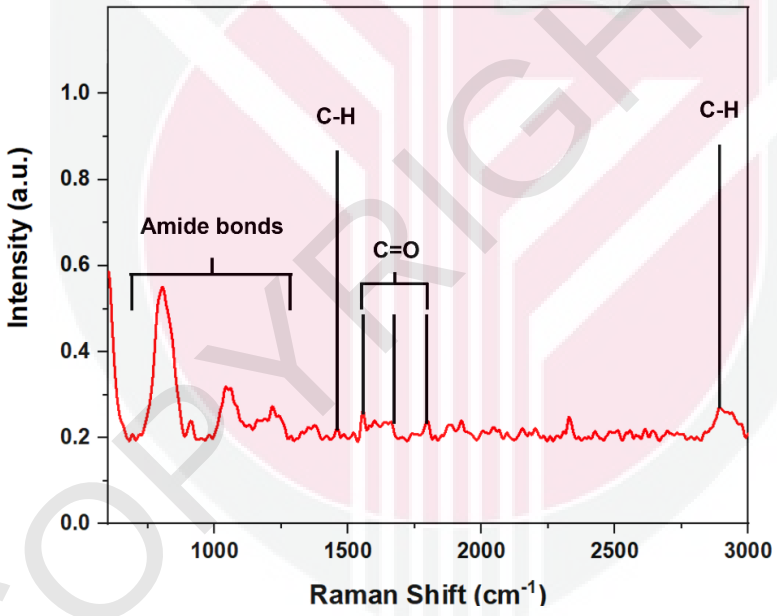

Figure 4.11: Raman spectra of glutaraldehyde-activated SMTF.

For both SMTFs, a Field Emission Scanning Electron Microscope (FESEM) was used to examine the SMTF at the end of each functionalization stage, taking note of its thickness and conformation. Figure 4.12 (i.-vi.) for SMTF1 shows that when the fiber was introduced to a new solution, its thickness increased consistently. After immersing a bare SMTF with a diameter of ≈ 12 µm in NaOH, an increase of ≈ 0.4 µm, or less, was noted. A slight increase was anticipated because hydroxyl groups were not thought to be particularly heavy. The immersion with APTES on the other hand yielded a net length of 0.8 µm, followed by 1 µm when glutaraldehyde was introduced, respectively. In Figure 4.12 (v.-vii.) for SMTF2, on the other hand, an increase of ≈ 0.4 µm was seen after NaOH was added using a bare SMTF that had a diameter of ≈ 10 µm. Incubating APTES, on the other hand, led to a net diameter of ≈ 0.8 µm while adding glutaraldehyde caused an increase of ≈ 0.9 µm. The SMTF's ability to exhibit a conformational shift indicates successful functionalization.

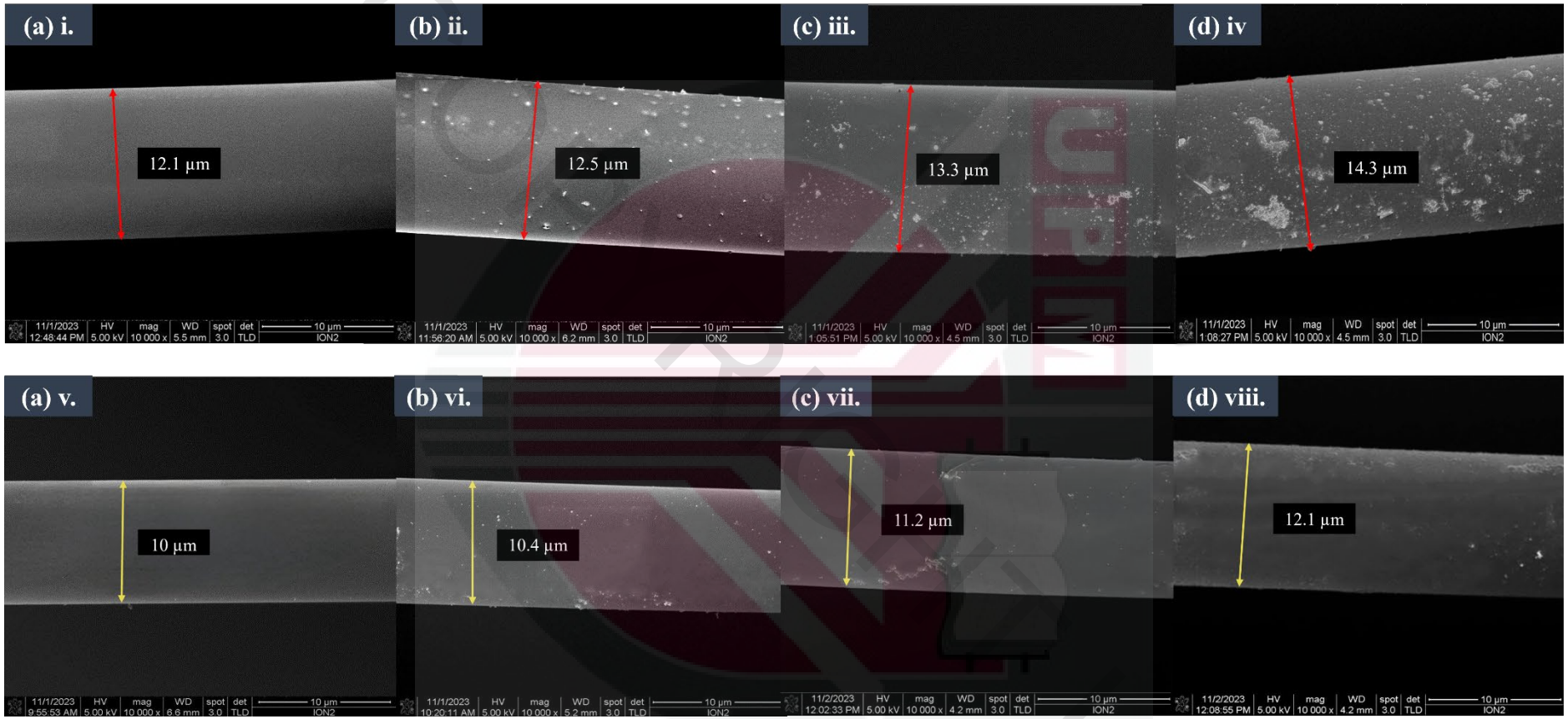

Figure 4.12: FESEM images of the SMTF at 5 kV and 10 K magnification for SMTF1 following the immersion of (a) bare, (b) NaOH, (c) APTES, and (d) glutaraldehyde for (i.-iv.) SMTF1 and (v.-viii.) SMTF2.

4.4.2 Functionalization of Cascaded SMTF

The immobilization of the antibody onto the SMTF determines the selectivity of the cascaded sensor. Antibodies are proteins that vertebrates create in reaction to specific chemicals. Immunoglobulin G (IgG) is an antibody with excellent antigen specificity that makes 10% to 20% of plasma protein in human blood and protects for months and years after being exposed to the antigen [87]. IgG antibodies are substantial globular proteins composed of four peptide chains and have an approximate molecular weight of 150 kDa shown in Figure 4.13. The structure is tetrameric and quaternary, with four identical chains: two large gamma chains (about 50 kDa) and two light chains (about 25 kDa) [88]. Fab fragment in the antibody is the antigen-binding portion. The domains of each heavy and light chain component are constant and changeable, respectively. The antigen-binding site, or paratope, is situated at the amino-terminal end of the monomer and is formed in large part by the domains. The Fc portion of an antibody, meantime, communicates with complement system proteins and Fc receptors found on cell surfaces. Antibodies possess a remarkable ability to activate the immune system [89]. Antibodies may take on one of four orientations when immobilized on a surface. Flat on, side on, tail on, and head on are the four possible positions. Flat-on orientation limits domain exposure, but the other three allow the antibody's Fab region to react with the target antigen because of the antibody's vertical orientation [90].

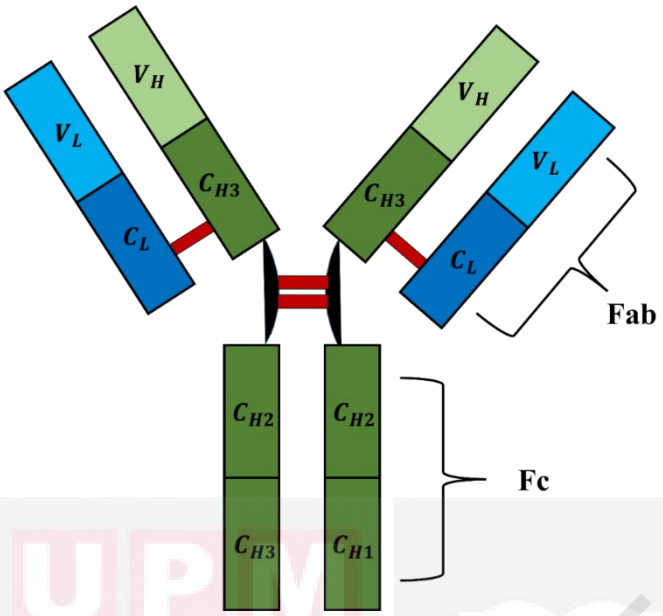

Figure 4.13: An illustration of an IgG antibody molecule.

4.5 Detection of Single Disease using DENV II E Protein with Biofunctionalized Cascaded SMTF

The selected antibodies should bind specifically to the target determinant; in this case, the DENV II E protein was utilized for the detection of a single disease due to its availability. These antibodies are well known as anti-DENV II E protein IgG antibodies or DENV II E protein-specific antibodies. As the Glutaraldehyde-activated optical fiber was carboxyl-terminated, it allowed a reaction with the primary group of the antibody, resulting in the formation of a strong covalent bond, which causes a very stable immobilization. As depicted in Figure 4.14, the reaction resulted in the immobilization of vertically oriented antibodies on the SMTF, allowing them to function as intended while maintaining their selectivity for DENV II E protein.

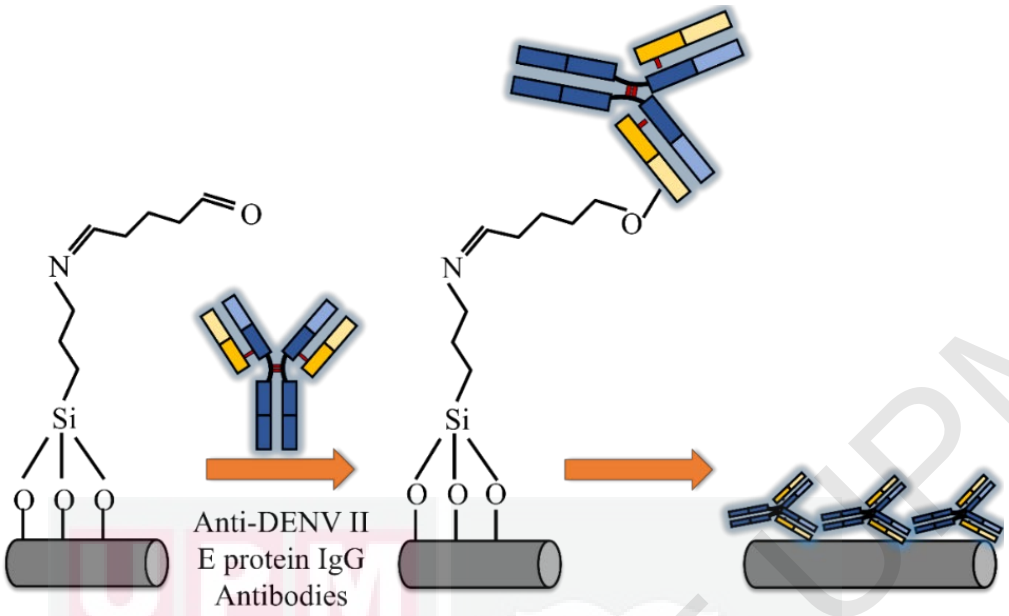

Figure 4.14: Anti-DENV II E protein antibodies are immobilized on the surface of an active, SMTF, resulting in a vertical dimension with exposed Fab regions in both SMTFs.

Anti-DENV II E protein IgG antibodies are used in both SMTFs in this study. To immobilize anti-DENV II E protein antibodies, a well-dried activated SMTF was immersed in 0.1 µM anti-DENV II E protein antibody (Meridian Life Sciences) diluted in PBS solution with a pH of 7.4 for 30 minutes [54]. Following immersion in an anti-DENV II E protein antibody solution for 30 minutes, the SMTF underwent three rinses to remove any unbound molecules. Subsequently, the fiber was allowed to dry at room temperature.

Using Raman spectroscopy, the presence of antibodies on the dried, immobilized, tapering optical fiber was verified. When compared to the literature, the recorded Raman spectra in Figure 4.15 correlated with that of an IgG molecule. The peak at 737 cm^{-1} has been ascribed to the tyrosine residues contained within the amino acid sequence of IgG, whereas 1307 cm^{-1}, 1517 cm^{-1}, and the area marked as 'b' originate from C-N, C-C, N-H, and terminal amino groups [91], [92]. Aside from that, a C=O

vibrational mode was observed around 1720 cm^{-1} to 1745 cm^{-1}, representing the carboxylic end of the IgG molecule [93]. Raman peaks at the region marked as 'a', 1450 cm^{-1}, and 2930 cm^{-1} were attributed to vibrational modes of C-H bonds, whereas 1000 cm^{-1} was referred to the Si-O- a group that was produced during the silanization process [83], [86].

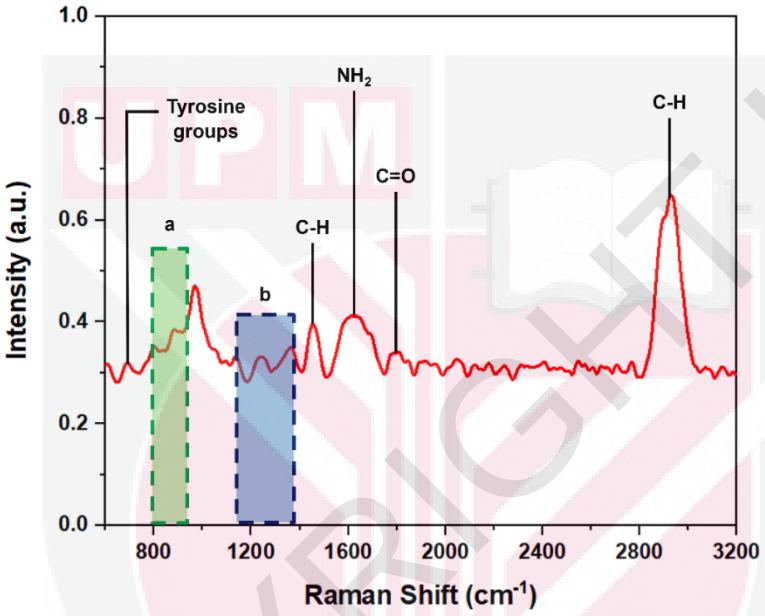

Figure 4.15: Raman spectra of a SMTF following immobilization with anti-DENV II E protein IgG antibodies.

Figure 4.16 exhibits a red shift following the completion of each surface functionalization phase. The introduction of the SMTF with APTES after hydroxylation with NaOH resulted in a rightward shifting of 1.49 nm for SMTF1 and 2.13 nm for SMTF2 from the initial peak. The red shift for both SMTFs was 0.24 nm and 0.96 nm when glutaraldehyde was added to the SMTF, then the peak was pushed farther by 2.05 nm and 2.84 nm when anti-DENV II E protein IgG antibodies were immobilized. The adherence of molecules onto the tapered surface caused the wavelength shift, which in turn increased the cladding's RI and decreased the Δn_{eff}

value. As stated in equation. 2.1 and 2.2 in Chapter 2, the reduction of Δn_{eff} has an impact on the phase shift of the spectrum, leading to a noticeable red shift in the observed spectra when compared. The red shift observed in both SMTFs can be attributed to variations in RI in the vicinity of a SMTF, as previously explicated.

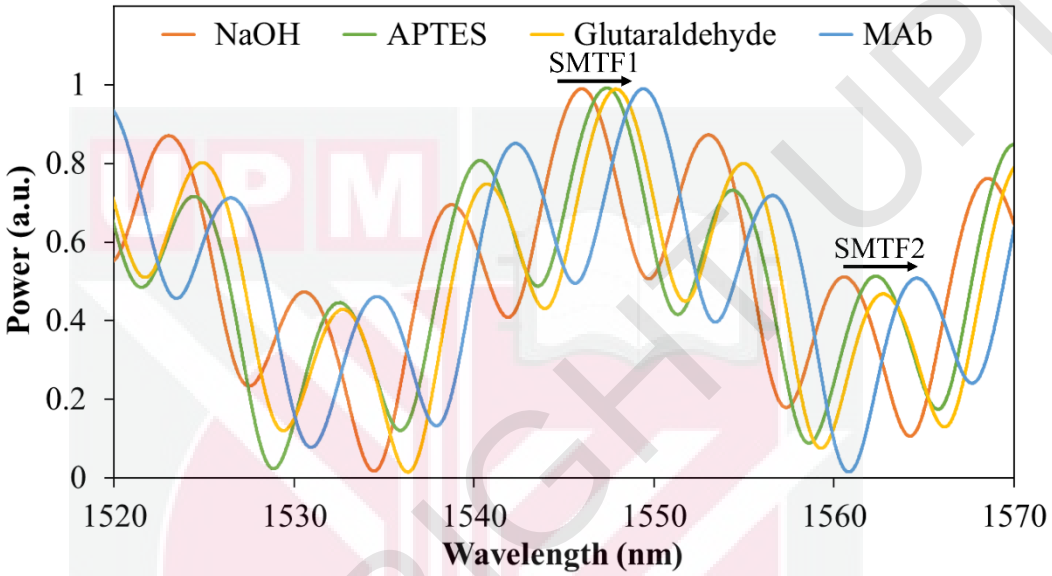

Figure 4.16: Spectra of output following incubation with glutaraldehyde, NaOH, APTES, and anti-DENV II E protein antibodies.

The DENV II E protein was introduced into an immobilized surface for SMTF1 and SMTF2. The goal of immobilizing anti-DENV II E protein antibodies onto a SMTF surface was to achieve selective recognition of E protein for the sensor. This is accomplished by the specific affinity for the E protein created to attach to SMTF, as shown in Figure 4.17.

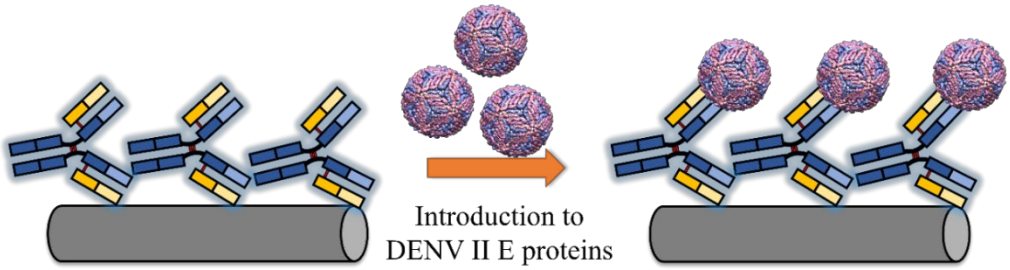

Figure 4.17: Anti-DENV II E protein antibody exhibits reactivity towards the DENV II E protein in both SMTF1 and SMTF2.

To begin DENV II E protein detection, DENV II E proteins (1nM) were introduced onto both SMTFs. Phosphate buffer solution at pH 7.4 was used to prepare DENV II E protein (Meridian Life Science) for incubation. The optimization method employed a fresh batch of functionalized SMTF. After around 15 minutes, the excess solution was pipetted out, and the tapered area was rinsed three times with deionized water to remove any residual molecules before drying at room temperature. Reading of the output spectra was taken using OSA. The spectra obtained before and after the introduction of DENV II E proteins demonstrate a significant red shift of 2.47 nm and 3.66 nm, respectively, for SMTF1 and SMTF2, shown in Figure 4.18.

The red shift observation, as discussed in earlier sections, was caused by a change in the RI on the external surroundings of SMTF. The sensor setup was evaluated with avidin (negative control) to eliminate any bias factors and analyze the specificity of the sensor. Avidin was compared with DENV II E protein due to its similar molecular weight around 50 – 65 kDa [15], [94]. At 1.0 nM, the identical procedures were carried out using avidin. The same figure's blue line indicates that there was no discernible change in the pre- and post-antibody-immobilization spectra. This outcome, in which no further layers were generated, and no shift was detected, was anticipated since avidin has no affinity for the immobilized IgG on the SMTF.

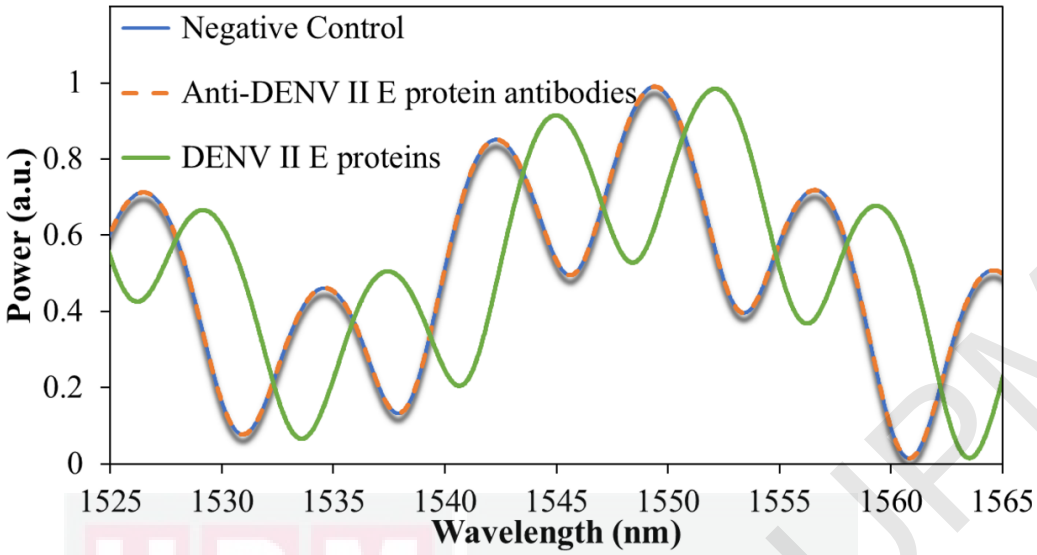

Figure 4.18: Output spectra prior to and subsequent to the introduction of DENV II E proteins, with avidin acting as the negative control.

3 sets of experiments were performed using cascaded SMTFs, referring to Table 4.2, and each one was exposed to a different concentration of DENV II E proteins ranging from 0.2 nM to 1.0 nM. After 15 minutes, the SMTF was rinsed three times with deionized water to remove any remaining molecules before drying. Each set of experiments was performed in triplicates to ensure the precision and accuracy of the sensor.

Table 4.2: 3 sets of different experiment for the detection of DENV II E protein.

NO	DENV II E Protein (nM)					
	SET 1		SET 2		SET 3	
	SMTF1	SMTF2	SMTF1	SMTF2	SMTF1	SMTF2
1	0.0	0.0	0.0	0.0	0.0	0.0
2	0.0	0.2	0.2	0.0	0.2	0.2
3	0.0	0.4	0.4	0.0	0.4	0.4
4	0.0	0.6	0.6	0.0	0.6	0.6
5	0.0	0.8	0.8	0.0	0.8	0.8
6	0.0	1.0	1.0	0.0	1.0	1.0

Figure 4.19 shows output spectra and a coherent trend line between the variable of DENV II E protein concentrations, and the corresponding wavelength shift that was observed based on the spectra response in Figure 4.20. For both experiments in set 1 and set 2, it yields a coefficient correlation value of 0.9997 and 0.9987 for SMTF2 and SMTF1. When both SMTFs increase gradually in experiment set 3, R^2 for both is above 0.9985. The R^2 for all spectral shift responses are also remarkably high, indicating that the linear fit is a good representation of the data. This demonstrates a clear relationship between concentration and red shifts as higher concentrations lead to a shifting of peaks towards longer wavelengths. The observed phenomenon is consistent with equation. 2.1 and 2.2, as the increase in concentration is directly proportional to the increase in RI, leading to the observed outcome. The sensitivity of the sensor for all sets of experiments obtained at a value of ≈ 6.9 nm/nM with SD of $\pm$ 0.87 for SMTF1 meanwhile sensitivity for SMTF2 obtained a value of ≈ 9.1 nm/nM with an SD of $\pm$ 1.08. SMTF2 has more sensitivity than SMTF1 (c). The larger

evanescent field at the sensor surface for SMTF2 is consistent with its smaller WD [77]. Therefore, this indicates that the sensor has excellent and linear sensitivity to the sample concentration. This allows for precise and accurate measurements of the sample concentration to be taken using the sensor.

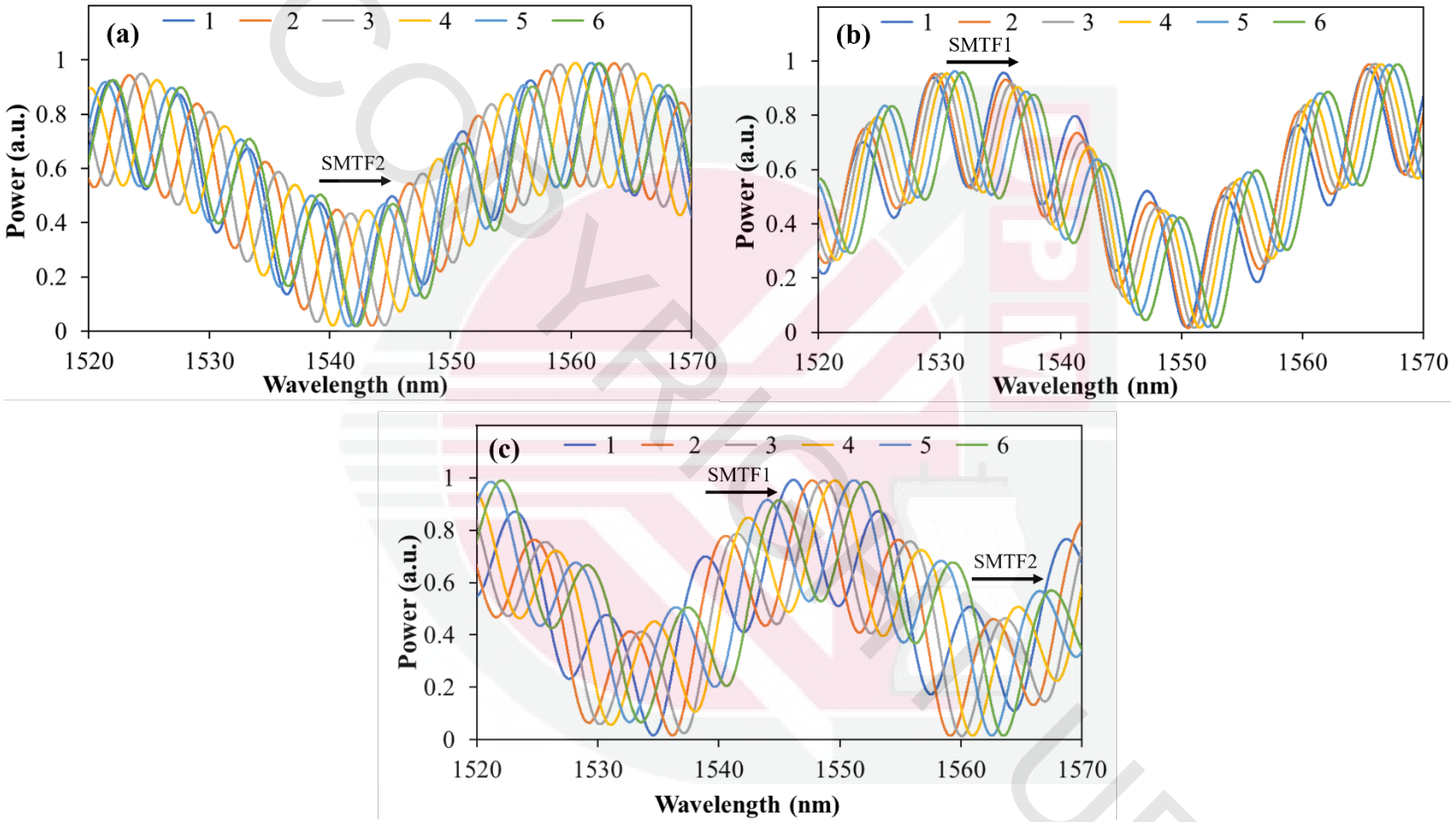

Figure 4.19: Output spectra for detection of a single disease using DENV II E Protein for the experiment in (a) set 1, (b) set 2, and (c) set 3.

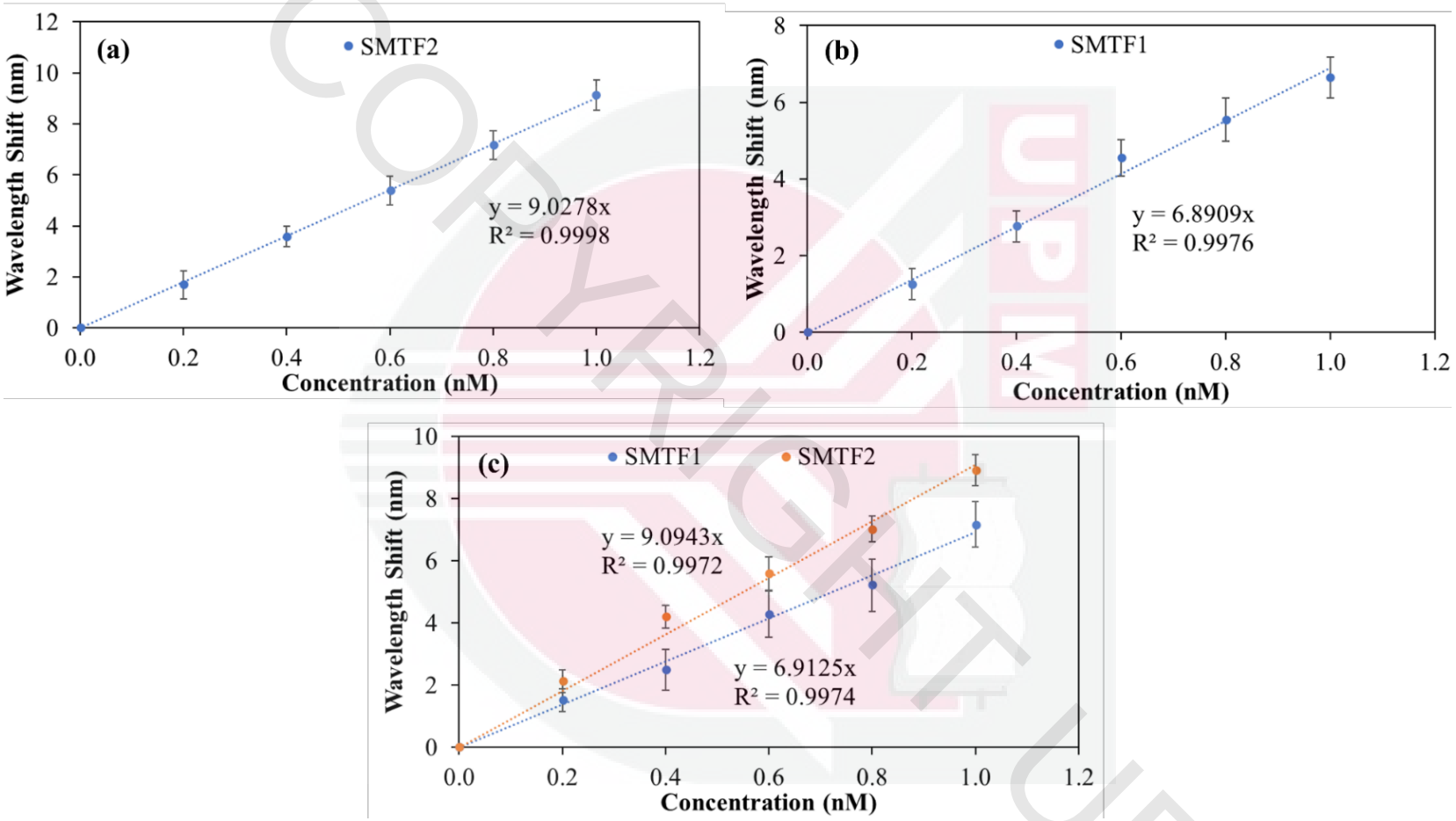

Figure 4.20: The trend line depicts the association between the shift and concentration of DENV II E proteins for the experiment in (a) set 1, (b) set 2, and (c) set 3.

The bio-functionalized SMTF was assessed for the presence of DENV II E proteins using Raman spectroscopy. The results were evaluated both before and after the DENV II E proteins were added to the fiber as depicted in Figure 4.21. There was a marked increase in the intensity of the signal at 490 cm^{-1} following the addition of DENV II E proteins. The increase, shown by the band S-S, indicates that there was a massive influx of protein molecules onto the surface. In the same vein, the presence of amides is indicated by another peak at 610 cm^{-1} [95]. Additionally, a notable increase at 835 cm^{-1} was detected, which was subsequently linked to C-C bonds [93]. Conversely, a decrease in intensity at 1303 cm^{-1} was observed, indicating a weakening of N-H bonds. In the conventional model of the antibody-antigen interaction, a C-N bond is formed when the COO^- of the antigen combines with the NH_3^+ of the antibody molecule [96].

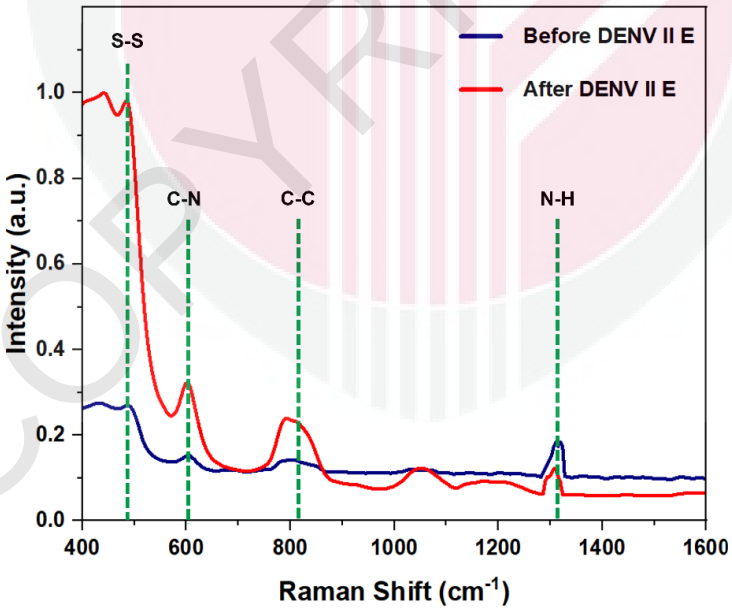

Figure 4.21: Raman spectrum of SMTF following DENV II E protein introduction.

To validate the binding between the antibody and the antigen, subsequent analyses utilizing energy-dispersive X-ray (EDX) spectroscopy, atomic force microscopy (AFM), and FESEM were conducted after the DENV II E protein was introduced. These techniques assessed the conformation, roughness, and thickness of each layer on the SMTF. These investigations complement the morphologies using FESEM to gain a quantitative evaluation of antibody-antigen binding structure. In Figure 4.22 (a), an increase of thickness from 11.680 nm to 18.366 nm was expected compared to Figure 4.23 (a). The roughness of the surface was also reflected in the Root Mean Square (RMS) values, which showed a similar pattern. With antibodies, the RMS value is 5.951, and DENV II E with RMS value of 10.421. The roughness value is a crucial factor in explaining the changes in light propagation that result in a strong optical response. Increased surface roughness leads to a greater surface area, resulting in a higher amount of adsorption of DENV II E protein. A 0.5 μm expected observation of thickness increment was observed in Figure 4.22 (b) and Figure 4.23 (b). The state is almost the same before and after the addition of the DENV II E protein, although both exhibit protein immobilization. This is because both the antibody and the antigen are proteins, and the presence of globular-like structures on the SMTF indicates that the protein has been functionalized and immobilized successfully shown in Figure 4.24.

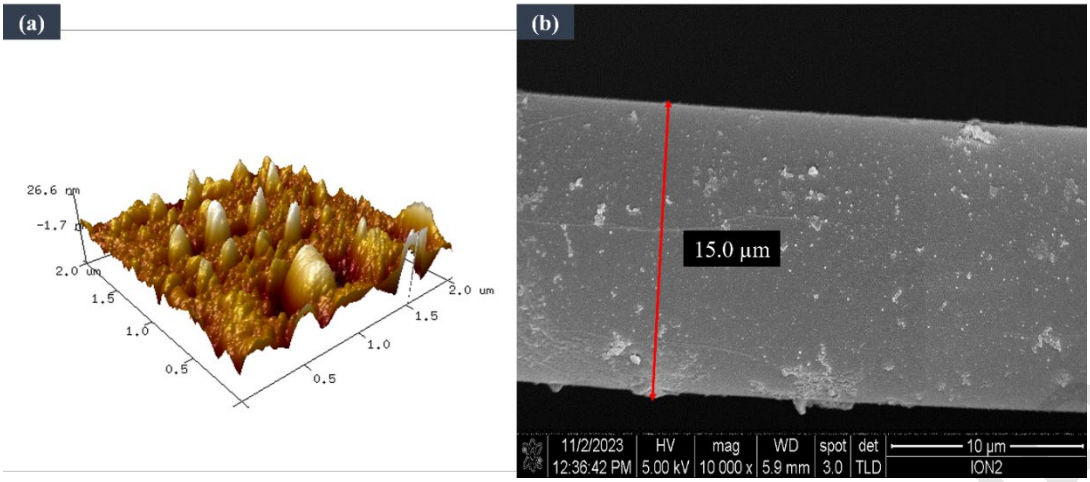

Figure 4.22: Anti-DENV II E protein immobilization for (a) AFM and (b) FESEM at 5kV under magnification of 10 K.

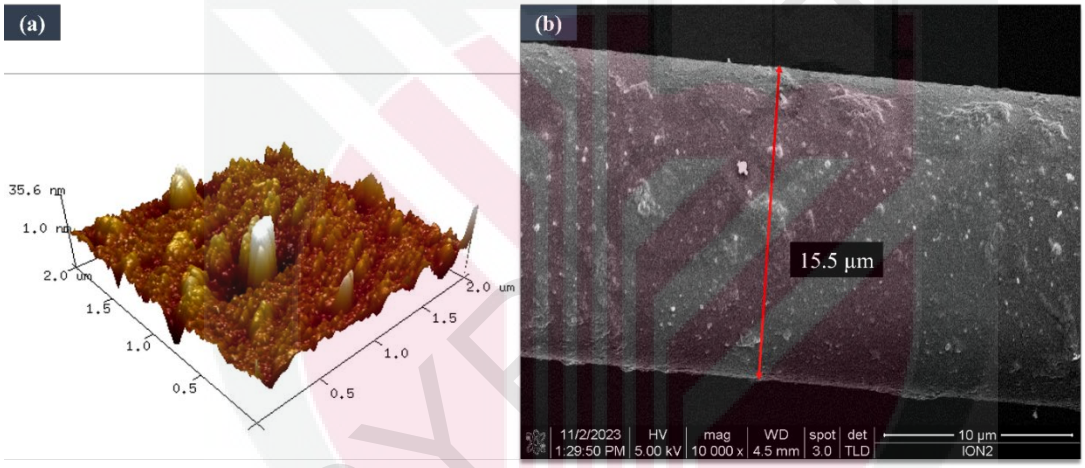

Figure 4.23: Introduction of DENV II E protein immobilization for (a) AFM and (b) FESEM at 5kV under magnification of 10 K.

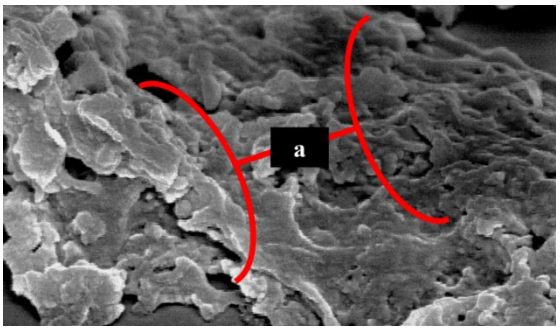

Figure 4.24: After the addition of DENV II E proteins, SMTF was observed using a FESEM at 5 kV and 50 K magnification. On the surface of the SMTF, globular-like structures are obvious throughout the area "a".

When comparing data from pre-and post-introduction of DENV II E protein, the EDX tests were more conclusive. Figure 4.25 shows a 5.22% increase and a 7.60% decrease in the number of Carbon and Oxygen molecules. This demonstrates how the antigen-antibody complex reacts and how the DENV II E protein adheres to the SMTF surface [54].

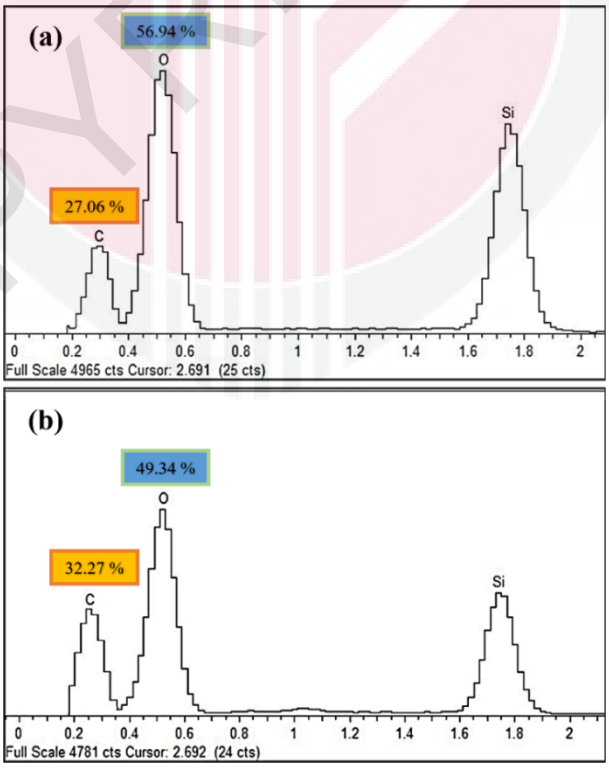

Figure 4.25: EDX spectra for before (a) and after (b) the introduction of DENV II E protein.

4.6 Detection of Dual-Diseases (DENV II E Protein and SARS-CoV-2 S Protein)

To accomplish the dual disease detection using DENV II E and SARS-CoV-2 proteins, the cascaded SMTFs will be immobilized with protein-specific antibodies that act as biorecognition molecules. Similar to the preliminary study, functionalization and immobilization are conducted. Cascaded sensor selectivity is determined by antibody immobilization on SMTF. The antibodies used should be those that bind specifically to the determinant of interest, which in this case is DENV II E and SARS-CoV-2 since there is growing interest in the potential interactions between these two infectious diseases, which includes the co-infection scenarios and antibody cross-reactivity.

For this subchapter, to decide which disease should be immobilized in which SMTFs, there were three critical benchmarks needed using the concept in the field of medicine: severity, infectivity period, and threshold concentration [74]. The severity of an illness or disease is measured by how much the body's systems break down or organs stop working. This shows how it can impact a person's health and quality of life, even to the point where it becomes life-threatening [97]. Meanwhile, the infectivity period is the amount of time that a person can spread an illness or microorganism to other people. Threshold concentration, on the other hand, is the amount of the substance that causes an adverse effect. The lower the threshold concentration, the more dangerous it would be. Table 4.3 shows the comparison of these 3 benchmarks to decide which disease is more critical. SARS-CoV-2 has a severity worse than DENV II E. It also has a higher infectivity period and lower threshold concentration, making this disease a crucial one to detect promptly. From the previous subchapter in this study, SMTF2 has higher sensitivity than SMTF1. Therefore, SMTF2 was chosen to immobilize the SARS-CoV-2 S protein, and SMTF1 is denoted for DENV II E Protein.

Table 4.3: Critical benchmark between SARS-CoV-2 and DENV II E disease.

No.	Critical Benchmark	SARS-CoV-2 vs. DENV II E	Ref
1	Severity	SARS-CoV-2 causes respiratory compilations, leads to life-threatening and has a broader global impact	[98]
2	Infectivity Period	SARS-CoV-2 ↑ than DENV II E, and easy to transmit	[99]
3	Threshold Concentration	SARS-CoV-2 ↓ than DENV II E, it takes fewer SARS-CoV-2 virus particles to infect someone than DENV II E does SARS-CoV-2 = 5.9pM/L, DENV II E = 100pM/L	[72]

In Figure 4.26, the reaction resulted in the immobilization of both antibodies on the SMTF, allowing them to function as intended while maintaining their selectivity for both antigens. Anti-DENV II E protein IgG antibody was immobilized in SMTF1, and SARS-CoV-2 S Protein S1 IgG antibody denoted to SMTF2. All steps for immobilization of antibodies were repeated as in the single disease detection. For the dilution, 0.1 μM SARS-CoV-2 S Protein S1 IgG antibody was prepared in 20 mM Tris with 50mM glycine, pH 7.6 with the same immersion time of DENV II E IgG Antibody of 30 minutes [54]. After 30 minutes, both SMTFs were rinsed three times to eliminate unbound molecules and left to dry at room temperature.

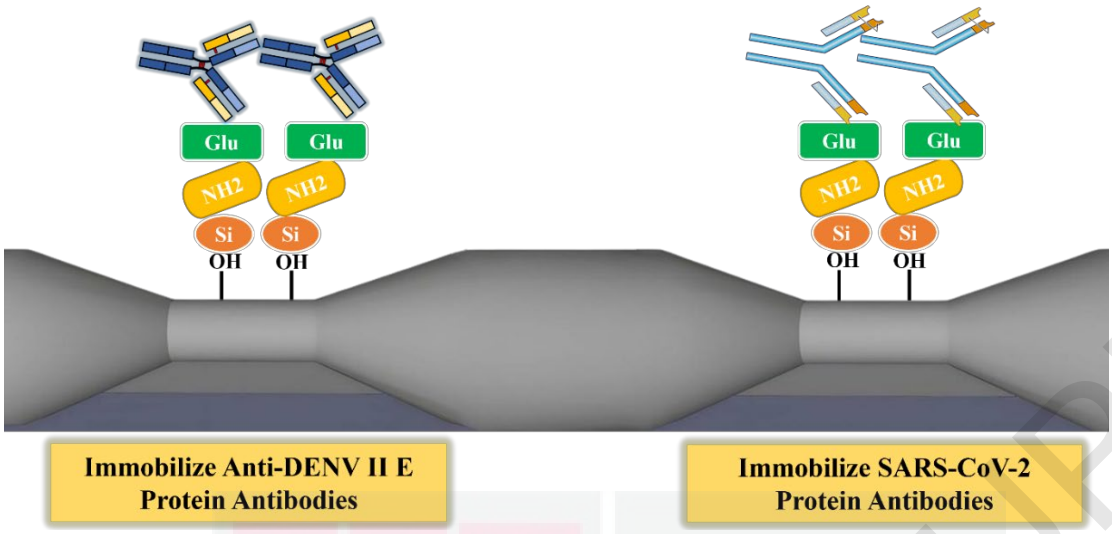

Figure 4.26: Antibodies immobilization for dual-disease detection.

A Raman spectroscopy analysis of the fully dried immobilized SMTF demonstrated the presence of SARS-CoV-2 S protein IgG antibodies on the fiber. According to the literature, the Raman spectra in Figure 4.27 aligned with an IgG molecule. The peak at 839 cm^{-1} was due to the tyrosine residues contained within the amino acid sequence of IgG, whereas area marked 'a', 1056 cm^{-1}, 1125 cm^{-1}, was originate from C-N, C-C, N-H protein stretching and terminal amino groups [100]. Protein structure or interactions with physiologically produced molecules may involve aromatic amino acids, such as tryptophan and phenylalanine, which are distinct signals of SARS-CoV-2 S protein. In general, an environment that contains aromatic amino acids is associated with strong signals in these regions [57], [101]. In addition, amide bonds indicative of the carboxylic end of the IgG molecule were detected. Raman peaks at 1288 cm^{-1} and 1404 cm^{-1} (Amide III) were identified. Peaks at 1542 cm^{-1} were attributed to the stretching of the C-N and N-H bends (Amide II), while the C=O vibrational mode was identified at 1674 cm^{-1} (Amide I). Meanwhile, Raman peaks at 2895 cm^{-1}, and 2930 cm^{-1} were attributed to stretching modes of C-H and $C-H_3$ groups of S proteins [102].

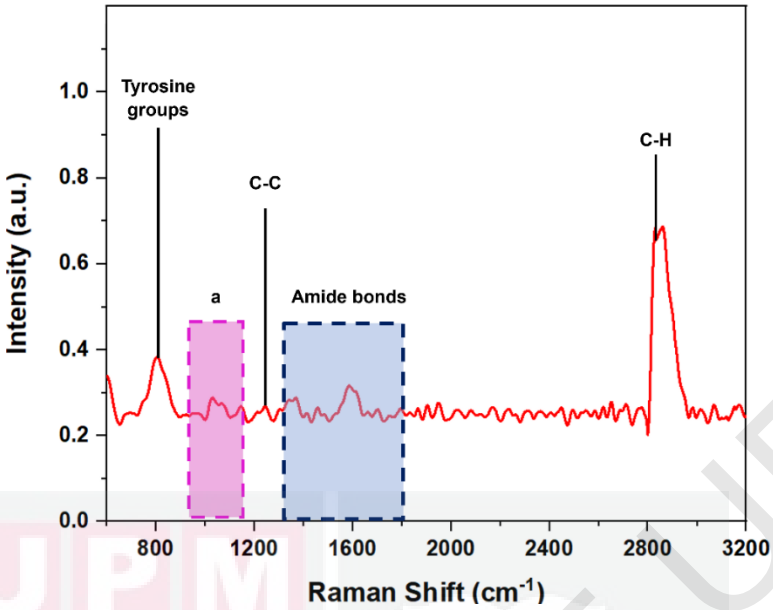

Figure 4.27: Raman spectra of a SMTF after anti-SARS-CoV-2 S-RBD IgG antibodies immobilization.

Each surface functionalization stage causes a red shift in Figure 4.28. When SMTF was introduced with APTES following NaOH hydroxylation, SMTF1 and SMTF2 spectrums shifted 1.24 nm and 2.05 nm to the right from the initial peak. Adding glutaraldehyde to the tapering optical fiber red shift both SMTFs by 0.89 nm and 1.36 nm, while immobilizing both protein IgG antibodies pushed the peak 2.71 nm and 3.13 nm farther. The wavelength shift correlated with molecule adhesion on the tapered surface, increasing the cladding RI and decreasing the Δn_{eff} value. According to equation. 2.1 and 2.2 in Chapter 2, reducing Δn_{eff} influences the spectrum's phase shift, resulting in a red shift when comparing spectra. The red shift observed in both SMTFs can be attributed to variations in RI in the vicinity of a SMTF, as previously explained.

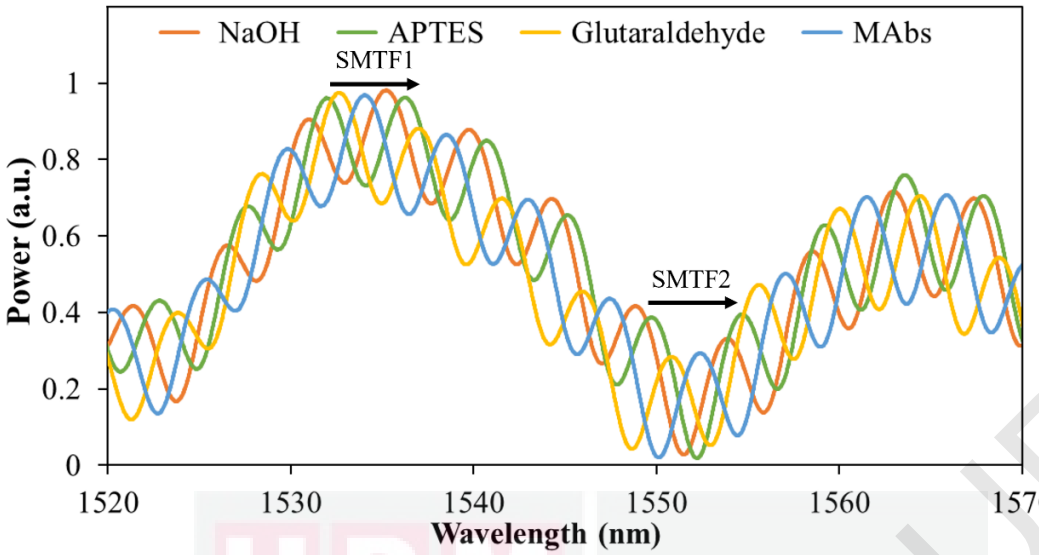

Figure 4.28: Output spectra after surface functionalization and antibodies immobilization.

An immobilized surface for SMTF1 and SMTF2 was used to introduce the DENV II E and SARS-CoV-2 proteins. The sensor's ability to selectively detect S and E proteins was the driving force for immobilizing the two protein antibodies onto a SMTF surface. As demonstrated in Figure 4.29, this can be achieved where SMTF1 attaches to DENV II E and SMTF2 with SARS-CoV-2 proteins due to their unique affinity.

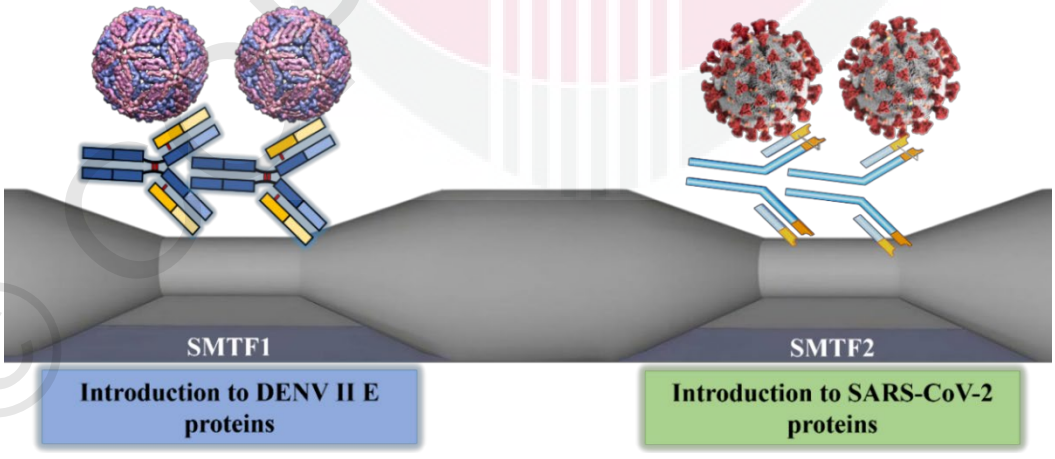

Figure 4.29: Dual-disease detection occurs in cascaded SMTFs.

To begin dual-disease detection, 1 nM concentrations of DENV II E protein (SMTF1) and SARS-CoV-2 protein (SMTF2) were used. The dilution for DENV II E was prepared in the same manner as before. However, for SARS-CoV-2 protein incubation, Phosphate Buffer Saline at pH 7.0 (EastCoast Bio) was used. During the optimization process, a fresh batch of functionalized SMTF was utilized. After 15 minutes, the excess solution was carefully washed out and the tapered region was rinsed three times with deionized water to ensure the removal of any remaining molecules and left to dry at room temperature. The resulting spectra were read using OSA. Figure 4.30 depicts a red shift of 1.47 nm for SMTF1 and 2.84 nm for SMTF2 in spectra pre-and post-introduction of DENV II E proteins.

The phenomenon of red shift can be attributed to alterations in the RI of the external environment surrounding tapered region. The sensor configuration was assessed using MERS-CoV as a negative control to mitigate any biases and assess the specificity of the sensor. MERS-CoV was compared to DENV II E and SARS-CoV-2 proteins since all three of these viruses belong to the order Nidovirales [65]. A variety of proteins, including non-structural proteins (NSPs) involved in transcription and viral replication, are encoded in the RNA genome of every virus. Additionally, it comprises structural proteins that constitute the virion, the viral particle released by infected cells. The three viruses have NSPs that are remarkably similar to each other, but the structural proteins have some differences [73]. It has been hypothesized that these variations account for the diverse infectivity and pathogenicity of the viruses.

The same procedures were followed for MERS-CoV at 1.0 nM. The same steps were repeated for MERS-CoV at 1.0 nM. As seen by the blue line in the same figure, there was a slight blue shift between the spectra before and after the antibody was immobilized. This can be explained by the non-specific adsorption phenomenon. The protein could be adsorbed non-specifically to the surface of the SMTF [103]. This may occur if the protein and the fiber surface have hydrophobic or electrostatic interactions. Even minimal non-specific adsorption can cause a slight change in the RI of the fiber, resulting in a blue shift in wavelength. The local environment surrounding the SMTF may be changing because of the protein's presence [104]. For instance, the protein might be drawing in ions or water molecules, which would alter the fiber's RI. This also led to blue shift in wavelength. This demonstrates that the sensor is specific for the SARS-CoV-2 and DENV II E protein (SMTF1), respectively.

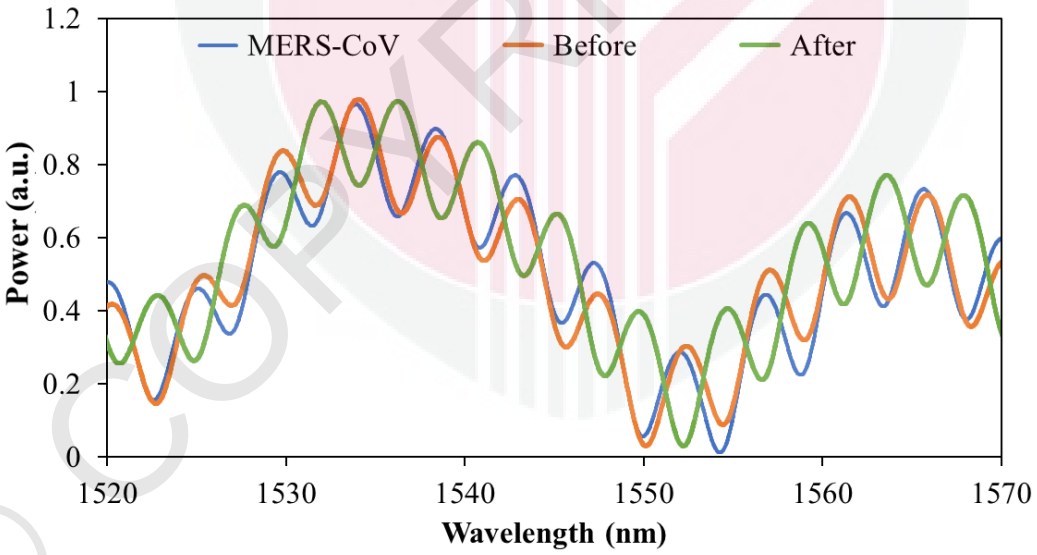

Figure 4.30: Output spectra prior to and subsequent to the introduction of the SARS-CoV-2 and DENV II E proteins, with MERS-CoV-2 as negative control.

Table 4.4 shows set of cascaded SMTF tests with DENV II E protein (SMTF1), and SARS-CoV-2 S protein (SMTF2) at concentrations from 0.2 nM to 1.0 nM. Before drying, the SMTF was rinsed three times with deionized water to eliminate residual molecules after 15 minutes. Triplicate experiments were done to confirm sensor precision and accuracy.

Table 4.4: 3 sets of different experiments for dual-disease detection of DENV II E protein and SARS-CoV-2 S protein.

NO	SET 1		SET 2		SET 3	
	SMTF1	SMTF2	SMTF1	SMTF2	SMTF1	SMTF2
	DENV II E (nM)	SARS-CoV-2 (nM)	DENV II E (nM)	SARS-CoV-2 (nM)	DENV II E (nM)	SARS-CoV-2 (nM)
1	0.0	0.0	0.0	0.0	0.0	0.0
2	0.0	0.2	0.2	0.0	0.2	0.2
3	0.0	0.4	0.4	0.0	0.4	0.4
4	0.0	0.6	0.6	0.0	0.6	0.6
5	0.0	0.8	0.8	0.0	0.8	0.8
6	0.0	1.0	1.0	0.0	1.0	1.0

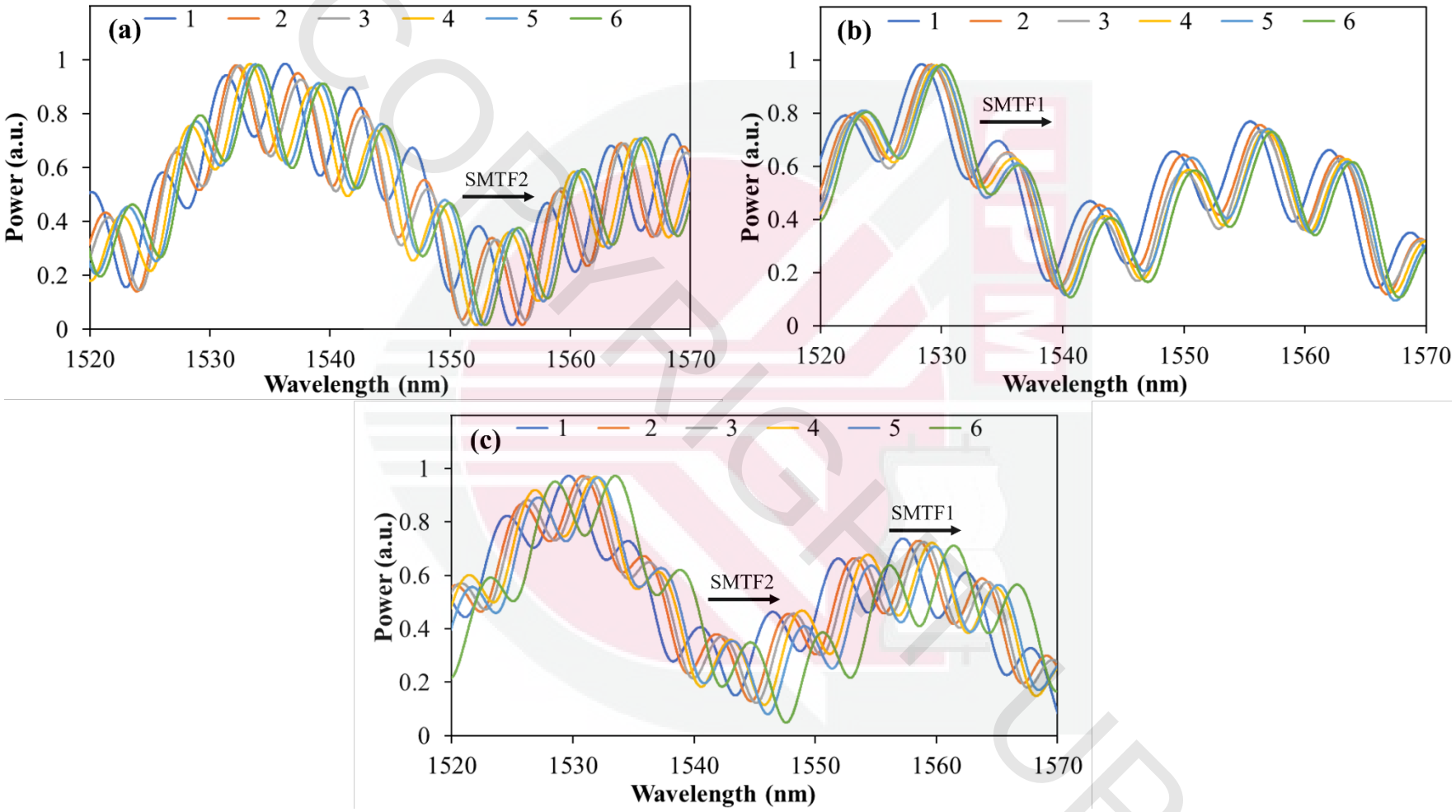

Figure 4.31: Output spectra for detection of dual disease for the experiment in (a) set 1, (b) set 2, and (c) set 3.

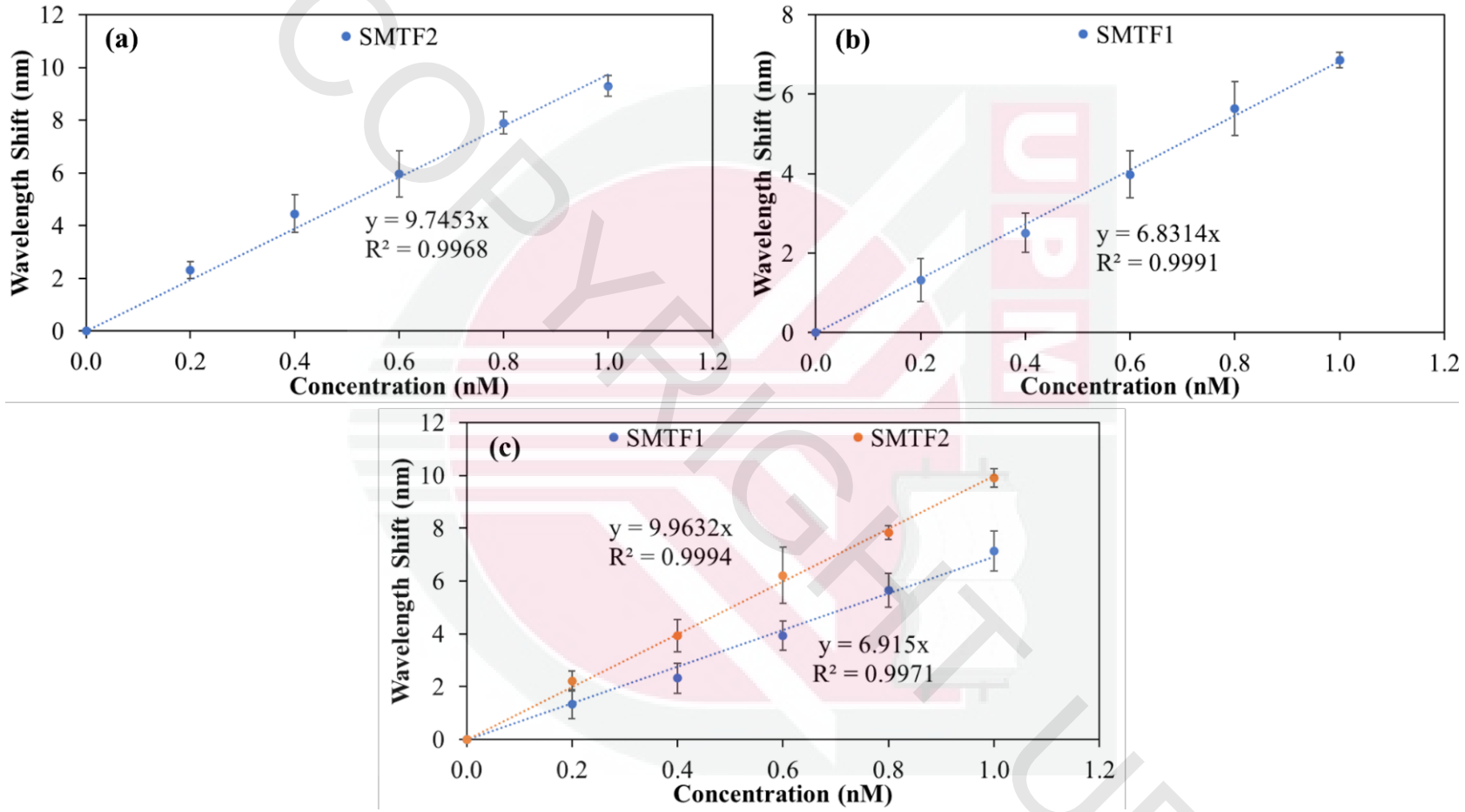

Figure 4.32: The trend line illustrates the correlation between the shift and concentration of dual disease in 3 sets of experiments: (a) set 1, (b) set 2, and (c) set 3.

Figure 4.31 displays output spectra and coherent trend line between dual disease concentrations and wavelength shifts based on spectra response in Figure 4.32. Both experiments in set 1 and set 2 provide coefficient correlation values of 0.9968 and 0.9991 for SMTF2 and SMTF1. When both SMTFs increase gradually in experiment set 3, R^2 for both is above 0.9970. The linear fit accurately represents the data, as indicated by high R^2 values for all spectral shift responses. This shows a strong relationship between concentration and red shifts, as increasing concentrations cause peaks to shift towards longer wavelengths. The observed phenomenon is consistent with equation. 2.1 and 2.2, because an increase in concentration is directly proportional to an increase in RI, resulting in the observed result. The sensitivity of the sensor for all sets of experiments obtained at a value of ≈ 6.9 nm/nM with SD of $\pm$ 0.72 for SMTF1 meanwhile sensitivity for SMTF2 obtained a value of ≈ 10 nm/nM with SD of $\pm$ 0.56. SMTF2 has more sensitivity than SMTF1. As a result, the sensor exhibits good and linear sensitivity to sample concentration. This enables the sensor to take precise and accurate readings of sample concentration.

Raman spectroscopy was used to characterize the surface of the SMTF following the introduction of the SARS-CoV-2 protein. Significant changes can be discerned by comparing the Raman spectra obtained prior to and after the introduction of the S protein from SARS-CoV-2, depicted in Figure 4.33. Observations are also noted to be similar with previous results in Figure 4.33 for introduction of DENV II E protein. The notable rise in intensity at the 490 cm^{-1} band peak can be attributed to the introduction of S-S bonds resulting from the binding of antigens onto the SMTF surface [96]. The occurrence of the same phenomena increased C-C and C-C-H bonds, leading to the formation of a peak at 605 cm^{-1} [101]. Diminishment in intensity was seen at peaks

810 cm^{-1}, 1035 cm^{-1}, 1210 cm^{-1}, 1340 cm^{-1}, and 1442 cm^{-1}, indicating a decrease in amino functional groups and N-H bonds [102]. The result that was observed aligns with the anticipated outcome of an immune response, wherein the amine functional group undergoes hydrolysis upon the interaction of an antigenic determinant and its corresponding antibody.

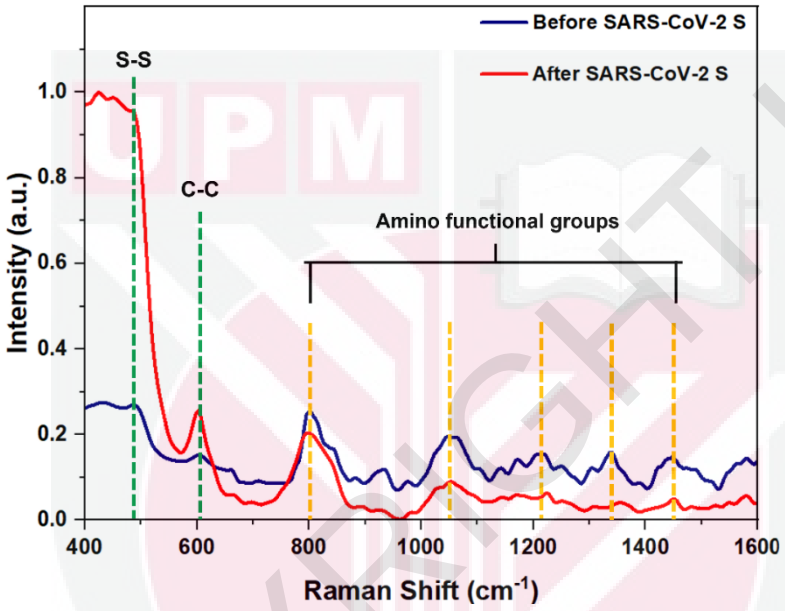

Figure 4.33: Raman spectrum of SMTF after introduction of SARS-CoV-2 S protein.

After introducing the SARS-CoV-2 S protein for SMTF2, AFM, FESEM, and EDX were used to further characterize the SMTF. Validation of antibody-antigen binding was done, and the thickness, roughness, and conformation of each layer were evaluated. When compared to Figure 4.34 (a), an increase in thickness from 13.446 nm to 19.466 nm was predicted in Figure 4.35 (a). The RMS value for antibody is 6.149, whereas the RMS value for antigen is 10.093. Surface roughness is known to influence molecule adhesion to a surface. This effect increases the surface area available for molecule adsorption. Furthermore, it encourages interactions to take

place in close proximity, resulting in greater bonds and better adhesive strength which is identical before and after its addition depicted in Figure 4.34 (b) and Figure 4.35 (b). These antibodies interact with other molecules in a stable and specific manner due to their globular shape. A 0.5 µm increase in the thickness of the SMTF was observed. Since both the antigen and the antibody are proteins, the SMTF exhibits globular-like structures. This means that the protein has been functionalized and immobilized properly since anti-SARS-Cov-2 S receptor-binding domain (RBD) IgG Antibodies were used, as shown in Figure 4.36.

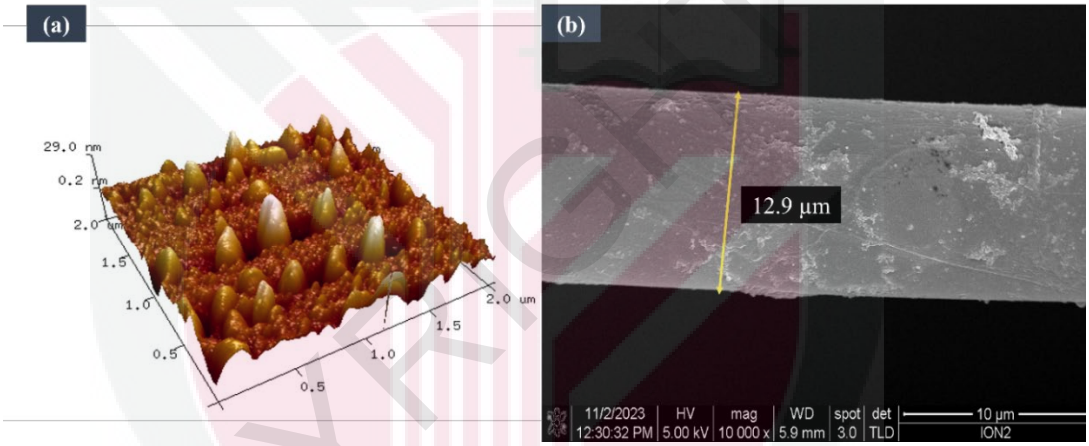

Figure 4.34: Anti-SARS-CoV-2 S protein immobilization for (a) AFM and (b) FESEM at 5kV under magnification of 10 K.

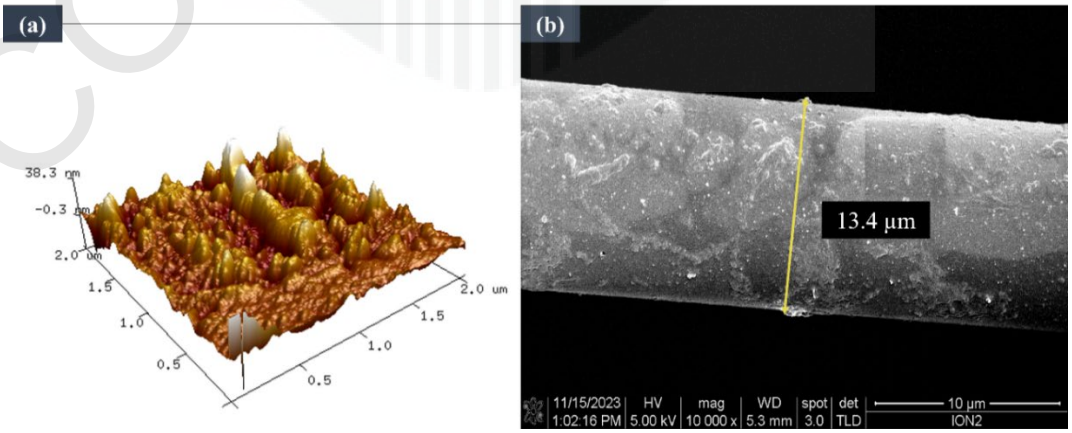

Figure 4.35: Introduction of SARS-CoV-2 S protein immobilization for (a) AFM and (b) FESEM at 5kV under magnification of 10 K.

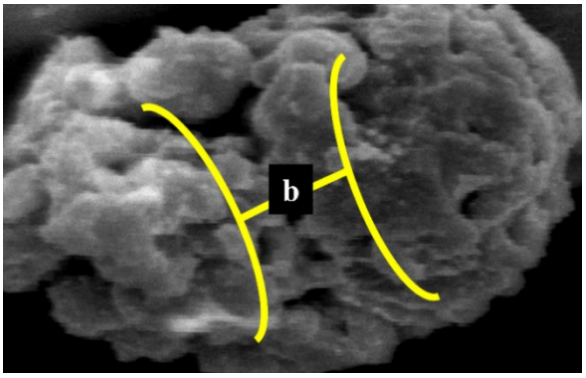

Figure 4.36: FESEM image of SMTF after adding SARS-CoV-2 S proteins at 5 kV and 50 K magnification. Throughout area "b," there are apparent globular-like structures on the SMTF 's surface.

The results were more definitive when comparing EDX analyses conducted before and after the SARS-CoV-2 S protein was introduced. Figure 4.37 shows that the number of carbon and oxygen molecules increased by 3.20% and decreased by 5.69%, respectively. This aids antigen-antibody complex formation and SARS-CoV-2 S protein binding to the tapered region.

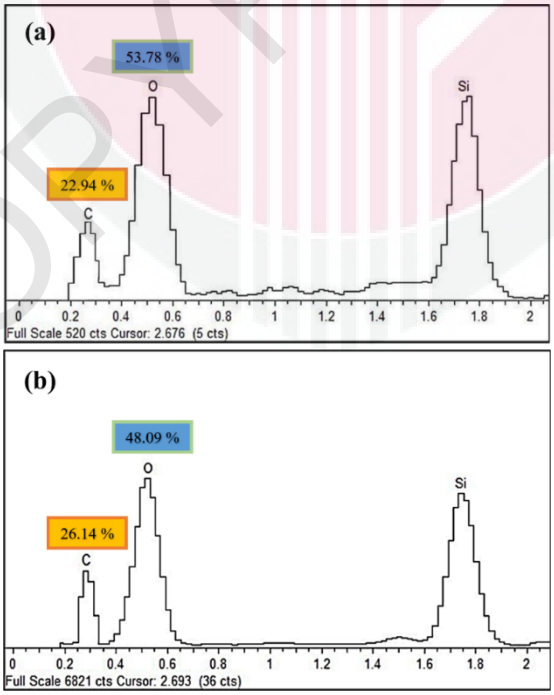

Figure 4.37: EDX spectra for before (a) and after (b) the introduction of SARS-CoV-2 S protein.

For LOD determination using cascaded SMTFs, concentrations of DENV II E protein (SMTF1) and SARS-CoV-2 S protein (SMTF2) within the range of 0.01 pM to 10 nM were tested. Focused on this experiment offers a valuable starting point to establish a comparable baseline and simplify initial analysis. And therefore, an equal increase in concentration was done for both DENV II E and SARS-CoV-2 proteins. To determine the sensor's affinity for these proteins, the experiment was repeated three times, and the data was analyzed using the Langmuir adsorption isotherm equation. From Figure 4.38, the lowest possible concentration detected by the sensor was 0.1 pM as no wavelength shift was observed with concentrations lower than 0.1 pM for both SMTFs. The LOD value obtained was even better than the previous study, using a single SMTF to detect DENV II E protein which obtained only 1 pM [54]. In another study, the development of a gold nano-film deposited on a D-shaped plastic optical fiber was also able to detect SARS-CoV-2 S proteins, however, with a detection limit of only 37 nM [105]. The dissociation constant, K_d obtained is 1.42×10^{-10} M (SMTF1) and 1.15×10^{-10} M for (SMTF2) with R^2 above 0.9980 and SD below 10 for both SMTFs, which confirms the higher affinity of the sensor and was comparable to previously reported literature [106]. Future investigations should explore in unequal concentration changes to gain a more comprehensive understanding of the sensor's performance to mimic real-world scenarios where the concentrations of the target proteins might differ significantly. This will allow for a more thorough assessment of the sensor's ability to detect both proteins and map the dynamic range of the cascaded SMTF sensor.

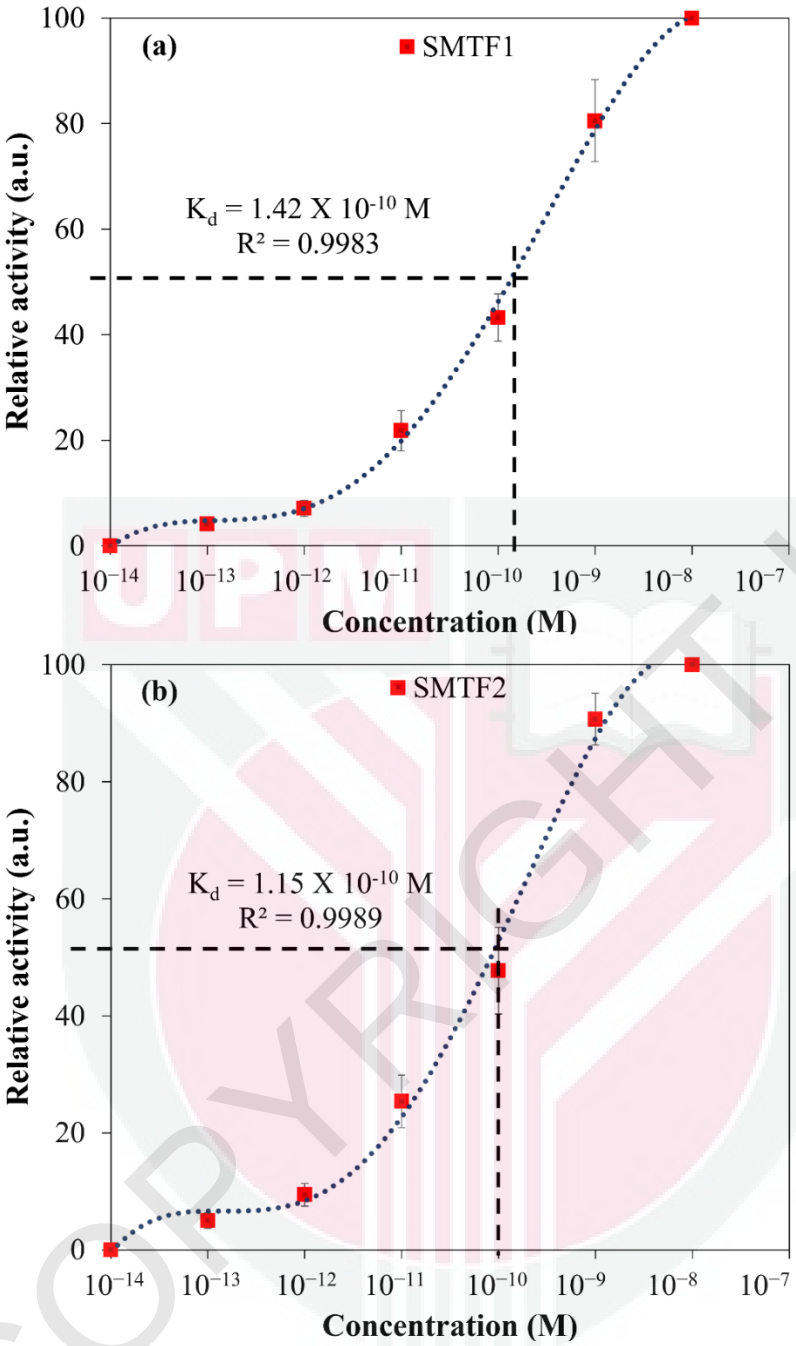

Figure 4.38: The wavelength shift corresponding to different concentrations of (a) DENV II E (SMTF1) and (b) SARS-CoV-2 S (SMTF2) proteins, ranging from 0.01 pM to 10.0 nM, was fitted using the Langmuir isotherm adsorption equation.

4.7 Summary

Surface functionalization, optimization, and biofunctionalized cascaded SMTFs sensor characterization were elaborated in this chapter. Immobilizing anti-DENV II E protein antibodies on a SMTF surface improves the sensor's selectivity. The cascaded SMTF sensor was then tested using dual-disease detection. In this case, DENV II E protein (SMTF1) and SARS-CoV-2 S protein (SMTF2) were used. The sensor's selectivity for DENV II E protein and SARS-CoV-2 S protein has been enhanced by immobilizing the two protein antibodies on the tapered region. The sensor achieved a sensitivity of approximately 6.9 nm/nM (SMTF1) and approximately 10 nm/nM (SMTF2). The sensor configuration achieved a LOD value of 0.1 pM with a dissociation constant (K_d) of 1.42×10^{-10} M for SMTF1 and 1.15×10^{-10} M SMTF2.

CHAPTER 5

CONCLUSIONS, RESEARCH CONTRIBUTIONS, LIMITATIONS AND FUTURE WORKS RECOMMENDATION

5.1 Conclusions

The focus of this research work is to develop a cascaded SMTF biosensor for simultaneous detection of dengue and SARS-CoV-2 viruses. The research began with the design and fabrication of cascaded SMTFs with optimized parameters. The results led to the selection of two taper profiles: SMTF1 (12 μm of WD, 5 mm of WL) and SMTF2 (10 μm of WD, 20 mm of WL) which fulfilled the first objective. Both up and down taper lengths were fixed at 5 mm. The FSR difference of 23.233 nm and 3.880 nm created a composite spectrum with small fringes superimposed over large fringes.

With the optimized cascaded SMTFs, the work progressed into completing its second objective, which was to investigate the performance of simultaneous detection using two different RIs. The cascaded SMTF was analyzed using 4 sets of experiments with varied RI solution sequences that were manipulated by exposing the SMTF surface to various concentrations of bulk NaCl solution ranging from 0.2 M to 1.0 M. The results indicated that RIs may be concurrently identified by analyzing the transmission output spectrum for the wavelength shift of both small and large fringes. This finding holds significant potential for developing sensors capable of detecting multiple analytes at different concentrations, concurrently.

The work continued with the investigation of cascaded SMTF spectral response towards the presence of different biological analytes. Initial tests on the SMTF for

selective sensing with functionalized bio-recognition molecules were conducted. Due to their strong affinity, biotin-avidin was used for the study. Following biotin immobilization on the tapered surface, the bio-functionalized cascaded SMTFs were tested in 3 sets of experiments with varying concentrations of avidin ranging from 0.2 μM to 1.0 μM in each SMTF. A consistent wavelength shift was achieved for all sets using the bio-functionalized SMTF. In experiment set 3, increasing avidin concentration for both tapers yielded sensitivity values of 6.36 nm/μM (SMTF1) and 9.26 nm/μM (SMTF2), with SD of $\pm$ 1.78 and R^2 value of 0.99. With proper functionalization, cascaded SMTFs can preferentially detect the required determinant. The larger WD of SMTF1 explains why it is less sensitive than SMTF2. Since its penetration depth is less due to its greater width, the evanescent field interacts less with target protein molecules at the sensor surface. Thus, SMTF1 has a weaker response and lower sensitivity than SMTF2.

The functionalization process for the cascaded SMTF biosensor, which utilizes DENV II E proteins for single disease detection, involved hydroxylating the cascaded SMTFs surface using NaOH. Following this, APTES silanization, glutaraldehyde activation, and immobilization of anti-DENV II E protein antibodies. 3 sets of experiments were performed with DENV II E protein with concentrations from 0.2 nM to 1.0 nM. Both sensor configurations for single disease detection using cascaded SMTF exhibited good sensitivity, with SMTF2 achieving slightly higher sensitivity (9.1 nm/nM) compared to SMTF1 (6.9 nm/nM). This difference is due to the smaller WD of SMTF2, which results in a larger evanescent field at the sensor surface, enhancing its interaction with the target protein molecules.

The work continued using the same procedure applied before for dual-disease detection, in this case, DENV II E proteins (SMTF1) and SARS-CoV-2 spike proteins (SMTF2). The sensor was able to achieve a sensitivity value of ≈ 6.9 nm/nM (SMTF1) and ≈ 10 nm/nM (SMTF2). Additionally, the LOD and affinity of the sensor for both proteins were determined via experiments involving determinant proteins within a concentration range of 10 nM to 0.01 pM. An LOD value was achieved by the sensor configuration of 0.1 pM and a dissociation constant, K_d of 1.42×10^{-10} M for SMTF1 and 1.15×10^{-10} M for SMTF2. Overall, the sensing performance demonstrates the success of fabricating and designing a cascaded SMTF biosensor for simultaneous detection of dengue and SARS-CoV-2 viruses.

5.2 Research Contribution

The world stands at a pivotal juncture, facing dangerous virus crisis that have gripped over half of its population. This escalating threat, potentially even fatal, underscores the urgent need for continuous advancement in simultaneous multiple disease diagnostics. More effective and targeted responses are required to avert this catastrophe and safeguard global health. Multiplexing is essential for biosensors, especially when trying to diagnose infections with identical symptoms. The major contribution of this research is the demonstration of a possible alternative dual sensor using the cascaded SMTF configuration with the potential for early diagnosis and improved patient outcomes. While the proposed work remains in the proof-of-concept stage, its application to both viruses using DENV and SARS-CoV-2 has yielded promising results. Both viruses were used in this study since they share similar pathological behaviour. As a result, a quantitative, selective, and highly sensitive method is developed for the detection and monitoring of dual diseases. This could

potentially provide insights into the virus's characteristics and aid in enhancing clinical management of infection.

5.3 Limitations of Work

The work showed the potential of bio-functionalized cascaded SMTF as a sensor for multiple diseases utilizing DENV II E and SARS-CoV-2 S protein, however, it had limitations. When analyzing multiple diseases simultaneously, spectrum changes may overlap, making it hard to distinguish at a certain concentration range, complicating the process of analysis. The overlap of spectral responses makes it difficult to distinguish the large and small fringes of each disease. This uncertainty can cause misinterpretations and erroneous diagnosis, especially for illnesses with similar spectral signatures.

5.4 Future Work

The groundbreaking results of this research have opened a plethora of exciting avenues for further exploration. Here are just a few suggestions for future work that build upon this success:

- This research was only concerned with the identification of dual illness. DENV II E and SARS-CoV-2 S proteins were employed in this work. However, it is possible to investigate other prominent variants of these diseases. For example, employing several DENV strains (DENV-1, DENV-3, and DENV-4) and other SARS-CoV-2 variations (Alpha, Beta, Delta, and Omicron).
- Implementing the use of nanomaterials such as AuNPs, CNTs, Chitosan, and PAMAM Dendrimers to enhance the sensing capabilities of the sensor.
- Spectrum shifts associated with different diseases may overlap, making it challenging to differentiate between them. This can be overcome through advanced signal processing techniques or by selecting targets with distinct spectral signatures and improving disease identification accuracy by exploring the use of:
    i. Machine learning for spectral analysis
    ii. Decision-making trees and rule-based systems
    iii. Ensemble method of multiple algorithms
    iv. Artificial intelligence for spectra interpretation

REFERENCES

[1] M. Elsherif, A. E. Salih, M. G. Muñoz, F. Alam, B. AlQattan, D. S. Antonysamy, M. F Zaki, A. K. Yetisen, S. Park, T. D. Wilkinson, and H. Butt, "Optical Fiber Sensors: Working Principle, Applications, and Limitations," *Advanced Photonics Research*, vol. 3, no. 11, p. 2100371, Jul. 2022.

[2] R. Min, B. Ortega, and C. Marques, "Latest achievements in polymer optical fiber gratings: Fabrication and applications," *Photonics*, vol. 6, no. 2, p. 36, Mar. 2019.

[3] V. Bhardwaj, K. Kishor, and A. C. Sharma, "Tapered optical fiber geometries and sensing applications based on Mach-Zehnder Interferometer: A review," *Optical Fiber Technology*, vol. 58, p. 102302, Sep. 2020.

[4] D. J. J. Hu and A. H. P. Ho, "Plasmonic Photonic Crystal Fibers," *Progress in Optical Science and Photonics*, vol. 9, no. 1, pp. 1-12, Jul. 2020.

[5] S. E. J. Bell, G. Charron, E. Cortés, J, Kneipp, M. L. de a Chapelle, J. Langer, M. Procházka V. Tran, and S. Schlücker, "Towards Reliable and Quantitative Surface-Enhanced Raman Scattering (SERS): From Key Parameters to Good Analytical Practice," *Angewandte Chemie - International Edition*, vol. 59, no. 14, pp. 5454-5462, Mar. 2020.

[6] S. Korposh, S. W. James, S. W. Lee, and R. P. Tatam, "Tapered Optical Fibre Sensors: Current Trends and Future Perspectives," *Sensors (Basel, Switzerland)*, vol. 19, no. 10, pp. 2294, May, 2019.

[7] H. Gao, J. Wang, J. Shen, S. Zhang, D. Xu, Y. Zhang, and C. Li, "Study of the vernier effect based on the fabry–perot interferometer: Methodology and application," *Photonics*, vol. 8, no. 8, p. 304, Jul. 2021.

[8] A. B. Socorro-Leránoz, D. Santano, I. Del Villar, and I. R. Matias, "Trends in the design of wavelength-based optical fibre biosensors (2008–2018)," *Biosensors and Bioelectronics: X*, vol. 1, p. 100015, Jun. 2019.

[9] S. L. Lee, J. Kim, S. Choi, J. Han, G. Seo, and Y. W. Lee, "Fiber-optic label-free biosensor for SARS-CoV-2 spike protein detection using biofunctionalized long-period fiber grating," *Talanta*, vol. 235, p. 122801, Dec. 2021.

[10] N. De Acha, A. B. Socorro-Leránoz, C. Elosúa, and I. R. Matías, "Trends in the design of intensity-based optical fiber biosensors (2010–2020)," *Biosensors*, vol. 11, no. 6, p. 197, Jun. 2021.

[11] J. Xue, Y. Zhang, Z. Guang, T. Miao, Z. Ali, D. Qiao, Y. Yao, K. Wu, L. Zhou, C. Meng, and N. Copner, "Ultra-High Sensitivity Terahertz Microstructured Fiber Biosensor for Diabetes Mellitus and Coronary Heart Disease Marker Detection," *Sensors*, vol. 23, no. 4, p. 2020, Feb. 2023.

[12] F. Chiavaioli, C. A. J. Gouveia, P. A. S. Jorge, and F. Baldini, "Towards a uniform metrological assessment of grating-based optical fiber sensors: From refractometers to biosensors," *Biosensors*, vol. 7, no. 2, p .23, Jun. 2017.

[13] J. D. Love, W. M. Henry, W. J. Stewart, R. J. Black, S. Lacroix, and F. Gonthier, "Tapered single-mode fibres and devices. I. Adiabaticity criteria," *IEE Proceedings J (Optoelectronics)*, vol. 138, no. 5, pp. 343–354, Oct. 1991.

[14] X. Fu, D. Li, Y. Zhang, G. Fu, W. Jin, and W. Bi, "High sensitivity refractive index sensor based on cascaded core-offset splicing NCF-HCF-NCF structure," *Optical Fiber Technology*, vol. 68, p. 102791, Jan. 2022.

[15] M. D. L. Muñoz, G. Limón-Camacho, R. Tovar, A. Diaz-Badillo, G. Mendoza-Hernández, and W. C. Black, "Proteomic identification of dengue virus binding proteins in Aedes aegypti mosquitoes and Aedes albopictus cells," *BioMed research international*, vol. 2013, Jan. 2013.

[16] P. Velusamy, K. Kiruba, C. H. Su, V. Arun, P. Anbu, S. C. Gopinath, and B. Vaseeharan, "SARS-CoV-2 spike protein: Site-specific breakpoints for the development of COVID-19 vaccines," *Journal of King Saud University - Science*, vol. 33, no. 8, p. 101648, Dec. 2021.

[17] G. P. Agrawal, "Fiber-Optic Communication Systems (Fifth Edition)," *John Wiley & Sons*, Jun. 2021.

[18] P. Lu, N. Lalam, M. Badar, B. Liu, B. T. Chorpening, M. P. Buric, and P. R. Ohodnicki, "Distributed optical fiber sensing: Review and perspective," *Applied Physics Reviews*, vol. 6, no. 4, Dec. 2019.

[19] B. Lee, "Review of the present status of optical fiber sensors," *Optical Fiber Technology*, vol. 9, no. 2, pp. 57-79, Apr. 2003.

[20] J. Zhang, Y. Xiang, C. Wang, Y. Chen, S. C. Tjin, and L. Wei, "Recent Advances in Optical Fiber Enabled Radiation Sensors," *Sensors*, vol. 22, no. 3, p. 1126, Feb. 2022.

[21] E. E. Gdoutos, "Optical Fiber Strain Sensors," *Solid Mechanics and its Applications*, vol. 269, pp. 219-233, Jan. 2022.

[22] R. Correia, S. James, S. W. Lee, S. P. Morgan, and S. Korposh, "Biomedical application of optical fibre sensors," *Journal of Optics (United Kingdom)*, vol. 20, no. 7, p. 073003, Jul. 2018.

[23] F. Sequeira, D. Duarte, L. Bilro, A. Rudnitskaya, M. Pesavento, L. Zeni, and N. Cennamo, "Refractive index sensing with D-shaped plastic optical fibers for chemical and biochemical applications," *Sensors (Switzerland)*, vol. 16, no. 12, p. 2119, Dec. 2016.

[24] A. Urrutia, I. Del Villar, P. Zubiate, and C. R. Zamarreño, "A Comprehensive Review of Optical Fiber Refractometers: Toward a Standard Comparative Criterion," *Laser and Photonics Reviews*, vol. 13, no. 11, p. 1900094, Nov. 2019.

[25] R. Q. Lv, Q. Wang, B. T. Wang, Y. Liu, and L. Kong, "Polymer microfiber bridging Bi-tapered refractive index sensor based on evanescent field," *Optics Communications*, vol. 414, pp. 134-139, May. 2018.

[26] J. Liu, J. Dong, Y. Wang, H. Yuan, Q. Song. Y. Xue, J. Xu, P. Liu, D. Li, K, Lebbou and Z. Wang, "Laser operation of tm: LuAG single-crystal fiber grown by the micro-pulling down method," *Crystals (Basel)*, vol. 11, no. 8, p. 898, Jul. 2021.

[27] W. Jin and L. Hu, "Review on quasi one-dimensional cdse nanomaterials: Synthesis and application in photodetectors," *Nanomaterials*, vol. 9, no. 10, p. 1359, Sep. 2019.

[28] N. Z. A. Naharuddin, M. A. Bakar, A. R. Sadrolhosseini, N. Tamchek, M. T. Alresheedi, A. F. Abas, and M. A. Mahdi, "Pulsed-laser-ablated gold-nanoparticles saturable absorber for mode-locked erbium-doped fiber lasers," *Optics & Laser Technology*, vol. 150, p. 107875. Jun. 2022.

[29] Y. Xin, G. Pandraud, Y. Zhang, and P. French, "Single-mode tapered vertical SU-8waveguide fabricated by E-beam lithography for analyte sensing," *Sensors (Switzerland)*, vol. 19, no. 15, p. 3383, Aug. 2019.

[30] S. W. Harun, K. S. Lim, C. K. Tio, K. Dimyati, and H. Ahmad, "Theoretical analysis and fabrication of tapered fiber," *Optik (Stuttg)*, vol. 124, no. 6, pp. 538-43, Mar. 2013.

[31] X. Zhao, Y. Zhang, W. Zhang, Z. Li, L. Kong, L. Yu, J. Ge, and T. Yan," Ultra-high sensitivity and temperature-compensated Fabry–Perot strain sensor based on tapered FBG," *Optics & Laser Technology,* vol. 124, p. 105997, Apr. 2020.

[32] Y. Yu, Q. Bian, J. Wang, X. Zhang, J. Yang, and L. Liang, "All-optical modulation characteristics of a microfiber coupler combined Sagnac loop," *IEEE Photonics Journal*, vol. 11, no. 1, pp. 1-11, Dec. 2018.

[33] C. Chen and J. Wang, "Optical biosensors: An exhaustive and comprehensive review," *Analyst*, vol. 145, no. 5, pp. 1605-1628, 2020.

[34] T. Zhou, Y. nan Zhang, B. Han, A. Zhang, and D. Fu, "Low-cost non-adiabatic tapered fiber for high-sensitive temperature sensing," *Optical Fiber Technology*, vol. 45, pp. 53-57, Nov. 2018.

[35] A. Sulaiman, S. W. Harun, K. S. Lim, F. Ahmad, and H. Ahmad, "Microfiber Mach-Zehnder interferometer embedded in low index polymer," *Optics & Laser Technology*, vol. 44, no. 4, pp. 1186-1189, Jun. 2012.

[36] D. Q. Liu, M. Kang, D. Perry, C. H. Chen, G. West, X. Xia, S. Chaudhuri, Z. P. Laker, N. R. Wilson, G. N. Meloni, and M. M. Melander, "Adiabatic versus non-adiabatic electron transfer at 2D electrode materials," *Nature Communications*, vol. 12, no. 1, p. 7110, Dec. 2021.

[37] M. Arjmand, H. Saghafifar, M. Alijanianzadeh, and M. Soltanolkotabi, "A sensitive tapered-fiber optic biosensor for the label-free detection of organophosphate pesticides," *Sensors and Actuators B: Chemical*, vol. 249, pp. 523-532, Oct. 2017.

[38] A. K. Sharma, J. Gupta, and I. Sharma, "Fiber optic evanescent wave absorption-based sensors: A detailed review of advancements in the last decade (2007–18)," *Optik (Stuttg)*, vol. 183, pp.1008-1025, Apr. 2019.

[39] D. Sun, Y. Ran, and G. Wang, "Label-free detection of cancer biomarkers using an in-line taper fiber-optic interferometer and a fiber Bragg grating," *Sensors (Switzerland)*, vol. 17, no. 11, p. 2559, Nov. 2017.

[40] Y. Mustapha Kamil, M. H. Abu Bakar, M. A. Mustapa, M. H. Yaacob, A. Syahir, and M. A. Mahdi, "Sensitive and specific protein sensing using single-mode tapered fiber immobilized with biorecognition molecules," *IEEE Photonics Journal*, vol. 7, no. 6, pp. 1-9, Oct. 2015.

[41] T. K. Yadav, R. Narayanaswamy, M. H. Abu Bakar, Y. M. Kamil, and M. A. Mahdi, "Single mode tapered fiber-optic interferometer based refractive index sensor and its application to protein sensing," *Optics Express*, vol. 22, no. 19, pp. 22802-22907, Sep. 2014.

[42] S. P. Chakyar, S. K. Simon, C. Bindu, J. Andrews, and V. P. Joseph, "Complex permittivity measurement using metamaterial split ring resonators," *Journal of Applied Physics*, vol. 121, no. 5, Feb. 2017.

[43] H. Kushwah, J. K. Anand, and A. Sethi, "Design methodology of a surface plasmon resonance-based affinity biosensor using instantaneous Poynting vector analysis," *Materials Today: Proceedings*, vol. 71, pp. 160-164, Jan. 2022.

[44] A. Sharma, R. K. Mishra, K.Y. Goud, M. A. Mohamed, S. Kummari, S. Tiwari, Z. Li, R. Narayan, L. A. Stanciu, and J. L. Marty, "Optical biosensors for diagnostics of infectious viral disease: A recent update," *Diagnostics*, vol. 11, no. 11, p. 2083, Nov. 2021.

[45] A. Gharatape and A. Y. Khosroushahi, "Optical Biomarker-based Biosensors for Cancer/Infectious Disease Medical Diagnoses," *Applied Immunohistochemistry and Molecular Morphology*, vol. 27, no. 4, pp. 278-286, Apr. 2019.

[46] M. Mansor, M. A. Bakar, M. F. Omar, Y. M. Kamil, N. Z. Abiding, F. H. Mustafa, and M. A. Mahdi, "Taper biosensor in fiber ring laser cavity for protein detection," *Optics and Laser Technology*, vol. 125, p. 106033, May. 2020.

[47] J. Han, S.-L. Lee, J. Kim, G. Seo, and Y. W. Lee, "Label-Free SARS-CoV-2 Spike Protein Detection Using ACE2-Conjugated Tapered No-Core Fiber," *SSRN Electronic Journal*, Feb. 2022.

[48] D. Farnesi, F. Chiavaioli, F. Baldini, G. C. Righini, S. Soria, C. Trono, and G. N. Conti, "Quasi-distributed and wavelength selective addressing of optical micro-resonators based on long period fiber gratings," *Optics Express*, vol. 23, no. 16, pp. 21175-21180, Aug. 2015.

[49] T. Liyanage, M. Lai, and G. Slaughter, "Label-free tapered optical fiber plasmonic biosensor," *Analytica Chimica Acta*, vol. 1169, p. 338629, Jul. 2021.

[50] A. N. Masterson, T. Liyanage, C. Berman, H. Kaimakliotis, M. Johnson, and R. Sardar, "A novel liquid biopsy-based approach for highly specific cancer diagnostics: Mitigating false responses in assaying patient plasma-derived circulating microRNAs through combined SERS and plasmon-enhanced fluorescence analyses," *Analyst*, vol. 145, no. 12, pp. 4173-4180, May. 2020.

[51] V. Semwal and B. D. Gupta, "LSPR- and SPR-Based Fiber-Optic Cholesterol Sensor Using Immobilization of Cholesterol Oxidase over Silver Nanoparticles Coated Graphene Oxide Nanosheets," *IEEE Sensors Journal*, vol. 18, no. 3, pp.1039-1046, Dec. 2017.

[52] S. Kumar, B. K. Kaushik, R. Singh, N.K. Chen, Q. S. Yang, X. Zhang, W. Wang, and B. Zhang, "LSPR-based cholesterol biosensor using a tapered optical fiber structure," *Biomedical Optics Express*, vol. 10, no. 5, pp. 2150-2160, 2019.

[53] S. Kaushik, A. Pandey, U. K. Tiwari, and R. K. Sinha, "A label-free fiber optic biosensor for Salmonella Typhimurium detection," *Optical Fiber Technology*, vol. 46, pp. 95-103, Dec. 2018.

[54] Y. M. Kamil, M. A, Bakar, M. A. Mustapa, M. H. Yaacob, N. H. Abidin, A. Syahir, H. J. Lee, and M. A. Mahdi, "Label-free Dengue E protein detection using a functionalized tapered optical fiber sensor," *Sensors and Actuators B: Chemical*, vol. 257, pp. 820-828, Mar. 2018.

[55] M. Z. Muhammad, A. A. Jasim, H. Ahmad, H. Arof, and S. W. Harun, "Non-adiabatic silica microfiber for strain and temperature sensors," *Sensors and Actuators A: Physical*, vol. 192, pp. 130-132, Apr. 2013.

[56] A. Banerjee, "Enhancement in sensitivity of blood glucose sensor by using 1D defect ternary photonic band gap structures," *Journal of Optics (India)*, vol. 48, no. 2, pp. 262-265, Jun. 2019.

[57] G. Qiu, Z. Gai, Y. Tao, J. Schmitt, G. A. Kullak-Ublick, and J. Wang, "Dual-Functional Plasmonic Photothermal Biosensors for Highly Accurate Severe Acute Respiratory Syndrome Coronavirus 2 Detection," *ACS Nano*, vol. 14, no. 5, pp. 5268-2577, Apr. 2020.

[58] A. Smolyaninov, A. El Amili, F. Vallini, S. Pappert, and Y. Fainman, "Programmable plasmonic phase modulation of free-space wavefronts at gigahertz rates," *Nature Photonics*, vol. 13, no. 6, pp. 431-435, 2019.

[59] M. Kim, J. H. Lee, and J. M. Nam, "Plasmonic Photothermal Nanoparticles for Biomedical Applications," *Advanced Science*, vol. 6, no. 17. P. 190471, Sep. 2019.

[60] Y. Zhao, Z. Jia, M. Dai, C. Zhao, M. S. Gandhi, S. Sun, Q. Li, and H. Y. Fu, "Cascaded fiber non-adiabatic taper and Sagnac loop for refractive index sensing," *Sensors Actuators A Phys*, vol. 332, p. 113212, Dec. 2021.

[61] L. Xie, B. Sun, M. Chen, and Z. Zhang, "Sensitivity enhanced temperature sensor with serial tapered two-mode fibers based on the Vernier effect," *Optics Express*, vol. 28, no. 22, pp. 32447-32466, Oct. 2020.

[62] J. Li, M. Zhang, M. Wan, C. Lin, S. Huang, C. Liu, Q. He, X. Qiu, and X. Fang, "Ultrasensitive refractive index sensor based on enhanced Vernier effect through cascaded fiber core-offset pairs," *Optics Express*, vol. 28, no. 3, pp. 4145-4155, Feb. 2020.

[63] T. Martan, D. Mares, and V. Prajzler, "Local detection of gaseous carbon dioxide using optical fibers and fiber tapers of single-cell dimensions," *Sensors and Actuators B Chem*, vol. 375, p. 132887, Jan. 2023.

[64] K. Katsarou, E. Bardani, P. Kallemi, and K. Kalantidis, "Viral Detection: Past, Present, and Future," *BioEssays*, vol. 41, no. 10, p. 1900049, Oct. 2019.

[65] J. Costa, E. C. Ferreira, and C. Santos, "Covid-19, chikungunya, dengue and zika diseases: an analytical platform based on MALDI-TOF MS, ir spectroscopy and RT-qPCR for accurate diagnosis and accelerate epidemics control," *Microorganisms*, vol. 9, no 4, p. 708, Mar. 2021.

[66] S. Khan, S. M. Akbar, T. Yahiro, M. A. Mahtab, K. Kimitsuki, T. Hashimoto, and A. Nishizono, "Dengue Infections during COVID-19 Period: Reflection of Reality or Elusive Data Due to Effect of Pandemic," *International Journal of Environmental Research and Public Health*, vol. 19, no. 17, p. 10768, Aug. 2022.

[67] B. H. Kok, H. T. Lim, C. P. Lim, N. S. Lai, C. Y. Leow, and C. H. Leow, "Dengue virus infection – a review of pathogenesis, vaccines, diagnosis and therapy," *Virus Research*, vol. 324, p. 199018, Jan. 2023.

[68] S. Anantapreecha, S. Chanama, A. A-nuegoonpipat, S. Naemkhunthot. A. Sa-Ngasang, P. Sawanpanyalert and L. Kurane, "Serological and virological features of dengue fever and dengue haemorrhagic fever in Thailand from 1999 to 2002," *Epidemiology & Infection*, vol. 133, no. 3, pp. 503-507, Jun. 2005.

[69] H. Fahimi, M. Mohammadipour, H. Haddad Kashani, F. Parvini, and M. Sadeghizadeh, "Dengue viruses and promising envelope protein domain III-based vaccines," *Applied Microbiology and Biotechnology*, vol. 102, no. 7, pp. 2977-2996, Apr. 2018.

[70] W. H. Wang, A. N. Urbina, C. Y. Lin, Z. S. Yang, W. Assavalapsakul, A. Thitithanyanont, P. L. Lu, Y. H. Chen, and S. F. Wang, "Targets and strategies for vaccine development against dengue viruses," *Biomedicine and Pharmacotherapy*, vol. 144, p. 112304, Dec. 2021.

[71] W. Yan, Y. Zheng, X. Zeng, B. He, and W. Cheng, "Structural biology of SARS-CoV-2: open the door for novel therapies," *Signal Transduction and Targeted Therapy*, vol. 7, no. 1, p. 26, Jan. 2022.

[72] M. Platten, D. Hoffmann, R. Grosser, F. Wisplinghoff, H. Wisplinghoff, G. Wiesmüller, O. Schildgen, and V. Schildgen, "SARS-CoV-2, CT-values, and infectivity—conclusions to be drawn from side observations," *Viruses*, vol. 13, no. 8, p. 1459, Jul. 2021.

[73] M. H. Shahrajabian, W. Sun, and Q. Cheng, "Product of natural evolution (SARS, MERS, and SARS-CoV-2); deadly diseases, from SARS to SARS-CoV-2," *Human Vaccines and Immunotherapeutics*, vol. 17, no. 1, pp. 62-83, Jan. 2021.

[74] O. Dadras, A. M. Afsahi, Z. Pashaei, H. Mojdeganlou, A. Karimi, P. Habibi, A. Berzegary, A. Fakhfouri, P. Mirzapour, N. Janfaza, and S. Dehghani, "The relationship between COVID-19 viral load and disease severity: A systematic review," *Immunity, Inflammation and Disease*, vol. 10, no. 3, p. e580, Mar. 2022.

[75] W. Bin Ji, Y. C. Tan, B. Lin, S. C. Tjin, and K. K. Chow, "Nonadiabatically tapered microfiber sensor with ultrashort waist," *IEEE Photonics Technology Letters*, vol. 26, no. 22, pp. 2303-2306, Sep. 2014.

[76] B. Musa, Y. M. Kamil, M. H. Abu Bakar, A. S. Mohd Noor, A. Ismail, and M. A. Mahdi, "Investigating the effect of taper length on sensitivity of the tapered-fiber based temperature sensor," *J Teknol*, vol. 78, no. 3, pp. 135-140, Feb. 2016.

[77] R. M. A. Ayaz, A. Balazadeh Koucheh, and K. Sendur, "Sensitivity of a tapered fiber refractive index sensor at diameters comparable to wavelength," *Optik*, vol. 265, p. 169417, Sep. 2022.

[78] Z. H. Shao, X. G. Qiao, F. Y. Chen, and Q. Z. Rong, "Ultrasonic sensitivity-improved fiber-optic Fabry-Perot interferometer using a beam collimator and its application for ultrasonic imaging of seismic physical models," *Chinese Physics B*, vol. 27, no. 9, p. 094218, Sep. 2018.

[79] L. Chaiet and F. J. Wolf, "The properties of streptavidin, a biotin-binding protein produced by Streptomycetes," *Archives of biochemistry and biophysics*, vol. 106, pp. 1-5, Jan. 1964,

[80] G. E. Walraten and R. T. W. Douglas, "Raman spectra from very concentrated aqueous NaOH and from wet and dry, solid, and anhydrous molten, LiOH, NaOH, and KOH," *Journal of Chemical Physics*, vol. 124, no. 11, Mar. 2006.

[81] Y. Sun, M. Yanagisawa, M. Kunimoto, M. Nakamura, and T. Homma, "Estimated phase transition and melting temperature of APTES self-assembled monolayer using surface-enhanced anti-stokes and stokes Raman scattering," *Applied Surface Science*, vol. 363, pp. 572-577, Feb. 2016.

[82] Y. Liu, Y. Li, X. M. Li, and T. He, "Kinetics of (3-aminopropyl) triethoxylsilane (aptes) silanization of superparamagnetic iron oxide nanoparticles," *Langmuir*, vol. 29, no. 49, pp. 15275-15282. Dec. 2013.

[83] K. Marycz, K. Kornicka-Garbowska, A. Patej, P. Sobierajska, A. Kotela, E. Turlej, M. Kepska, A. Bienko, and R. J. Wiglusz, "Aminopropyltriethoxysilane (APTES)-Modified Nanohydroxyapatite (nHAp) Incorporated with Iron Oxide (IO) Nanoparticles Promotes Early Osteogenesis, Reduces Inflammation and Inhibits Osteoclast Activity," *Materials*, vol. 15, no. 6, p. 2095, Mar. 2022.

[84] M. P. Byrne and W. E. Stites, "Chemically crosslinked protein dimers: Stability and denaturation effects," *Protein Science*, vol. 4, no. 12, pp. 2545-2558, Dec. 1995.

[85] M. Prabhaharan, A. R. Prabakaran, S. Gunasekaran, and S. Srinivasan, "Molecular structure and vibrational spectroscopic investigation of melamine using DFT theory calculations," *Spectrochimica Acta Part A: Molecular and Biomolecular Spectroscopy*, vol. 123, pp. 392-401, Apr. 2014.

[86] K. Ramaiah, J. Prashanth, J. Haribabu, K. E. Srikanth, B. V. Reddy, R. Karvembu, and K. L. Reddy, "Vibrational spectroscopic (FT-IR, FT-Raman), anti-inflammatory, docking and molecular characteristic studies of Ni (II) complex of 2-aminonicotinaldehyde using theoretical and experimental methods," *Journal of Molecular Structure*, vol. 1175, pp. 769-781, Jan. 2019.

[87] S. W. de Taeye, T. Rispens, and G. Vidarsson, "The ligands for human igG and their effector functions," *Antibodies*, vol. 8, no. 2, p. 30, Apr. 2019.

[88] L. L. Lu, T. J. Suscovich, S. M. Fortune, and G. Alter, "Beyond binding: Antibody effector functions in infectious diseases," *Nature Reviews Immunology*, vol. 18, no. 1, pp. 46-61, Jan. 2018.

[89] C. Rader, "Overview on concepts and applications of fab antibody fragments," *Current Protocols in Protein Science*, vol. 55, no. 1, pp. 6-9, Feb. 2009.

[90] M. S. Soares, M. Vidal, N. F. Santos, F. M. Costa, C. Marques, S. O. Pereira, and C. Leitão, "Immunosensing based on optical fiber technology: Recent advances," *Biosensors*, vol. 11, no. 9, p. 305, Aug. 2021.

[91] R. P. Kengne-Momo, P. Daniel, F. Lagarde, Y. L. Jeyachandran, J. F. Pilard, M. J. Durand-Thouand, and G. Thouand, "Protein Interactions Investigated by the Raman Spectroscopy for Biosensor Applications," *International Journal of Spectroscopy*, vol. 2012, 2012.

[92] S. J. Bauman, Z. T. Brawley, A. A. Darweesh, and J. B. Herzog, "Substrate oxide layer thickness optimization for a dual-width plasmonic grating for surface-enhanced raman spectroscopy (SERS) biosensor applications," *Sensors (Switzerland)*, vol. 17, no. 7, p. 1530, Jun. 2017.

[93] Z. Movasaghi, S. Rehman, and I. U. Rehman, "Raman spectroscopy of biological tissues," *Applied Spectroscopy Reviews*, vol. 42, no. 5, ppp. 493-541, Sep. 2007.

[94] A. Jain and K. Cheng, "The principles and applications of avidin-based nanoparticles in drug delivery and diagnosis," *Journal of Controlled Release*, vol. 245, pp.27-40, Jan. 2017.

[95] T. Mahmood, H. Nawaz, A. Ditta, M. I. Majeed, M. A. Hanif, N. Rashid, H. N. Bhatti, H. F, Nargis, M. Saleem, F. Bonnier, and H. J. Byrne, "Raman spectral analysis for rapid screening of dengue infection," *Spectrochimica Acta Part A: Molecular and Biomolecular Spectroscopy,* vol. 200, pp. 136-142, Jul. 2018.

[96] M. J. Oliveira, M. P. de Almeida, D. Nunes, E. Fortunato, R. Martins, E. Pereira, H. J. Byrne, H. Águas, and R. Franco, "Design and simple assembly of gold nanostar bioconjugates for surface-enhanced Raman spectroscopy immunoassays," *Nanomaterials*, vol. 9, no. 11, p. 1561, Nov. 2019.

[97] M. M. Pollack, "Severity of Illness Confusion," *Pediatric Critical Care Medicine*, vol. 17, no. 6, p. 583, Jun. 2016.

[98] G. N. Malavige, C. Jeewandara, and G. S. Ogg, "Dengue and COVID-19: two sides of the same coin," *Journal of Biomedical Science*, vol. 29, no. 1, p. 48, Jul. 2022.

[99] N. Bicudo, E. Bicudo, J. D. Costa, J. A. L. P. Castro, and G. B. Barra, "Co-infection of SARS-CoV-2 and dengue virus: a clinical challenge," *Brazilian Journal of Infectious Diseases*, vol. 24, no. 5, pp. 452-454, Nov. 2020.

[100] Y. Liu, Z. Qin, J. Zhou, X. Jia, H. Li, X. Wang, Y. Chen, Z. Sun, X. He, H. Li, and G. Wang, "Nano-biosensor for SARS-CoV-2/COVID-19 detection: methods, mechanism and interface design," *RSC Advances*, vol. 13, no. 26, pp. 17883-17906, 2023.

[101] M. B. Abdullah, C. Dab, M. Almalki, A. Alnaim, A. Abuzir, and C. Awada, "Ultrafast Detection of SARS-CoV-2 Spike Protein (S) and Receptor-Binding Domain (RBD) in Saliva Using Surface-Enhanced Raman Spectroscopy," *Applied Sciences (Switzerland)*, vol. 12, no. 10, p. 5039, May. 2022.

[102] J. E. Sanchez, S. A. Jaramillo, E. Settles, J. J. Salazar, A. Lehr, J. Gonzalez, C. R. Aranda, H. R. Navarro-Contreras, M. O. Raniere, M. Harvey, and D. M. Wagner, "Detection of SARS-CoV-2 and its S and N proteins using surface enhanced Raman spectroscopy," *RSC Advances*, vol. 11, no. 41, pp. 25788-25794, 2021.

[103] A. Leung, P. M. Shankar, and R. Mutharasan, "Model protein detection using antibody-immobilized tapered fiber optic biosensors (TFOBS) in a flow cell at 1310 nm and 1550 nm," *Sensors and Actuators B: Chemical*, vol. 129, no. 2, pp. 716-725, Feb. 2008.

[104] H. Y. Lin, C. H. Huang, G. L. Cheng, N. K. Chen, and H. C. Chui, "Tapered optical fiber sensor based on localized surface plasmon resonance," *Optics Express*, vol. 20, no. 19, pp. 21693-21701, Sep. 2012.

[105] N. Cennamo, L. Pasquardini, F. Arcadio, L. Lunelli, L. Vanzetti, V. Carafa, L. Altucci, and L. Zeni, "SARS-CoV-2 spike protein detection through a plasmonic D-shaped plastic optical fiber aptasensor," *Talanta*, vol. 233, p. 122532, Oct. 2021.

[106] D. Yang, A. Singh, H. Wu, and R. Kroe-Barrett, "Comparison of biosensor platforms in the evaluation of high affinity antibody-antigen binding kinetics," *Analytical Biochemistry*, vol. 508, pp. 78-96, Sep. 2016.

LIST OF PUBLICATIONS

N. N. Zulkeflee, Y. M. Kamil, M. H. A. Bakar, and S. Mashohor, "Cascaded Dual-Tapered Optical Microfiber Sensors for Simultaneous Detection of Refractive Indices in Multiple Solutions," *Fiber and Integrated Optics*, vol. 34, no. 5, pp.1-19, 2024.

N. N. Zulkeflee, M. H. A. Bakar, Y. M. Kamil, and S. Mashohor, "Functionalized cascaded tapered optical fiber sensor for simultaneous detection of Dengue E and SARS-CoV-2 Spike proteins"– *submitted to Biosensors and Bioelectronics*